Monitoring and Control of Semiconductor Manufacturing Using Acoustic Techniques

A Thesis
Presented to
The Academic Faculty

By

Frances R. Williams

In Partial Fulfillment
of the Requirements for the Degree
Doctor of Philosophy in the
School of Electrical and Computer Engineering

Georgia Institute of Technology
November 2003

Monitoring and Control of Semiconductor Manufacturing Using Acoustic Techniques

Approved by:

Dr. Gary S. May, Advisor

Dr. Mark G. Allen

Dr. Farrokh Ayazi

Dr. Peter J. Hesketh

Dr. William D. Hunt

Date Approved November 25, 2003

This thesis is dedicated to my parents for the many sacrifices they made throughout the years to ensure this day would come to pass.

ACKNOWLEDGEMENTS

To God be the glory for the things He has done. I would like to thank you God for the gift of Life through Your Son Jesus and for the daily guidance and strength to strive and endure. Thank you for this journey You have brought me through while in Atlanta. It has not only developed me and revealed to me who I am, but it has shown me just how awesome and great You are. I am humbled to be Your child. I will praise You all my days!

To my parents, I love you very much and thank you for all of the encouragement, support, and many (MANY) prayers. You knew I could when I didn't. To my siblings, thank you all for being such wonderful and supportive siblings. You all are the wind beneath my wings.

I give special thanks to my advisor, Dr. Gary S. May, for his support and guidance throughout my studies at Georgia Tech. He supported and believed in my efforts even when I was frustrated with my research and has served as a source of inspiration, encouragement, and professional guidance. Thus, I am a better researcher, teacher, mentor, and person. I would also like to thank Dr. Mark Allen and Dr. William Hunt for serving on my reading committee. A sincere thanks is also extended to the other members of my defense committee, Dr. Farrokh Ayazi and Dr. Peter Hesketh.

I am also grateful to Yong Kyu Yoon, Shawn Pinkett, Seong-O Choi, Jin-Woo Park, Gregory Triplett, Terence Brown, and Pam Jackson who contributed to my research endeavors. I would also like to thank Mrs. Laureen Rose, Mr. Gary Spinner, and the other MiRC staff whose assistance helped facilitate the processing of my device. Special

thanks to the Intelligent Semiconductor Manufacturing research group for their support and friendship. I would also like to thank Ameisha Sampson for her editing assistance.

I would be remiss if I did not mention all of the wonderful friends and associates I have met while at Georgia Tech. Your friendship, prayers, support, and encouragement have carried me through my time at Tech. I would especially like to thank Vanessa Hall, Charima Young, Lavinna King, Avalon Blenman, and Kendra Taylor. Special thanks to the MiRC crew: Cleon Davis, Gregory Triplett, Terence Brown, and Demetris Geddis. I cannot forget all of my friends who have been there for me since my days at A&T (and some since high school): Tameka Paschal, Nikki Darden, Tanja Darden, Fonda Daughtery, and Kim Rains. I would also like to thank my New Birth Cathedral church family and the 7th Day Dance Ministry—I'm going to really miss you all!

Table of Contents

Dedication iii

Acknowledgements iv

List of Tables ix

List of Figures x

Summary xiii

Chapter 1. Introduction 1

1.1. Process Monitoring in Semiconductor Manufacturing 3

1.2. Motivation for Thesis Work 5

1.2.1. Acoustic Sensing 5

1.2.2. Electrochemical Deposition 6

1.2.3. Research Objectives 8

1.3. Thesis Organization 9

Chapter 2. Review of Existing *In-Situ* Process Monitoring Techniques 10

2.1. Optical-Based Sensors 10

2.1.1. Optical Emission Spectroscopy 11

2.1.2. Interferometry 13

2.1.3. Spectroscopic Ellipsometry 15

2.1.4. Optical Pyrometry 17

2.2. Acoustic Sensors 19

2.2.1. Acoustic Wave Devices 19

2.2.1.1.Types 22

2.2.1.2.Parameter Sensitivity 25

2.2.2. Silicon Microphones 26

2.2.2.1.Types 27

2.2.2.2.Parameter Sensitivity 33

2.2.3. Acoustic Sensors in Semiconductor Process Manufacturing 33

2.3. Summary 35

Chapter 3. A Piezoelectric Sensor for Process Monitoring 37

3.1. Sensor Theory and Operation 37

3.2. Piezoelectric Materials 43

3.3. Circuit Model 46

3.4. Summary 50

Chapter 4. Fabrication Process 51

4.1. Sensor Design 51

4.2. Micromachining 55

4.3. Emulsion Plating 57

4.4. Process Sequence 59

Chapter 5. Sensor Response and Measurement 64

5.1. Theory of Thin Plates 64

5.2. Theoretical Sensitivity Calculations 67

5.3. Experimental Results 73

5.3.1. Test Set-up 73

5.3.2. Results 75

5.4. Comparison 75

5.5. Summary 77

Chapter 6. Monitoring Electrochemical Deposition Using the Acoustic Sensor 79

6.1. Electroplating Mechanism 81

6.2. Nickel-Iron Plating 88

6.3. The Propagation of Sound in Fluids 89

6.4. Plating Set-Up 91

6.5. Predictive Model for Metallization 96

Chapter 7. Conclusion 105

7.1. Summary of Contributions 106

7.2. Future Work 109

Appendix A Time Delay Experiments 112

Appendix B Statistical Model Results 121

References 122

Vita 129

List of Tables

Table 1	Parameters to be measured	3
Table 2	Piezoelectric constitutive equations and definitions of piezoelectric parameters	44
Table 3	Composition of Ni-Fe electroplating solution	88
Table 4	Time delay measurements	114
Table 5	Salt molarity and time delay data	115
Table 6	ANOVA table for response thickness *T*	121
Table 7	Least squares coefficients for regression model	121

List of Figures

Figure 1	OES system set-up	12
Figure 2	Characteristic plasma emissions	12
Figure 3	Physical principle of interferometry	14
Figure 4	Basic geometry of Ellipsometry measurements	16
Figure 5	IDT design	21
Figure 6	Acoustic wave device structure	23
Figure 7	Capacitive microphone	28
Figure 8	Piezoresistive microphone	30
Figure 9	Position of piezoresistors on microphone membrane	30
Figure 10	Piezoelectric microphone	31
Figure 11	Optical-waveguide microphone	32
Figure 12	Simple piezoelectric structure	38
Figure 13	Piezoelectric effect in quartz	39
Figure 14	Sensor equivalent circuits	47
Figure 15	Sensor circuit employing a charge amplifier	48
Figure 16	Cross-sectional view of piezoelectric acoustic sensor	53
Figure 17	ANSYS plot of stress in x-direction	53
Figure 18	Electrode pattern	54
Figure 19	Piezoelectric response	55
Figure 20	Pyroelectric response	55
Figure 21	Mask layout	58

Figure 22 Camera set-up for making masks 59

Figure 23 Schematic of fabrication process 60

Figure 24 Etching set-up with PDMS ring 63

Figure 25 Sensor diaphragm 66

Figure 26 Side view of deflected diaphragm 66

Figure 27 Testing set-up 74

Figure 28 Plot of sensor sensitivity (amplified) 75

Figure 29 Water dipole 81

Figure 30 Alignment of ions with water molecule 82

Figure 31 Environment of ion in aqueous solution 83

Figure 32 Electrolytic cell 85

Figure 33 Ion transfer for metal deposition 87

Figure 34 Electroplating monitoring set-up 92

Figure 35 Sensor output voltage vs. Ni-Fe thickness 96

Figure 36 Experimental data and output from regression model for plating thickness vs. voltage 99

Figure 37 Experimental data and output from regression model for plating thickness vs. time 99

Figure 38 Feed-forward network showing input, hidden, and output layers 100

Figure 39 ObOrNNS display with input, output, target, and error data 102

Figure 40 Response surface graph generated from ObOrNNS 104

Figure 41 Sensor/loudspeaker measurements 113

Figure 42 Time delay vs. molarity 116

Figure 43 Electroplating set-up for measuring time delay 118

Figure 44 Time delay vs. nickel mass 119

SUMMARY

Since semiconductor fabrication processes require numerous steps, cost and yield are critical concerns. *In-situ* monitoring is therefore vital for process control. However, this goal is currently restricted by the shortage of available sensors capable of performing in this manner. The goal of this research therefore, was to investigate the use of acoustic signals for monitoring and control of semiconductor fabrication equipment and processes. Currently, most methods for process monitoring (such as optical emission or interferometric techniques) rely on "looking" at a process to monitor its status. What was investigated here involved "listening" to the process. Using acoustic methods for process monitoring enhances the amount and sensitivity of data collection to facilitate process diagnostics and control.

A silicon acoustic sensor was designed, fabricated, and implemented as a process monitor. Silicon acoustic sensors are favorable because of their utilization of integrated circuit and micromachining processing techniques; thus, enabling miniature devices with precise dimensions, batch fabrication of sensors, good reproducibility, and low costs. The fabricated sensor was used for *in-situ* monitoring of nickel-iron electrochemical deposition processes. During this process, changes occur in its plating bath as the alloy is being deposited. It is known that changes in the process medium affect the acoustic response. Thus, the sensor was implemented in an electroplating set-up and its response was observed during depositions. By mapping the sensor response received to the film thickness measured at certain times, a predictive model of the plated alloy thickness was

derived as a function of sensor output and plating time. Such a model can lead to real-time monitoring of nickel-iron thickness.

CHAPTER 1

INTRODUCTION

As feature sizes continue to decrease, the level of integration of semiconductor devices continues to increase in complexity and number of components. The demand in integrated circuit (IC) manufacturing is to accommodate this trend without increased manufacturing cost. Microprocessors, for example, had a density of 38.6 million logic transistors per cm^2 at the cost of 107 microcents in 2001, but the expectations for 2005 include a density of 97.2 million logic transistors per cm^2 at a cost of 27 microcents per transistor [1].

IC packaging must also evolve to accommodate the changing trends in IC technology. IC packaging provides interconnections, power, cooling, and protection of the IC [2]. It dictates the system's cost, size, electrical performance and reliability and is the bottleneck to system performance. Therefore, packaging requirements such as costs, power, input/output (I/O) count, and operating frequency must be consistent with IC roadmap projections. For example, compared to requirements for 2002 where high performance packages had costs of 2.66 cents/pin, a maximum power of 129 watts, 2248 I/O connections, and operated at 800 MHz, 2005 expectations include costs of 2.28 cents/pin, power of 160 watts, 3158 I/O connections, and an operating frequency of 1000 MHz [1,2].

Semiconductor wafer manufacturing challenges will increase as feature size is expected to approach 0.05 microns in coming years [3]. Improvements in fabrication methods and processes are critical for producing these small dimensions cheaply and

reliably. Semiconductor fabrication requires hundreds of successive processing steps, including cleaning routines, oxidation, diffusion, photolithography, etching, and deposition steps [3]. Each of these can potentially contribute to yield loss and increased cost. Therefore, IC technology development requires not only advancement of device fabrication processes, but also advances in process monitoring and control [4]. Stringent process control methods are needed to ensure manufacturability. Process monitoring and control are used to obtain minimal process parameter deviations and high device yield, which requires monitoring process variables from pre- and post-process measurements as well as real time measurements [4]. The aim of process control is to enable the process to remain "centered" within some desired tolerance range [5].

Traditionally, process monitoring primarily has relied on statistical process control (SPC) techniques. SPC is usually performed off-line and is obtained from measurements taken after several batches of wafers are processed. SPC uses *ex-situ* measurements to provide important statistical data based on the status of the equipment and wafer batches [6]. It can determine out-of-tolerance conditions and then initiate corrective measures. Modifications are usually made on process input parameters based on the relation between the input parameters and the critical wafer parameters measured [7]. Unfortunately, the delay inherent in SPC methods may lead to several incorrectly processed batches, which can be quite costly. SPC requires using monitor wafers that can add to costs as well [7]. In addition, off-line measurements are labor intensive and time consuming [6].

In-situ sensors, however, can be used to measure and monitor certain critical process parameters in real time instead of after a run has been completed. Process shifts,

therefore, can be determined immediately and defective components can be detected earlier. *In-situ* sensors for process monitoring of semiconductor manufacturing equipment and processes may enable higher equipment up-time, reduce process parameter variations, reduce equipment-related drift, and reduce total device manufacturing cycle time [4]. During a run, *in-situ* sensors can be used to collect process data that can be used to develop a predictive model for the process as well.

1.1. Process Monitoring in Semiconductor Manufacturing

Sensors generally convert an input signal of some specific form into an electrical signal [8]. They usually detect, measure, or record physical phenomena [9]. *In-situ* process sensors can be used for real-time feedback control, detection of process end-point, and for equipment or process diagnosis [6]. Table 1 shows some of the different parameters of interest to process control engineers and researchers. If these parameters can be measured by *in-situ* process sensors, they have the potential of allowing monitoring and control of manufacturing processes [9].

Table 1. Parameters to be measured.

Gas Flow	Chamber Pressure
Wafer Temperature	Microwave Power
Gas Impurity	Critical Dimension
Film Thickness	Metal Film Sheet Resistance

Process control sensors are generally categorized as invasive or non-invasive. Invasive sensors have the potential of altering the process environment as well as the wafer surface, and therefore are not favorable for real-time monitoring. Process monitoring is optimally performed with non-invasive *in-situ* sensors where some sensing phenomenon is exploited to measure the parameter of interest. The sensor and its operating mechanism are established by criteria such as the process being monitored and the critical parameter(s) to be measured. Challenges may arise in implementing these sensors in process chambers, since the process environment may present difficulties such as high processing temperature or a highly reactive environment [4].

In-situ process control sensors are generally grouped into three categories: equipment state, process state, and wafer state sensors [4,5,9]. Equipment state sensors monitor the status of the processing equipment. They may be used to control the equipment or identify machine failure or aging. Some machine state measurements include pumping speed of vacuum systems, chamber contamination, and leak detection. Process state sensors monitor the process environment and parameter settings that will yield the desired wafer properties or qualities. Numerous parameters affect the process, but some that have a significant effect include wafer temperature, process gas pressure and flow, and plasma species, concentration, and energies [5-6]. These sensors provide closed-loop machine control, keeping the process environment constant [5]. Wafer state sensors measure the effect of the manufacturing process on the wafer. Wafer state measurements are extremely important as wafer parameters are directly proportional to device yield and performance [4]. Using process models, measurements from wafer state sensors can lead

to real-time modification of process parameters/variables [5]. Wafer state measurements include film thickness, film thickness uniformity, and sheet resistance.

1.2. Motivation for Thesis Work

There is a shortage of sensors that have been developed as process monitors. Many methods currently available utilize optical-based techniques to monitor various process parameters *in-situ* [3]. These methods rely on "looking" at a process to monitor its status. While they may be the most common *in-situ* process control sensors, they are somewhat limited in their applications and can be expensive. Thus, alternative or complementary techniques, such as acoustic methods, are also desirable for monitoring semiconductor manufacturing equipment and processes *in-situ*. Acoustic methods involve "listening" to the manufacturing process to enhance the amount and sensitivity of data collection to facilitate process diagnostics and control.

1.2.1. Acoustic Sensing

Acoustic devices offer potential as *in-situ* sensors because they are highly sensitive to surface changes and perturbations [10-11]. They are also capable of sensing in both gas and liquid environments [10]. Acoustic sensors can be fabricated using IC fabrication methods, yielding high fabrication accuracy and reproducibility, bulk fabrication, low cost, high performance, and the integration of on-board signal processing electronics [8]. They have been reported as providing measurement of parameters such as pressure, temperature, mass loading, liquid density and viscosity, as well as electrical conductivity [10,12]. Many of these parameters are of interest in semiconductor manufacturing.

1.2.2. Electrochemical Deposition

Electrochemical deposition (electroplating) processes are used in the semiconductor industry to deposit various metals on substrates in aqueous solutions. They do not require expensive or complicated equipment and can be performed in a beaker [13]. Electroplating entails two different methods: electrolytic and electroless plating. In electrolysis, the beaker contains an electroplating solution (electrolyte) consisting of ions of the metal to be plated, as well as negative and positive electrodes. The substrate to be plated is located at the negative electrode (cathode). Power is supplied to the electrodes causing current to flow through the electrolyte. This current is needed to drive a non-spontaneous reaction—the flow of electrons from the anode to the cathode. Therefore, electrons are supplied to the surface of the substrate and metal cations in the solution move towards the cathode, become reduced (gain electrons), and deposit metal there [13-15]. In electroless plating, an exposed metal surface or seed layer is placed in the plating solution. Electroless plating eliminates the need for an external power supply and an anode. This type of deposition uses chemical instead of electrical reduction. The reduction and oxidation processes are carried out on the same metal surface [15, 16].

Electrochemical deposition has existed since the 1800's, and has evolved in its technique and usage. Its discovery has been linked to Luige Brugnatelli, a friend of Allisandro Volta, who discovered the electrical cell a short time prior to Brugnatelli's discovery [17]. Brugnatelli's work involved plating gold over silver objects. By 1840, electroplating was more widely known and had been refined as a plating method that could be used for producing printing press plates. Today's usage of electroplating ranges from the deposition of metals such as silver or gold on jewelry to the plating of chrome

on car parts [17]. Since the mid-1900's, electroplating has been use more extensively for plating electronic components. It is not only used in fabricating electronic devices in the IC industry but for micromachining of high aspect ratio metal parts. Metals that can be electroplated include copper, gold, silver, nickel, tin, palladium, tin-lead alloys, palladium alloys, gold alloys, and magnetic alloys such NiFe, NiFeMo, and CoFeCu [13-19]. Electroplating has been used to deposit these metals on printed circuit boards for contacts and interconnects, as corrosion protective surfaces, on chip packages, as etch masks, for thin film magnetic heads, and in the creation of electrostatic or magnetic actuators [16, 19].

While the IC industry may seek to avoid wet chemical processing when dry deposition alternatives are available, electroplating has various attributes that validates its necessity in this industry. Plating is an attractive deposition technique because it is inexpensive, is an additive process, provides for the deposition of large thicknesses at relatively fast rates, is performed at low temperatures, and can be used to deposit a wide range of metals including metal alloys. Electrodeposition also enables the plating of via holes and blind vias, the fabrication of high-density metal patterns, and the ability to control various properties of the deposited metal by modifying the plating bath [16]. Also, because of the mechanism of electroplating metals—ions leaving the plating solution and depositing metal on the areas of the substrate exposed by a polymer mask atom by atom—even the smallest features of the plating mold can be duplicated on the substrate [16]. Electroplating enables the creation of high-aspect-ratio parts used for microelectromechanical systems (MEMS). Many other metal deposition techniques cannot produce structures with a height-to-width aspect ratio that is greater than 1:1

without challenges [16]. Processing challenges such as the shadowing effect prevent these other methods from realizing the pattern precisely on the substrate. Shadowing can result in metals that have rounded edge profiles [16].

1.2.3. Research Objectives

In the semiconductor industry, manufacturers of integrated devices are concerned with device yield, which denotes the fraction of finished devices that are fully functional and able to be sold. Yield loss can be attributed to wafer defects, processing errors and miscalculations, and assembly damage [20]. Monitoring of manufacturing processes helps alleviate errors and miscalculations during processing, thereby increasing yield and ultimately decreasing manufacturing cost and increasing profit. The objective of this research is to investigate the use of acoustic methods for *in-situ* monitoring of semiconductor manufacturing processes. More specifically, this work focuses on developing an acoustic sensor that will provide a novel technique for monitoring electroplating deposition processes. This research establishes a predictive model of the progression of metallization during electroplating based on signals from the acoustic sensor in an electroplating set-up. During certain electroplating processes, changes in the plating solution composition yield changes in an acoustic signal transmitted through the bath. Thus, the sensor data and measured plated metal thickness can be recorded and mapped to yield an empirical relationship between the two, leading to real-time monitoring of electroplating.

1.3. Thesis Organization

Chapter 2 of this thesis presents a review of existing *in-situ* process monitoring techniques. These methods are based on optical and acoustic sensors. A thorough discussion of the various types of acoustic sensors as well as their applications for monitoring semiconductor manufacturing is included. In Chapter 3, the piezoelectric sensor developed in this research is described. This chapter details the theory and operation of the sensor, the mechanism of piezoelectricity, selection of piezoelectric materials, and the circuit model used to represent the acoustic sensor. The design of the sensor and process sequence used to fabricate it are then outlined in Chapter 4. Chapter 5 derives the theoretical sensitivity of the sensor and presents the experimental response. The theoretical and experimental results are then compared and discussed. Electrochemical deposition is described in Chapter 6. The mechanism and chemistry of electroplating is presented, as well as details about the nickel-iron plating bath used in this research. Chapter 6 also presents the implementation of the piezoelectric acoustic sensor in the electroplating set-up. The predictive model developed for film thickness is then presented. Chapter 7 summarizes the research detailed in this thesis, provides final comments, and describes directions for future research.

CHAPTER 2

REVIEW OF EXISTING *IN-SITU* PROCESS MONITORING TECHNIQUES

Since microelectronics fabrication processes require numerous steps, cost and yield are critical concerns. Thus, manufacturing companies are continuously seeking improvements in fabrication methods and processes. Ideally, one would like to monitor and control crucial semiconductor process parameters (such as those in Table 1) *in-situ*. These parameters are significant for obtaining denser, yet cheaper chips while maintaining high yields, reliability, and performance [4]. Much work is still to be done to realize a full range of sensors to provide such capabilities. Most monitoring schemes still rely on pre- and post-process measurements [3]. Also, wafer state measurements are still lagging behind other process control measurements. This chapter reviews some of the *in-situ* process monitoring techniques currently available. Many of these methods can be classified as either optical or acoustic sensors.

2.1. Optical Sensors

Currently, most *in-situ* process sensors are optical in nature. These include optical emission spectroscopy (OES), interferometry, ellipsometry, and optical pyrometry. These techniques can be used to determine parameters such as etch/deposition rates, film thickness, and wafer temperature based on optical emission variations, the interference of

light waves, and light polarization changes. An overview of these sensors describing their advantages and limitations as process control sensors is given below.

2.1.1. Optical Emission Spectroscopy (OES)

OES is a common process state sensor that is used frequently in plasma processes. It is the most common method for end-point detection during plasma etch. Optical emission from a plasma is produced by the impact of electrons with gaseous species that thereby decay and emit excess energy in the form of photons [21-22]. These photons can be measured through optical techniques. A typical OES set-up for a plasma system is shown in Figure 1. It uses a monochromator to collect the emission spectra [23].

OES is a bulk measure of the optical radiation of the plasma species and is considered a "passive" method (compared to laser interferometry and ellipsometry). During an etching process, emission can come from etch products, etchants, or their residue. Because the spectra emitted by excited chemical species are generally unique, the composition of a gas mixture can be determined [24]. OES generally provides an average intensity at a certain wavelength above the wafer. The spectrum from a plasma changes during an etching process. The wavelengths that appear correspond to the etch reaction product (Figures 2a and 2b). The intensity at a single wavelength can be monitored by setting the optical spectrometer to the line of interest. Thus, by monitoring a by-product species, etch end-point can be detected (Figure 2c) [25].

OES is only beginning to be examined for indirect *in-situ* monitoring of wafer state [21]. It is currently limited because light from plasma has numerous emissions from many species that include a wide spectral range. Often, it is difficult to delineate a

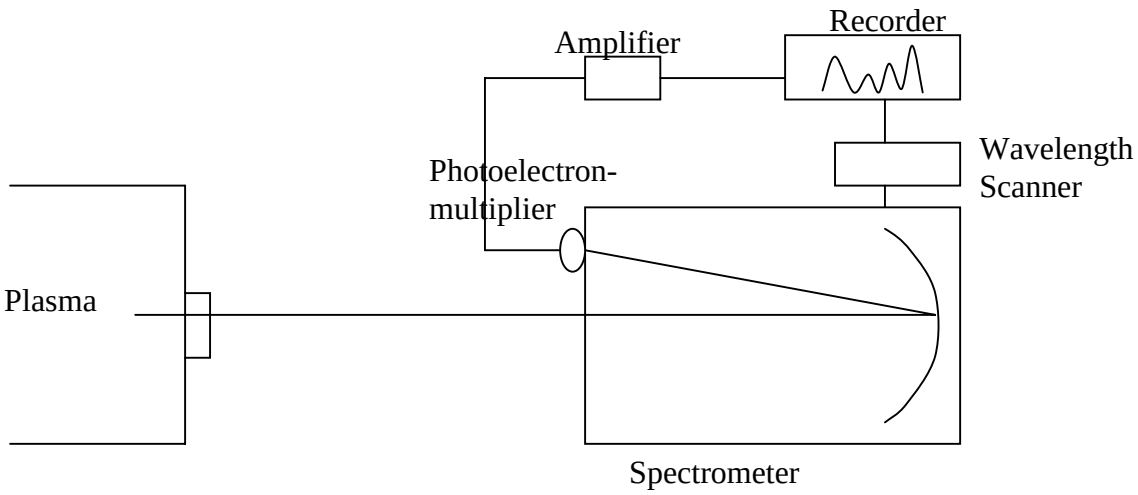

Figure 1. OES system setup [23].

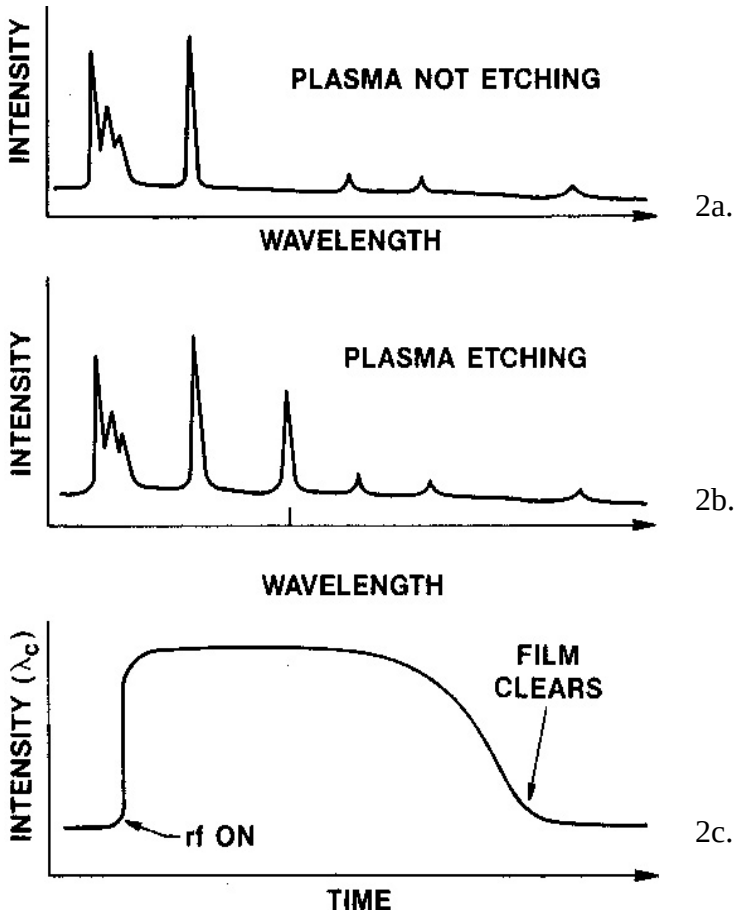

Figure 2. Characteristic plasma emissions [24].

characteristic line from the intense background [24]. However, new approaches are being derived for OES in which multiple beams are used to spatially resolve the intensity across the substrate [21]. This approach may produce process state information and estimates of wafer state parameters. As a wafer state sensor, OES could measure parameters such as spatial uniformity of the etch [21]. This approach can also be applied to plasma deposition processes [9].

2.1.2. Interferometry

Interferometers can be used as wafer state sensors. Their operation is based on the theory of light wave interference [26]. For laser interferometry, as a beam of monochromatic light is reflected by a top surface and the underlying interface of a transparent film, the rays combine and interfere—constructively and destructively (in phase and out of phase) [24, 27]. The interference is characteristic of the film thickness and wavelength of the light. Therefore, laser interferometry can be used to monitor the thickness of transparent films. A He-Ne laser (632.8 nm) light source is usually used because of its affordability, monochromaticity, and coherence of its emitted light [27].

As shown in Figure 3, some of the incident light reflects off of the top surface and some is transmitted through the film layer and reflected off of the film-substrate interface. The reflected intensity is a periodic function of film thickness and the amplitude of the reflected intensity is a function of the index of refraction of the ambient, film, and substrate [25]. The interference of the top and underlying layer causes the reflected intensity to change as the film thickness changes. When the interference is constructive, an optical maximum will occur. When the interference is destructive, an optical

minimum results [28]. Thus, the intensity varies sinusoidally. The film thickness is determined by observing the time between either the minima or maxima on the interferogram and is given by

$$d = \frac{\lambda}{2n} \tag{1}$$

where d is the film thickness, λ is the wavelength of the interferometer laser, and n is the index of refraction of the film [24].

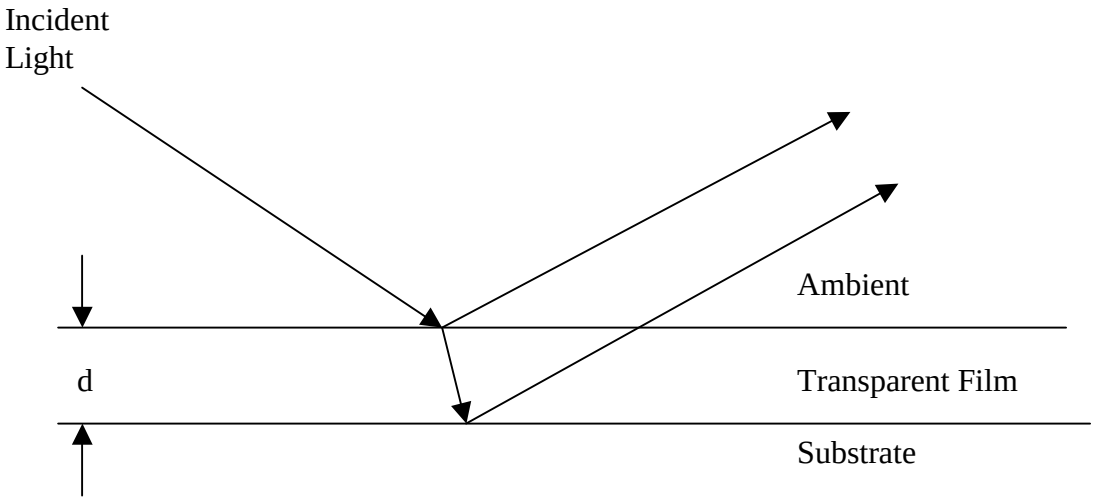

Figure 3. Physical principle of interferometry.

Laser interferometry provides *in-situ* monitoring of deposition and etch rates as well as end-point detection. It can be used to determine thickness as small as a few hundred angstroms [28]. It is limited in that it is only for transparent films and also because it monitors only a small spot on the substrate surface. Non-uniformities, therefore, may be associated with the data received from the sample observed [24].

Interferometry can be extended to full wafer measurements, however, where measurements can be obtained from multiple points across the wafer. For example, in plasma systems, this technique uses the plasma optical emission as the light source. A specific plasma emission line from the wafer surface is reflected onto a CCD camera, where the wafer surface is imaged using an optical band pass filter [9, 26]. Interferograms generated enable the etch or deposition rate distributions to be mapped across the wafer. This sensor is promising, but it may encounter hardware alignment and calibration difficulties. Filtering and then analysis of the extensive amount of data produced may also be a concern. Interferometers are costly as well [25].

While laser interferometry is not suitable for opaque films, such as metals, laser reflectance may be viable for end-point detection of such materials. Metal films have high reflectance intensity. Therefore, when completely etching through a metal to an insulator or semiconductor surface, there will be a sharp change in the intensity of the reflected light. This change can be used to signify end-point [24].

2.1.3. Spectroscopic Ellipsometry

Spectroscopic ellipsometers (SE) are ellipsometers that provide data for multiple wavelengths. Ellipsometry theory is based on the change in polarization of light after being reflected from a surface [26, 29]. The electric field portion of linearly polarized light propagates in one direction and has a *p*-component and an *s*-component, denoted by E_p and E_s, respectively. The *p* subscript stands for parallel (to the plane of incidence) and the *s* subscript stands for the German word ‘senkrecht’ which means perpendicular [30]. As shown in Figure 4, when linearly polarized light is reflected from a surface, its

components experience attenuation and a phase shift, causing the light to become elliptically polarized.

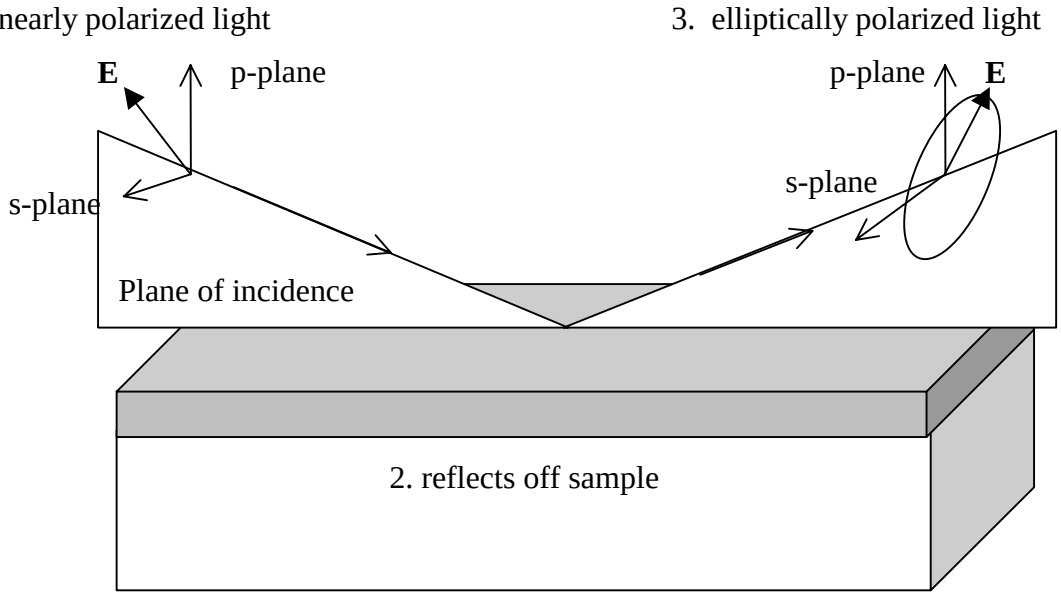

Figure 4. Basic geometry of ellipsometry measurements.

Ellipsometry determines the change in two parameters, the amplitude ψ and phase Δ, between Fresnal reflection coefficients for *p* and *s* polarized light. These coefficients are R_p and R_s, respectively [31]. ψ and Δ are usually defined by a ratio of these coefficients, ρ, which is given by

$$\rho = \frac{R_p}{R_s} = \tan(\Psi)e^{i\Delta} = \rho(\Phi, \lambda, N_i, L_i) \qquad (2)$$

where Φ is the angle of incidence, λ is the wavelength of the ellipsometer, N_i and L_i are the complex index and thickness of the i^{th} component respectively [31]. Also, $\Delta=\delta_p- \delta_s$

where δ_p and δ_s are the phase shifts of the *p*- and *s*- planes, respectively. R_p and R_s are given by

$$R_p = \frac{E_{pr}}{E_{pi}} \tag{3}$$

$$R_s = \frac{E_{sr}}{E_{si}} \tag{4}$$

where E_p and E_s are the *p*- and *s*- components of the electric field, respectively. The *r* and *i* subscripts denote that the waves are reflected (r) or incident (i) waves.

The change in state of polarization can be analyzed as a function of wavelength using Fourier analysis [17, 19]. ψ and Δ are usually measured and are a function of the material's index of refraction, thickness, and composition. Therefore parameters such as film thickness can be measured *in-situ* using SE.

Because ellipsometry is a measure of the ratio of two values, it is a repeatable and accurate measurement technique [32]. Its phase measurements allow it to have sub-monolayer sensitivities [31]. During many process reactions, the process window of the chamber becomes coated with reaction byproducts and result in intensity changes. SE sensors are insensitive to these changes and therefore eliminate the presence of such errors [31]. The sensor system, however, requires precise alignment and calibration for optimum sensitivity. Also, these sensors are restricted to transparent films.

2.1.4. Optical Pyrometry

Optical pyrometers are the most widely used sensors for temperature measurements in rapid thermal processing (RTP) reactors. The word pyrometry comes from the Greek word "pyro" (fire) and the word "metron" (measured). Pyrometers are photodectors that

absorb energy or measure the intensity of an electromagnetic (EM) wave [33]. Pyrometry theory is based on the emission of radiation from objects that is a function of their temperature [4]. A pyrometer monitors the electromagnetic radiation emitted by a wafer and then uses that information, along with the predetermined directional spectral emissivity of the wafer, to compute the wafer temperature. This relationship is derived from the ideal blackbody radiation-temperature relationship of Planck's law, which is given by [4]

$$W_b(\lambda, T) = \frac{2\pi c^2 h}{\lambda^5 \left[e^{(hc/k\lambda T)} - 1 \right]} \tag{5}$$

where W_b is the radiant power intensity from a blackbody, λ is the wavelength, T is the absolute temperature, h is Planck's constant (6.625×10^{-35} J-s), c is the speed of light (3×10^8 m/s), and k is Boltzmann's constant ($1.380 \times^{-23}$ J/K). Therefore, if the radiation intensity (W_b) is measured at a known wavelength (λ), the temperature T can be derived [33]. Equation (5), however, is given for blackbody objects (i.e., objects where all of the EM radiation is absorbed and where the maximum possible radiation is emitted). For any object that deviates from this condition, emissitivity must be considered. The emissitivity describes the difference between the radiation absorption of blackbodies and real objects. It is given as the ratio of radiation emitted by a non-blackbody material to that emitted by a blackbody object at the same temperature [33].

Therefore, the accuracy of optical pyrometers depends on the knowledge of the spectral emissivity, which is used as a correction factor for Planck's Law. This parameter can vary during the process, however, due to the temperature and process properties [31]. Emissivity can be affected by the dimensions and surface of the chamber walls,

interference effects of heated viewports and lamps, the thickness of any layers on the wafer surface (if a deposition process), and other wafer characteristics [4]. This can lead to erroneous temperature measurements that are up to 10^{o}C off [4]. Reproducible measurements are also an issue for optical pyrometry measurements.

2.2. Acoustic Sensors

Acoustic devices are of great interest because they are generally small, cheap, highly sensitive, and have the ability to characterize the effects of a wide range of measurands. Detection and characterization of a parameter are generally based on changes in the physical properties of the medium in contact with the sensor surface. For acoustic sensors, the medium could be a gas, liquid, or a solid. Acoustic devices are known to be sensitive to many of the parameters that could lead to process monitoring of various semiconductor manufacturing processes. Some of these properties/parameters include mass, electrical conductivity, flow, viscosity, pressure, and temperature variations. Acoustic sensors can be fabricated using IC and micromachining technologies; therefore leading to the creation of small, precise, and reproducible sensors that are capable of being integrated with other electronic circuitry. This thesis investigates using acoustic methods to provide alternative or complementary techniques to the optically based process monitoring sensors presented above.

2.2.1. Acoustic Wave Devices

There are various transduction mechanisms used by acoustic sensors. For some sensors, an acoustic wave is generated in and/or from the device and its characteristics

are altered in response to changes in the medium in contact with the device surface. Thus, the transduction principle is based on changes in the acoustic wave velocity or amplitude [8,10,34]. Such use of acoustic waves in sensor devices requires generation of the wave, circuitry to couple the electrical signal and mechanical response, as well as a means of measuring the wave perturbation [11].

Acoustic wave devices generally possess a piezoelectric layer with patterned metal electrodes (transducers) on its surface [11]. Piezoelectrics can be used to convert mechanical energy into electrical energy, and vice versa. Thus, if a voltage is applied to a piezoelectric crystal, a strain will result in the material. While probably the most common method, piezoelectricity is not the only mechanism of operation for these devices. Electrostrictive, magnetostrictive, as well as photothermal methods can be used to generate acoustic waves [11]. Acoustic wave devices operate over a frequency range extending from less than one to more than 1000 MHz [8]. The crystal orientation, piezoelectric film thickness, and metal transducer dimensions dictate the type of acoustic wave generated and the sensor resonant frequency.

Metal transducers are used to excite acoustic waves in the acoustic wave device medium. They may consist of simple circular patterns on the top and bottom of the piezoelectric plate surfaces or they may consist of more complex interdigital metal patterns. Interdigitated transducers (IDTs) usually have patterns similar to the one shown in Figure 5. When a spatially periodic electric field is applied to an IDT, a periodic mechanical strain will be generated in the underlying piezoelectric material because of piezoelectricity. Moreover, acoustic waves are created and will propagate away from the electrodes with wavefronts parallel to the IDT fingers [12]. The IDT period p is the

center-to-center distance between two adjacent electrode fingers of one comb. Optimal operation is provided when the wavelength λ is equivalent to *p*. Under these conditions, a sinusoidal voltage with frequency *f* will produce vibrations that interfere constructively [12]. Therefore, the synchronous or resonance frequency is $f = v/p$, where *v* is the wave (phase) velocity. The velocity is dictated by the cut of the crystal and the substrate material used.

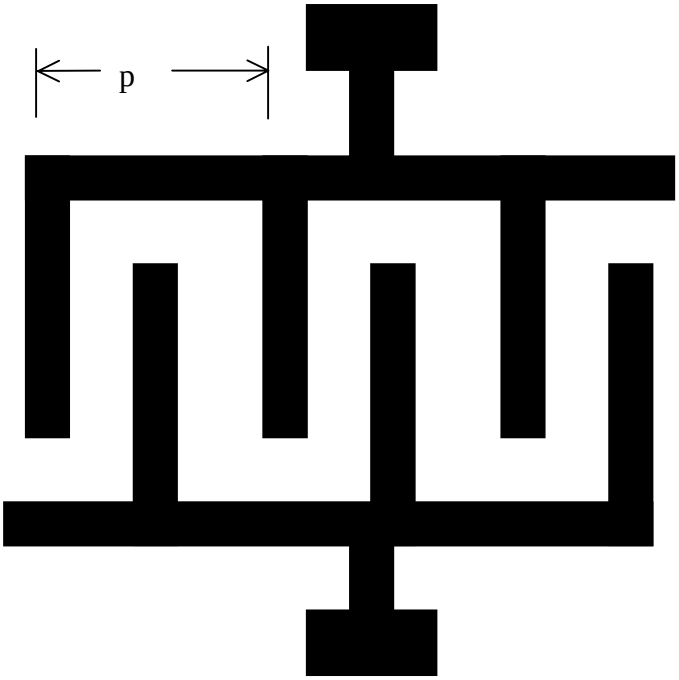

Figure 5. IDT design.

Many acoustic wave devices employ a delay line configuration that consists of two IDTs that have a center-to-center separation distance of *L*. In this set-up, one IDT generates the acoustic waves that propagate through the substrate and arrive at the second IDT after some time delay. An associated electric response is collected at the second

IDT, where it can then be recorded by data acquisition equipment. Therefore, any change in the response of the received waves is indicative of some change in the surface path through which the waves were transmitted [12].

2.2.1.1. Types

The most common acoustic wave devices include thickness-shear mode (TSM), surface acoustic wave (SAW), flexural plate wave (FPW), and shear horizontal plate mode (SH-APM) devices [8,10-12]. The waves that propagate in these devices usually have a transverse wave component, whereas the particle displacement will be normal to the direction of propagation. The particle displacement will be either parallel or perpendicular to the sensor surface [11].

TSM devices are characterized by acoustic waves that are transverse waves and propagate through the bulk material perpendicularly to the sensor surface [11]. As shown in Figure 6a, the particle displacement is parallel to the top and bottom surfaces. The wavelength of the fundamental and harmonic resonances are determined by the plate thickness d and is given by $\lambda = 2d/n$, where $n = 1$ for the fundamental resonance and $n = 3,5,7,\ldots$ for harmonic resonators [8, 11]. These devices usually have a fundamental mode of operation between 5 to 10 MHz [8]. TSM devices are considered one-port devices. The single port, which serves as both the input and output, is created by thin circular metal transducers located on each side of the plate. The sandwiched plate is usually AT-cut quartz.

Because of the orientation and piezoelectric properties of quartz, a shear deformation of the quartz crystal will occur if a voltage is applied to the electrodes [8]. Different

resonant thickness-shear modes can be excited in the crystal electrically wherein the displacement maxima will be found at the crystal surface. These devices are thus sensitive to surface perturbations, such as surface loading [8]. The most popular TSM device is generally known as the quartz crystal microbalance (QCM) [11], which will be discussed further in a subsequent section.

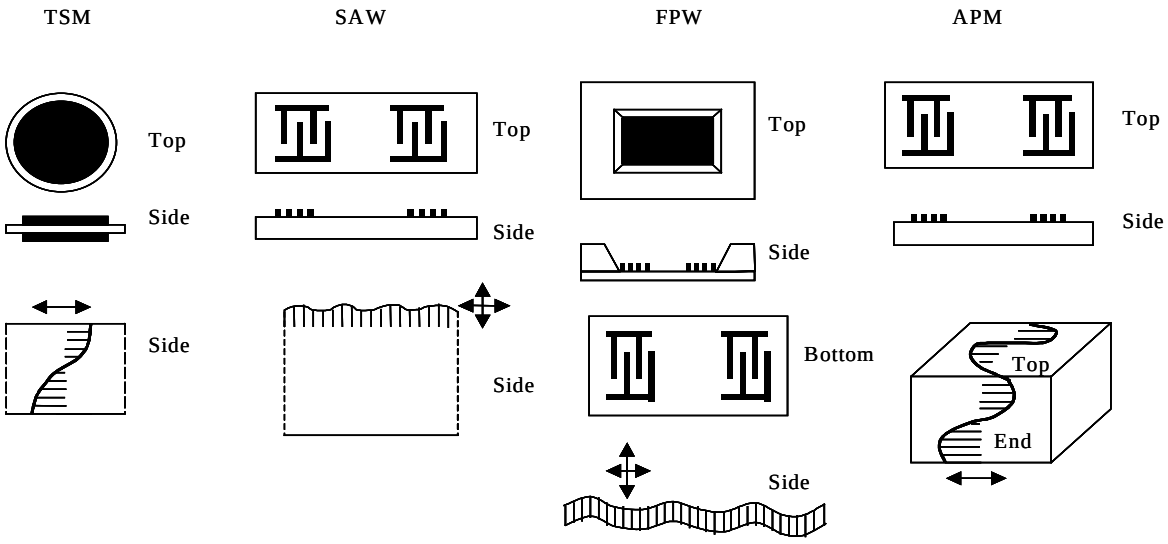

6(a). 6(b). 6(c). 6(d).

Figure 6. Acoustic wave device structures [11].

In SAW devices, acoustic waves generated by IDTs are usually Rayleigh waves whose energies are confined to a depth of approximately an acoustic wavelength thick in a piezoelectric material (Figure 6b). The piezoelectric material is generally thick and much greater than a wavelength. The surface particle moves in an elliptical and

retrograde path and possesses both surface-parallel and surface-normal components [8,10,11]. The surface-parallel component is parallel to the wave propagation direction and represents the longitudinal wave component. The surface-normal component is the shear component. SAW devices can be implemented with delay lines as shown in Figure 6b, where the IDTs are located at opposite ends of the surface of the plate. SAW devices can also be designed as resonators and require one or two IDTs for this application [11]. SAW devices typically operate at 30 to 300 MHz [11].

Another class of surface wave devices is known as surface transverse wave (STW) sensors. While not as common, they are similar in appearance to surface acoustic wave devices. STW devices, however, use a metal grating or thin film layer to confine the wave to the surface and lower the wave velocity. The particle displacement of these devices is parallel to the surface, yet perpendicular to the wave propagation [10-12].

Lamb waves are generated in thin plates (i.e., thickness is a fraction of the wavelength). Their particle motion, however, is similar to that of Rayleigh waves—the particles move in an elliptical path and have surface-parallel and surface-normal components [8, 10, 11]. Lamb waves generated by IDTs on thin plates establish a set of symmetric and anti-symmetric waves denoted by S_0, S_1, … and A_0, A_1,…., respectively [11]. The symmetry is in reference to the motion of the particle about the neutral plane of the plate. For very thin plates, only the two lowest order modes exist, S_0 and A_0 [8]. These are the only two modes that have wave velocities that are lower than that of SAW devices in the same medium. For the A_0 mode, the plate experiences flexure and is compared to a flag waving in the wind during the propagation of the wave [8]. Thus, these waves are called flexural plate waves (FPWs). They are depicted in Figure 6c.

The FPW sensor is implemented with a delay line. The IDTs excite the FPWs and cause the entire plate to be in motion. FPW devices typically operate at frequencies between 2-7 MHz [11].

SH-APM waves propagate in thin plates (on the order of a wavelength) and have particle displacements that are usually parallel to the device surface and normal to the direction of propagation (Figure 6d) [11]. Because they lack a surface-normal displacement component, SH-APM waves can propagate in liquids and thus are used for many applications for liquid sensing. The bulk of the plate of SH-APM devices serve as acoustic waveguides and confine the waves between the upper and lower surfaces of the plate as the wave propagates. The devices usually operate at 25-200 MHz [811.

2.2.1.2. Parameter Sensitivity

As previously noted, acoustic devices are usually sensitive to parameters that will perturb mechanical properties of the wave and/or its electric field [10]. Changes in the acoustic wave velocity can result from the addition of mass as well as from changes in the medium contacting the surface. If the acoustic wave device is placed in an oscillating circuit, changes in the oscillation frequency can be used to determine changes in the wave velocity. Changes in the acoustic wave amplitude are indicative of attenuation of the wave by the adjacent medium, thus signifying physical changes in that medium [11]. Such amplitude changes can be measured by equipment such as a vector voltmeter of network analyzer.

Acoustic wave devices have been used for various applications, including chemical and gas flow sensing and film thickness monitoring. In [35], a chemical sensor was

reported that employs surface acoustic waves to monitor the concentration of different gases. This device is composed of an oscillator circuit. A thin film that selectively absorbs the investigated gas is used to coat the surface of the sensor. The mechanical and electrical properties of the surface are altered as a result of sorption of the gas. Thus, the time delay of the delay line changes, as does the frequency. The frequency shift is used as a measure of the sampled gas concentration.

The temperature dependence of acoustic waves can be used to realize a SAW sensor that measures gas flow rates. Such a device was described in [10] and was composed of a delay line that was fabricated on 128^{o}-rotated Y-cut $LiNbO_3$. A substrate heater or acoustic absorber used to convert RF energy into heat, heats the delay line to a temperature above that of the surrounding atmosphere. Convection causes the heat to be removed as gas flows over the sensor. Thus, the surface temperature is reduced and the acoustic velocity is changed. This results in a shift of the oscillator circuit's frequency.

Thickness-shear mode sensors are generally known as quartz crystal microbalances (QCM). QCM devices have been used for deposition monitoring of thin metal films in vacuum systems since the late 1960s [29]. They use mass loading as the sensing operation. A frequency shift is proportional to the mass of the film. This information combined with the film density and acoustic impedance, enables the film thickness and deposition rate to be determined [11].

2.2.2. Silicon Microphones

Some acoustic sensors are categorized as microphones (operate in air) or hydrophones (operate in fluids). These sensors detect changes in mechanical pressure

over various frequency ranges [34,36]. Based on the relationship determined between the parameter of interest and pressure, a measurement of the desired parameter can be obtained. Most of these devices use bendable membranes or beams as the sensing element. IC and micromachining fabrication techniques provide the creation of extremely thin beams and membranes, thus enabling them to be highly sensitive to a measurand such as pressure. The deflections resulting from applied acoustic pressure are converted to electrical signals that can be measured with electrical equipment [34]. These devices are traditionally fabricated in silicon.

2.2.2.1. Types

Microphones use moving diaphragms or membranes that vibrate as a result of an incident pressure. They incorporate some sensing mechanism to convert the deflections into an electrical signal. There are various types of microphones that differ based on their diaphragm design and sensing mechanism. This establishes a wide range of microphones with a wide range of frequency bandwidths, sensitivities, dynamic ranges, and directional characteristics [34]. Acoustic sensors that are categorized as silicon microphones include capacitive, piezoresistive, piezoelectric, and optical waveguide sensors [34, 36-40.

The most common silicon microphone is known as the capacitive or condensor microphone. This sensor is composed of a variable gap capacitor as shown in Figure 7. Capacitive microphones either are biased by an external DC voltage source (usually 20-200V) to generate a surface charge q or use an electret material [34,37-40]. Electret materials are permanently charged and eliminate the need for an applied voltage. Operation of this sensor is based on

$$V = \frac{q}{C} = \frac{qd}{\in_o A} \tag{6}$$

where V is the voltage across the capacitor, q is the electric charge on the capacitor, C is the capacitance, d is the thickness of the air gap between the plates, $\in_o$ is the permittivity constant, and A is the area under the capacitor plates [34]. A pressure applied to the sensor diaphragm (at a constant charge) changes d, causing C to change. As a result, the voltage V will change. The change in V is proportional to the displacement of the diaphragm.

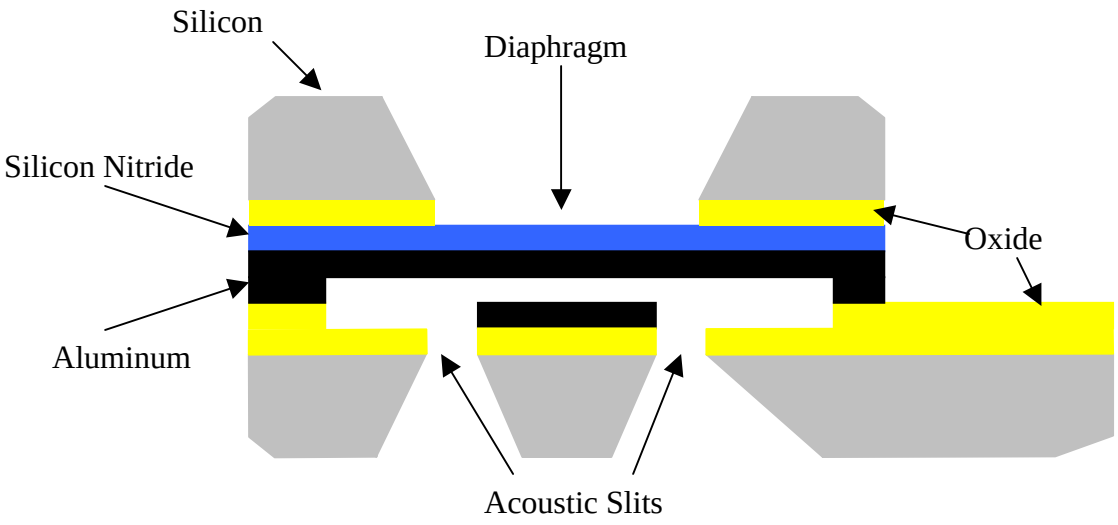

Figure 7. Capacitive microphone.

The microphone sensitivity of a capacitive microphone is dictated by the magnitude of q produced by the external voltage. This voltage needs to be very large to obtain high sensitivities. This, however, may lead to a lower dynamic range and a smaller shock resistivity [34]. Figure 7 shows that the air gap is connected to a large back cavity by slits. This is required to lower the stiffness of the air gap. Therefore, when the

membrane is displaced because of an applied pressure, the air in the gap streams and damping occurs [39]. Moreover, high frequency sensitivities will be greatly reduced because of the air-streaming resistance [13, 34]. Capacitive microphones have reported capacitances of 1-20 pF, sensitivities of 0.2 to 25 mV/Pa, and frequency responses between 10 Hz to 120 kHz [13, 38-39].

In piezoresistive microphones, four polysilicon resistors are fabricated on a silicon diaphragm and are usually connected in a Wheatstone bridge configuration as shown in Figures 8 and 9 [13, 34]. Figure 8 shows a cross-sectional view of the piezoresistors on the membrane and Figure 9 is a top view depicting the position of the four resistors (*R1, R2, R3, and R4*).

Piezoresistive materials experience a change in resistance as a result of an induced strain. Thus, an applied mechanical pressure or stress will be proportional to a change in resistance ΔR

$$\frac{\Delta R}{R} = \pi_l \sigma_l + \pi_t \sigma_t \qquad (7)$$

where π is the piezoresistive coefficient and σ is the stress. The subscripts *l* and *t* denote the longitudinal and transverse directions (with respect to the current flow), respectively [16, 34].

In a common design of this microphone, two resistors are positioned so that they sense stress that is in the same direction of their current flow. The other two are oriented to sense stress that is perpendicular to their current flow. Therefore, when the membrane is displaced, the value of two resistors increases while the value of the other two decreases [13, 16, 41]. If all of the resistors are initially equal and have identical resistance changes (except for a difference in sign) due to an applied stress, the output

voltage $\Delta V = V_{in}*(\Delta R/R)$, where V_{in} is the bridge-input voltage and R is the zero-stress resistance [13,16,41].

While piezoresistive microphones tend to possess low sensitivities, they typically generate a low output impedance [38, 40]. These microphones also exhibit a temperature dependence, which may pose problems for various applications. Piezoresistive microphones have sensitivities of 1 nV/Pa to 25 μV/Pa and frequency responses between 100 Hz and 5 kHz [16, 38, 40].

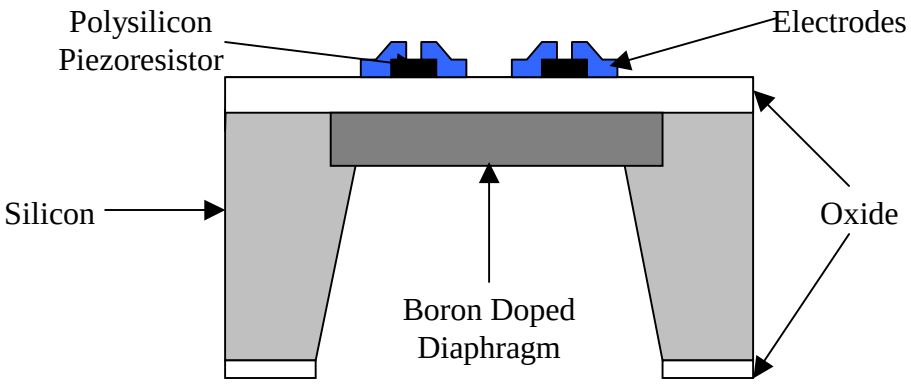

Figure 8. Piezoresistive microphone.

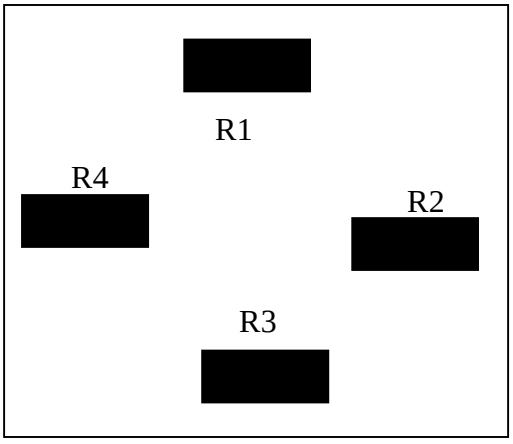

Figure 9. Position of piezoresistors on microphone membrane.

An example of a piezoelectric microphone is shown in Figure 10. This type of sensor is the basis of the thesis work presented here and thus, a more in-depth description of this microphone will be provided in Chapter 3. However, the author wishes to note that piezoelectric sensors employ a thin membrane and a piezoelectric layer. The operation of piezoelectric microphones is based on the piezoelectric effect, where a mechanical stress deforms the membrane and generates an electric charge on the piezoelectric layer. These microphones have sensitivities from 25 to 920 μV/Pa and frequency responses from 10 Hz to 45 kHz [38, 39].

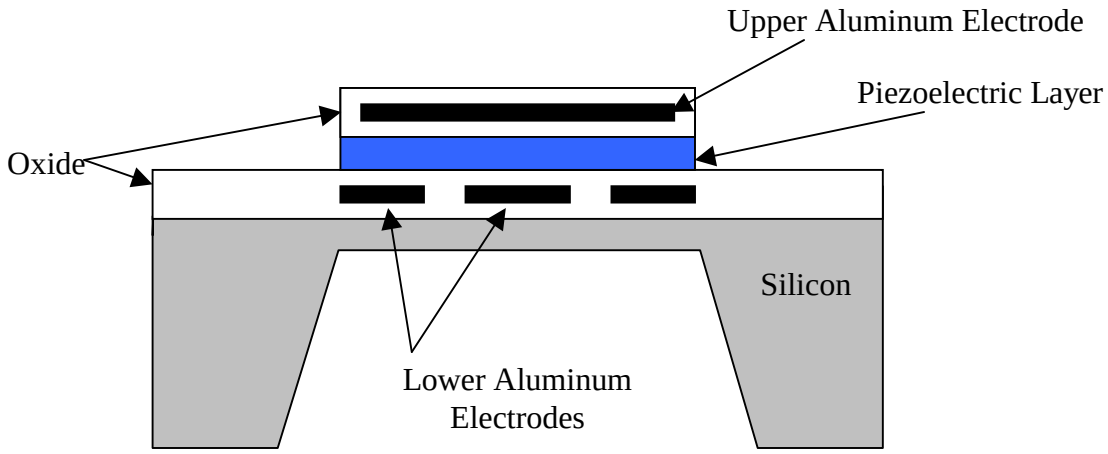

Figure 10. Piezoelectric microphone.

Optical-waveguide microphones are based on the fact that sound pressure changes the medium through which light propagates, thereby changing the phase or amplitude of the light wave [25, 26]. There are various optical-waveguide microphones that have been described in literature and one such sensor is depicted in Figure 11. This microphone has a two-chip design and implements a membrane chip and a silicon waveguide chip [38]. Optical fibers are used to couple the light into the waveguide chip and receive light once it has been transmitted through the waveguide. The hollow waveguide is enclosed by the bottom gold layer of the waveguide chip, the top gold membrane chip layer, and the silicon ridge (height of 5 μm) on the sides. If a mechanical pressure is applied to the membrane chip, the height of the hollow area of the waveguide is changed, modulating the phase and amplitude of the light in the waveguide before it is received by the receiving fiber. A Mach-Zehnder interferometer can be use to measure the phase modulation [38].

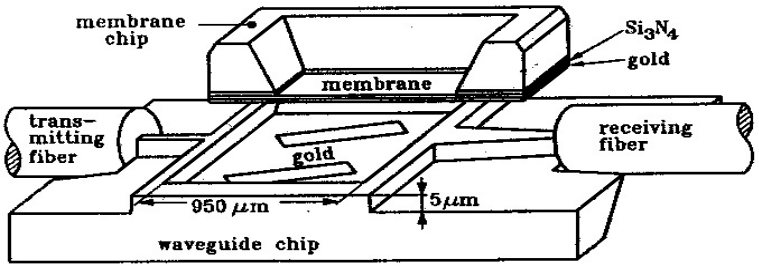

Figure 11. Optical-waveguide microphone [38].

2.2.2.2. Parameter Sensitivity

As previously mentioned, silicon microphones are sensitive to changes in mechanical pressure. The mechanism used to sense these changes can rely on capacitive, piezoresistive, piezoelectric, or optical responses and has been outlined for the various microphones in Section 2.2.2.1. The changes in pressure are usually converted into an electrical response (capacitive, piezoresistive, piezoelectric microphones) or an optical response (optical-waveguide microphone). These changes are usually measured by equipment such as voltmeters, network or spectrum analyzers, or interferometers.

2.2.3. Acoustic Sensors in Semiconductor Process Monitoring

In recent years, a group of Stanford University researchers has pioneered the use of acoustic methods to monitor semiconductor processes. They have provided sensors for *in-situ* thickness monitors and wafer temperature mapping in process chambers, as well as photoresist process monitoring. Some of their relevant work is outlined below.

A vital element of rapid thermal processing (RTP) technology is the need to accurately measure and map the wafer temperature. In [42], Lee et al. use the temperature dependence of acoustic wave propagation for *in-situ* temperature measurements. The devices used are FPW transducers mounted to quartz pins. These pins are in contact with the back of the wafer being processed. The center frequency of the transducers is 300 kHz. The acoustic wave propagates the (100) wafer plane in the RTP chamber. The time of flight of the lamb wave across the wafer is used to derive the temperature measurements. By incorporating an array of transducer pins around the

periphery of the wafer and using tomographic inversion techniques, the authors were able to map the temperature of the entire wafer during processing.

The Stanford researchers have also used FPW devices as *in-situ* film thickness sensors. The mechanism of this sensor relies on the fact that the velocity of the lamb wave propagating in a wafer will be changed by the thin film coating on the wafer surface [43]. The types of film monitored are not limited (as with optical sensors) and can include transparent or opaque films, as well as metals and insulators. In this application, the FPWs are excited and detected by piezoelectric transducers on the bottom of quartz rods. These rods contact the back surface of the silicon wafer. The operating frequency of the sensor is 200 kHz. The time delay of the signal transmitted is measured and film thickness information is derived. These measurements were performed in Al films in a sputtering system.

This group also developed an ultrasonic sensor for *in-situ* monitoring of photoresist processing [44]. This sensor is used to monitor changes in the photoresist thickness during development. Process monitoring is provided by exciting high frequency longitudinal waves in silicon via a buffer rod. The changes in the reflection coefficient of the acoustic wave reflected from the photoresist/silicon interface are measured and used for process monitoring.

These applications demonstrate the potential of using acoustic methods for monitoring and control of semiconductor manufacturing processes. The techniques described above, however, require direct contact of the sensor with the silicon wafer. The method used in this thesis research eliminates that requirement.

2.3. Summary

This chapter reviews existing *in-situ* process monitoring techniques. The methods outlined are based on either optical or acoustic sensors. Process sensors are required to monitor critical semiconductor process parameters in order to provide for high device yields and low processing costs.

Currently, most *in-situ* process sensors are optical in nature. Optically based sensors such as optical emission spectroscopy (OES), interferometry, ellipsometry, and optical pyrometry were outlined in this chapter. The advantages, limitations, and current applications of these sensors were presented.

Acoustic sensors are of great interest as process sensors because they are small, cheap, reliable, and known to sense many of the parameters relevant to process monitoring of semiconductor manufacturing equipment and processes. These sensors could be used in addition to or instead of optical sensors. Therefore, various acoustic wave devices and microphones were described in this chapter. The acoustic wave devices presented include thickness-shear mode (TSM), surface acoustic wave (SAW), flexural plate wave (FPW), and shear horizontal plate mode (SH-APM) devices. The silicon acoustic microphones presented include capacitive, piezoresistive, piezoelectric, and optical-waveguide sensors. A section detailing reported usage of acoustic sensors in semiconductor process monitoring was also included.

Chapter 3 will describe the acoustic sensor that was developed, designed, and fabricated in this thesis . The theory and operation of the sensor will be presented. The sensor is a piezoelectric microphone, therefore, the piezoelectric effect will be discussed

as well as factors in selecting piezoelectric materials. The equivalent circuit model used to represent the sensor will also be described.

CHAPTER 3

A PIEZOELECTRIC SENSOR FOR PROCESS MONITORING

In this thesis, a piezoelectric sensor was developed to provide process monitoring of semiconductor manufacturing processes. Piezoelectric films are used to convert mechanical energy into electrical energy and vice versa. Therefore, they are vital components of electromechanical transducers. These devices are desirable because they are usually one-chip devices that have a simple design. Piezoelectric sensors are fabricated using IC and bulk micromachining techniques. Therefore, the fabrication process is based on well-established, repeatable steps. The use of piezoelectric microphones eliminates air-gap losses associated with other acoustic sensors. Also, an excitation voltage or supply current is not required.

3.1. Sensor Theory and Operation

Piezoelectric devices are generally composed of a piezoelectric layer sandwiched between two electrodes, as shown in Figure 12. The transduction of piezoelectric sensors is based on the piezoelectric effect: a mechanical stress (pressure) applied to certain crystals produces a mechanical deformation (strain) in the crystal and results in an electric charge [16,37]. This phenomenon was first discovered in 1880 by Pierre and Paul-Jacques Curie. The word “piezo” is derived from the Greek word for “to press” [21,32]. Piezoelectrics exhibit the direct, as well as the converse effect, where an applied voltage causes strain in the crystalline material. Thus, the piezoelectric effect can be

employed by sensors to sense mechanical stress, as well as by actuators to actuate the surrounding medium by converting electrical energy into mechanical energy [13]. However, the high voltage (often > 1000V) required to obtain displacements with values in the micron range limit their use for many actuator applications [13]. Though in some instances stacked actuators or mechanical motion amplification is used to resolve these limitations.

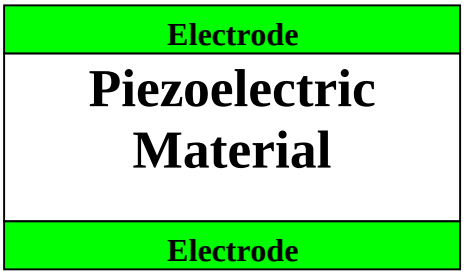

Figure 12. Simple piezoelectric structure.

Figure 13 gives a simplified illustration of the piezoelectric effect in quartz crystal (SiO_2). In quartz, each oxygen atom has two negative charges while each silicon atom has four positive charges. The atoms are arranged as a helix, and the oxygen atoms are grouped as pairs. There are three atoms of silicon and 6 atoms of oxygen (three pairs) located alternately around the helix for each crystal cell [34]. In the absence of mechanical stress, the crystal will be neutral (Figure 13a). However, when a stress is applied, the crystal lattice is deformed and the atoms are displaced establishing a charge (Figure 13b).

When centrosymmetric crystals such as silicon are strained, there is no movement of the centers of the negative and positive charges with respect to one another. Moreover,

the piezoelectric effect is found only in non-centrosymmetric crystals-crystals lacking a center of inversion. In these crystals, each unit cell of the crystal is oriented so that its electric dipole is aligned and the crystal is electrically neutral [16,34]. However, when a mechanical force is applied to the crystal, the crystal lattice is deformed (strained), causing charges to accumulate on the surface. Thus, a potential difference develops across the crystal. If electrodes are placed on the top and bottom surfaces of the crystal, as shown in Figure 12, the piezoelectric sensor can be considered a capacitor. These electrodes can measure the voltage, $V = \frac{Q}{C}$, across the capacitor, where Q is the charge generated as a result of the force and C is the capacitance of the piezoelectric sensor.

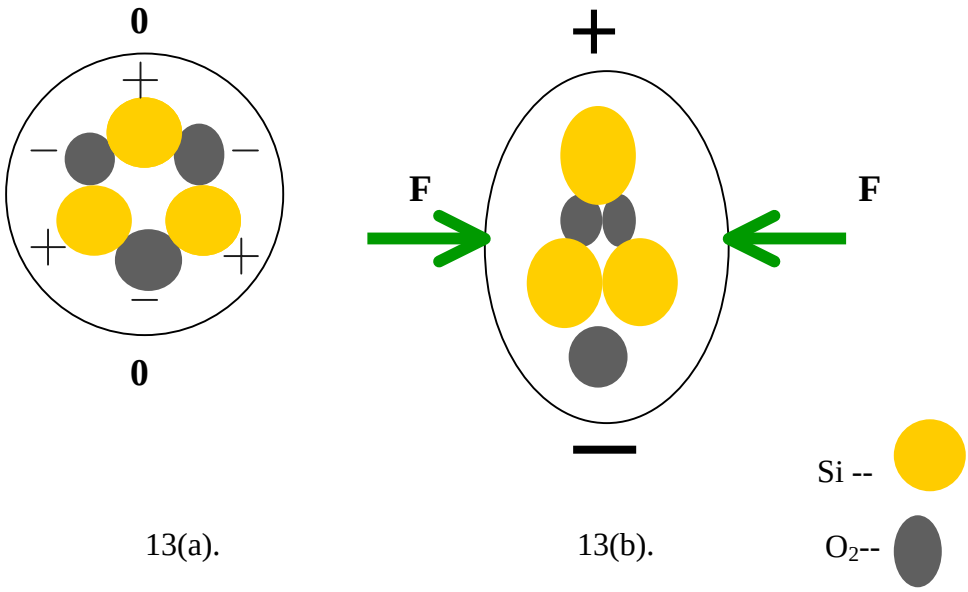

13(a). 13(b).

Figure 13. Piezoelectric effect in quartz.

Piezoelectricity can be more thoroughly explained by considering the equations describing the interaction of electrical and mechanical phenomena. A stress σ in a material is related to the strain ε by

$$\varepsilon = S\sigma \tag{8}$$

where S is the compliance [8,16]. This is the one-dimensional (1-D) mechanical constitutive equation known as Hooke's Law. Piezoelectrics are governed by electrical parameters as well. If a voltage is applied across a dielectric, an electric field E is generated and the following 1-D constitutive equation results:

$$D = \in_r E \tag{9}$$

where D is the electric displacement and $\in_r$ is the relative permittivity. Equation (2) can also be given by

$$D = \in_o E\,(1 + \chi) = \in_o E + P \tag{10}$$

In this equation, $\in_o$ is the permittivity of vacuum, χ is the electrical susceptibility, and P is the polarization [16].

Equation (8) denotes only mechanical parameters, while Equation (9) gives only electrical parameters. Because of the nature of piezoelectrics, however, these constitutive equations have to be coupled together to describe the interaction of stress, strain, charge displacement, and electric field. Therefore, for a piezoelectric layer with σ and E in the same direction, one can write

$$D = d\sigma + \in^{\sigma} E \tag{11}$$

where d is the piezoelectric coefficient with units of C/N for this equation and $\in^{\sigma}$ is the permittivity measured at a constant (usually zero) stress [46]. Equation (11) is based on the direct piezoelectric effect. The converse effect can be represented by

$$\varepsilon = S^E\sigma + dE \tag{12}$$

In Equation (12), S^E is the compliance measured at a constant electric field and d is given in m/V. These two equations are known as piezoelectric constitutive equations, represented here in 1-D. The second term of Equation (11) and the first term of Equation (12) are always valid, even for nonpiezoelectric materials. The first term of Equation (11) and the second term of Equation (12) are due to piezoelectric coupling [46].

Equations (11) and (12) describe only one form of the piezoelectric constitutive equations. This form can arbitrarily be called the "strain-charge" form, since it is used to determine strain and charge density displacement. Equations (11) and (12) can be rearranged to yield three other forms: the "stress-charge," "strain-voltage," and "stress-voltage" forms [47]. These alternative equations may be necessary, depending of the form of the piezoelectric coefficient given. The coefficient may have units of C/N, C/m^2, m^2/C, N/C, V/m/N, V/m, m/V, or N/V/m [16].

If no external electric field is applied to the piezoelectric layer, a polarization P resulting from a stress σ can be determined from Equations (10) and (11) as

$$P = d\sigma \tag{13}$$

Without an applied stress, Equation (12) yields the strain ε resulting from an electric field E as

$$\varepsilon = dE \tag{14}$$

So far, only 1-D calculations have been discussed. For a given piezoelectric crystal, however, the piezoelectric response has to be extended to all crystal axes and directions of interaction, as piezoelectric materials are anisotropic. Taking into account the orientation dependence of the piezoelectric effect, Equation (14) can be written as

$$\varepsilon_j = \sum_{i=1}^{3} d_{ij} E_i \tag{15}$$

and Equation (13) can be expressed as [16]

$$P_i = \sum_{j=1}^{6} d_{ij} \sigma_j \tag{16}$$

In Equations (15) and (16), i = 1, 2, and 3 and represent the x, y, and z axes, respectively, where i denotes the direction of polarization and is usually perpendicular to the electrodes, and j = 1, 2, 3,…6 and signifies the indices pertaining to the mechanical stress or strain. Because of crystal symmetry, j actually represents a reduced index notation whereas xx = 1, yy = 2, zz = 3, $yz = zy$ = 4, $xz = zx$ = 5, and $xy = yx$ = 6 [9]. J = 1, 2, or 3 denotes a normal stress and strain and j = 4, 5 or 6 signifies a shear stress or strain. Equations (11) and (12) are modified to address the piezoelectric orientation dependence as well and are now expressed as

$$D_i = d_{ij}\sigma_j + \in^{\sigma}_{ij} E_i \tag{17}$$

$$\varepsilon_j = S^{E}_{ij}\sigma_j + d_{ij}E_i \tag{18}$$

respectively.

Using Equation (16) to describe the response of the sensor shown in Figure 1, the piezoelectric coefficient d_{ij} indicates the charge density generated on the electrodes per the applied stress $\left(\frac{D_i}{\sigma_j}\right)$. The stress σ_j is the result of the applied force (F) or applied mechanical pressure (F/A). The charge generated Q_s on the surface is equivalent to the polarization P_i times the area of the surface. Therefore, the relationship between an applied mechanical pressure ($\propto \sigma$) and Q_s is deduced.

3.2. Piezoelectric Materials

Silicon is not piezoelectric; therefore, silicon-based sensors must use a piezoelectric layer to exploit this effect. Popular IC-compatible piezoelectric materials are quartz, lead zirconate titanate (PZT), polyvinylidene fluoride (PVDF), aluminum nitride (AlN), zinc oxide (ZnO), barium titanate ($BaTiO_3$), and lithium niobate ($LiNbO_3$). Some of these piezoelectrics, such as PVDF, are not initially polarized and must be "poled" (artificially polarized) in a strong electric field to align the dipoles [13,16,34].

Most piezoelectrics possess pyroelectric as well as ferroelectric properties [9,34]. Pyroelectric materials generate an electrical output in response to temperature change. Depending on the application of the piezoelectric device, the pyroelectric properties can be either advantageous or unfavorable. All pyroelectric materials are piezoelectric. However, all piezoelectric materials are not pyroelectric [24]. There are 32 classes of crystals; 21 of those classes are noncentrosymmetric and 10 of those classes possess pyroelectric properties [34]. Ferroelectric materials possess a spontaneous electrical polarization that can be changed by an applied electric field [9]. Similar to pyroelectric materials, all ferroelectrics are piezoelectric but the opposite is not necessarily true. Strong electrostriction is present in ferroelectric materials. Electrostriction is a phenomenon whereas a material is strained when an electric field is applied. This property involves electron spin, whereas piezoelectricity is associated with the ionic structure of the crystal [24].

Piezoelectrics are generally characterized by various parameters. One is the piezoelectric coefficient (or constant). The piezoelectric coefficient d_{ij} used in Equations (11), (16), and (17), for example, denotes the piezoelectric layer's sensitivity to stress

[32,35]. It describes the surface charge generated on the *i* crystal axis resulting from stress on the *j* axis. The piezoelectric coefficient may be given in different forms and denoted by various variables. Table 2 summarizes the different forms of the piezoelectric

Table 2. Piezoelectric constitutive equations and definitions of piezoelectric parameters [16].

Piezoelectric Equation	Definition of Constants	M.K.S. Units
$D = d\sigma + \in^{\sigma} E$	d= charge density developed / applied stress	C/N
$D = e\varepsilon + \in^{\varepsilon} E$	e= charge density developed / applied strain	C/m^2
$E = -g\sigma + \frac{D}{\in^{\sigma}}$	g= field developed / applied stress	V/m/N
$E = -h\varepsilon + \frac{D}{\in^{\varepsilon}}$	h= field developed / applied strain	V/m
$\varepsilon = dE + S^{\sigma}\sigma$	d= strain developed / applied field	MV
$\varepsilon = eD + S^{D}\sigma$	g= strain developed / applied charge density	m^2/C
$\sigma = -eE + Y^{E}\varepsilon$	e= stress developed / applied field	N/V/m
$\sigma = -hD + Y^{D}\varepsilon$	h= stress developed / applied charge density	N/C

coefficient and piezoelectric constitutive equation. Piezoelectrics can also be described by the electromechanical coupling coefficient, *k*, which denotes the efficiency of a

particular material in converting electrical energy into mechanical energy [16,34]. It is given by

$$k_{ij} = \sqrt{g_{ij} e_{ij}} = \sqrt{\frac{d_{ij}^2}{\varepsilon^{\sigma} S^{E}}} \tag{19}$$

where g_{ij} is a piezoelectric coefficient that is equivalent to d/ε^{σ} and e_{ij} is another piezoelectric coefficient equivalent to d/S^{E}. In comparing piezoelectric materials, other factors for consideration include adhesion to the substrate, cost, resistance to environmental effects, and IC process compatibility [16].

Ease of processing is an important issue. Manufacturing of certain ceramic piezoelectrics, such as PZT, may require complicated processing steps. One process used to produce PZT first starts with the milling and mixing of various metal oxide powders to form a powder with a chemical composition close to that of the final composition. This powder is then mixed with an organic binder and shaped into a cake. The organic binder is baked out and the cakes are heated to obtain the desired chemical reaction. The cakes are then cooled to form the crystalline structure [34]. Some piezoelectric polymers, such as PVDF, are not naturally poled. Unlike, quartz, whose crystal cells are naturally aligned along the crystal axes so that it is sensitive to mechanical stress, the electric dipoles of these materials are initially randomly oriented [34]. Thus, they will have to be "poled" to receive piezoelectric characteristics. Prior to poling, these piezopolymers are usually in a powder form that is dissolved in a solution, spun onto a wafer, and then annealed. One method of poling, thermal poling, entails heating the material to a temperature just above its Curie temperature. Above the Curie temperature, the dipole alignment of poled materials disappears. Heating of the material helps increase the

mobility of the crystal's molecular structure [34]. The material is placed in a strong electric field and many of the electric dipoles line up parallel with the field direction. The material is then kept under the electric field as it is cooled down. At this point, the alignment of the dipoles is "frozen" [34]. Another poling method is known as corona discharge poling. In this method, the wafer coated by the piezoelectric material is contacted by an electrode that has a corona discharge of several million volts per cm [34]. Thus, an electric field is generated and the dipole orientation will be aligned.

ZnO is one of the more popular piezoelectrics. It is implemented using common thin film deposition procedures. It is usually deposited using a planar plasma magnetron sputtering system, which prevents the need for poling or tedious mixing and curing associated with other methods. The c-axis of ZnO exhibits the strongest piezoelectricity, and therefore, ZnO is deposited so that this axis is perpendicular to the surface [13]. ZnO is the material chosen for the acoustic sensor described in this thesis. It has relatively good piezoelectric coefficients and was deposited on available equipment in the Microelectronics Research Center (MIRC) at the Georgia Institute of Technology. ZnO processing poses the potential of cross-contamination, however, and attention must be given to the sequence in which the ZnO deposition is performed.

3.4. Circuit Model

The simplified electrical equivalent circuit of the sensor is shown in Figure 14a. It consists of a charge generator in parallel with the capacitance of the sensor, C_s, and the resistance resulting from leakage through the dielectric, R_s. The circuit can also be represented by a voltage source, V_s, in series with C_s (Figure 14b). V_s is given by Q_s/C_s,

where Q_s is the stress-induced charge on the piezoelectric surface. Because the leakage resistance, R_s, is very large ($10^{12} – 10^{14}$ Ω), the output impedance will be very high [34]. Consequently, the output signal must be conditioned prior to being analyzed by data acquisition equipment. The high leakage of the sensor slowly discharges Q_s and reduces V_s. This generally prevents the device from maintaining a static response and confines it to measuring dynamic stresses [34,45,48]. Chen et al. [48] found that a virtually DC response could be obtained by burying the piezoelectric in insulating layers, however.

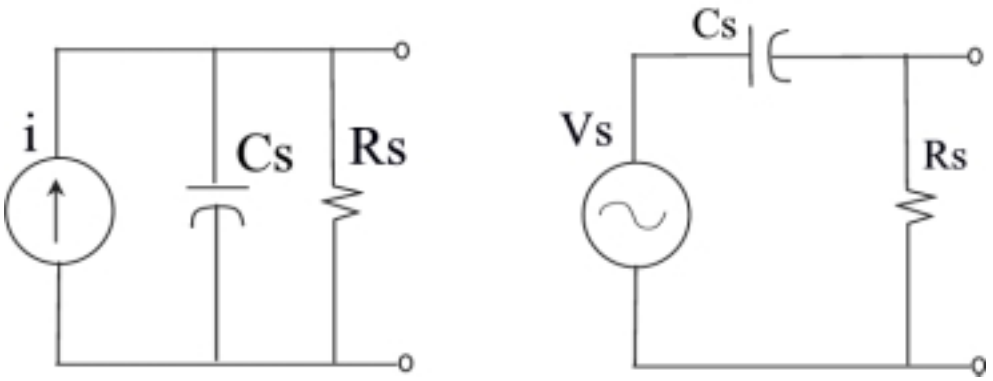

14a. 14b.

Figure 14. Sensor equivalent circuits.

Charge or voltage amplifiers are usually used in interfacial circuits between the piezoelectric sensors and electronic measurement equipment. They convert the high impedance of the sensor to a low impedance voltage signal and amplify and filter the signal as well. One disadvantage of a voltage amplifier is that the output signal is influenced by the capacitances of the connecting cable and probes, as well as the amplifier input [45,49]. This research utilizes a FET charge amplifier from ThermOptics (DN 620). A charge amplifier transforms the charge Q_s into a proportional voltage V_o.

Figure 15 shows the equivalent circuit employing a charge amplifier. The amplifier is an inverting amplifier with a feedback capacitance and resistance, C_{fb} and R_{fb}, respectively. This circuit is arranged so that the amplifier input impedance and the stray capacitances resulting from the cable (C_c) and probes (C_p) are connected between ground and the virtual ground at the amplifier inverting terminal. Thus, the voltage across the capacitors and amplifier input impedance is negligible. The output voltage, therefore, will depend on the charge generated by the sensor.

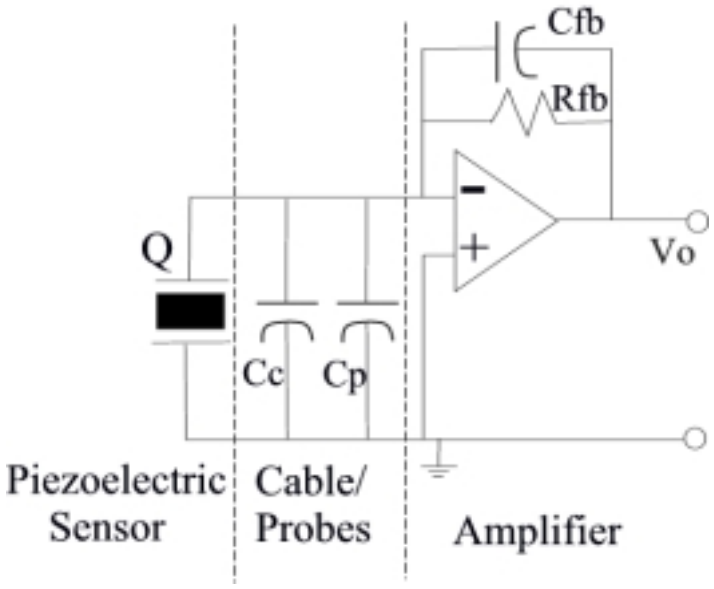

Figure 15. Sensor circuit employing a charge amplifier.

A small input current is necessary to bias the input transistors of the amplifier [50]. Therefore, a large feedback resistor, R_{fb}, is needed to provide a DC path for the amplifier input bias current. Otherwise, this current would charge C_{fb} and result in drift at the output [49]. For an alternating sensor response, the output of the circuit is given by

$$V_o = \frac{-(j\omega Q_s e^{j\omega t})C_N R_{fb}}{(1+j\omega R_{fb}C_{fb})(C_s+C_N)} \tag{20}$$

$$\text{V}_\text{o} \text{ approaches } \frac{-Q_s e^{jwt} C_N}{C_{fb}(C_s + C_N)} \text{ when } j\omega R_{fb}C_{fb} >> 1 \tag{21}$$

where C_N is the capacitance due to the silicon nitride layer. Equation (14) describes the normal operating condition of the circuit [45]. The cut-off frequency or lower bandwidth limit is given by,

$$f_c = \frac{1}{2\pi R_{fb}C_{fb}} \tag{22}$$

For R_{fb} = 1 GΩ and C_{fb} = 11 pF, f_c equals 14.5 Hz. The output signal is greatly reduced below this frequency.

3.4. Summary

This chapter describes an acoustic sensor that uses the piezoelectric effect as its mechanism of operation. In the piezoelectric, effect a mechanical stress applied to a non-centrosymmetric crystal will produce a strain in the crystal and result in an electric charge. This charge is proportional to the stress applied. Such sensors are favorable because they do not have air gap losses and they eliminate the need for an excitation voltage or supplying current.

There are various materials that are naturally or artificially polarized and possess piezoelectric characteristics. Selection of a material for device applications is based on factors such as the sensitivity of the material to a given parameter, the material's coupling efficiency, adhesion to the substrate, associated costs, and ease of processing. The sensor described in this work uses zinc oxide, a popular piezoelectric material that can be deposited using common thin-film deposition techniques.

The electrical equivalent circuit representation of the piezoelectric sensor was also described in this chapter. Due to the nature of piezoelectrics, the sensor can be thought of as a charge generator. Because of the high output impedance of the sensor, a charge amplifier was use to convert the high impedance to a low impedance voltage signal and to amplify and filter the signal. The output voltage of the sensor circuit incorporating the interfacial circuitry was derived and presented in this chapter.

Chapter 4 will present the process used in fabricating this sensor. It describes the design of the sensor and finite element analysis used to model it. Micromachining technology and its importance in the creation of microsensors are presented. Finally, the process sequence used to realize the sensor is outlined.

CHAPTER 4

FABRICATION PROCESS

Chapter 3 described the theory and operation of a piezoelectric acoustic sensor. This chapter will focus on the design and fabrication of the sensor. To optimize its performance, the sensor was modeled using finite element analysis software. The results of this analysis were used for the design of the sensor. The mask-making procedure used in transferring the design onto the sensor membrane will also be described. As previously mentioned, the advantage of acoustic sensors is that they can be micromachined into/onto silicon using common IC and micromachining techniques. Therefore, micromachining technology is reviewed in this chapter. Finally, the process sequence followed in fabricating the acoustic sensor is outlined.

4.1. Sensor Design

The design of the sensor is based on that presented in [36] and [37]. It consists of a membrane, a piezoelectric layer, and segmented surface electrodes. A highly doped silicon layer was used for the membrane because silicon does not possess the tensile stress associated with silicon nitride or silicon dioxide layers [37, 51]. Because the elastic constants of ZnO are very low, the ZnO layer had to be thin relative to the silicon membrane thickness [51]. The ZnO layer was approximately 0.8 μm, and the silicon membrane was 3.5 μm thick. The thickness of the silicon was dictated by the high temperature constant source boron diffusion step. The ZnO was encapsulated by a silicon nitride layer, which helps to reduce surface charge leaks [48, 52]. The deflectable

diaphragm structure, which is the sensing element of the microphone, has an area of 1270 x 1270 μm^2. A cross-sectional view is shown in Figure 16.

The ANSYS finite element analysis software package was used to model the piezoelectric membrane [53]. The membrane can be modeled mechanically as a thin plate with clamped edges. Movement of the membrane due to sound pressure produces mechanical strain in the ZnO, and thus, produces a charge displacement between the silicon membrane and top electrodes [36, 51]. Using ANSYS, it was verified that under uniform loading, the diaphragm will experience the greatest bending stress in the middle and outer regions. The outer region of the membrane is under tension while the middle region is under compression [52]. Figure 17 is a plot of the *x*-component of the stress (σ_x) due to the surface loading. Taking the center of the membrane as the *x*-*y* axis, Figure 17 shows that σ_x is large along the edges of the membrane and (with opposite sign) in the center, with a maximum value at $x = \pm a/2$, $y = 0$ (where *a* is the value of the length of the side of the membrane). The plot of the *y*-component reveals that σ_y is large along the edges of the membrane and (with opposite sign) in the center, with a maximum value at $y = \pm a/2$, $x = 0$. Electrodes placed in these regions will be used to collect the surface charges of the ZnO and measure the output signal.

The concentric electrode design employed (shown in Figure 18) creates two ZnO capacitors (of approximately equal area) formed by the inner and outer electrodes. The highly conductive boron doped silicon membrane connects the inner and outer capacitors in series. This design was first demonstrated by Royer et al. [52, 54,55].

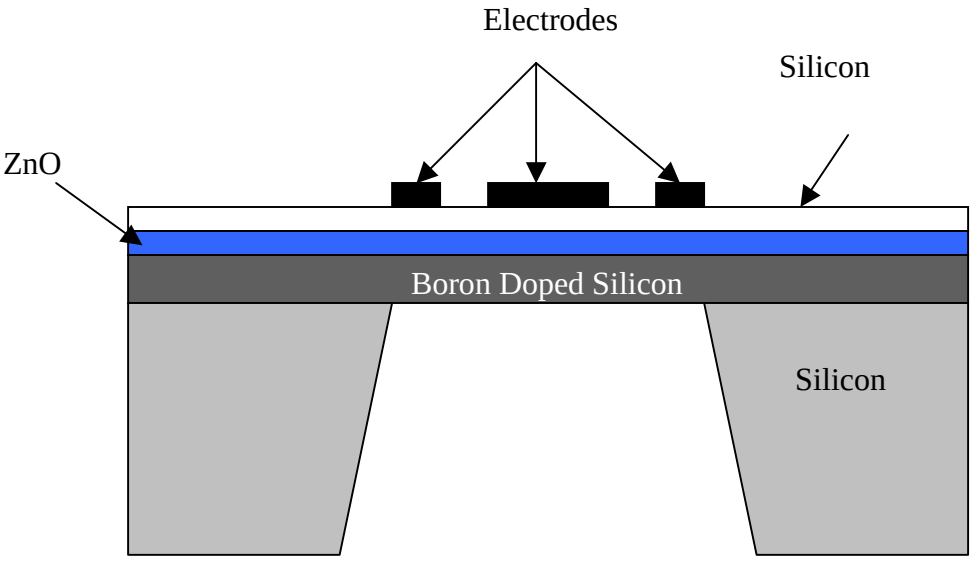

Figure 16. Cross-sectional view of piezoelectric acoustic sensor.

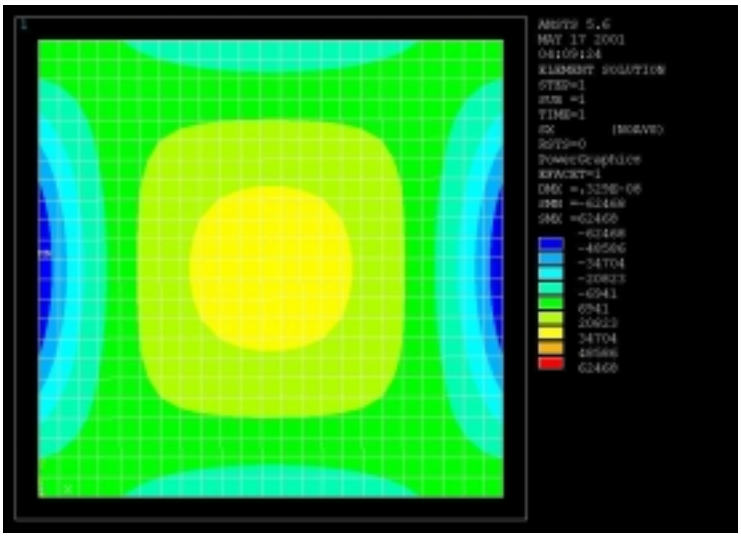

Figure 17. ANSYS plot of stress in x-direction.

Figure 19 shows the piezoelectric response generated in the capacitors. Because of the sign of the mechanical stresses in these areas, the piezoelectric signals of the central and outer regions are added in phase [16, 54]. Instead of including a large area with high and low strain regions, the segmented electrode shape includes smaller areas with high strain regions. Thus, sensitivity to pressure is also increased [48]. It should be noted that in order to connect the outer electrode regions of our acoustic sensor, some low strain areas (gray areas of Figure 18) were included and thus, the sensitivity may not be optimal.

ZnO has pyroelectric properties as well as piezoelectric properties. Pyroelectric materials produce surface charges in response to temperature variations [34, 52]. The strategic design of the concentric electrodes generates a pyroelectric response, as shown in Figure 20. Therefore, the output signal due to ZnO temperature variations cancel and the pyroelectric effect in this sensor is negligible.

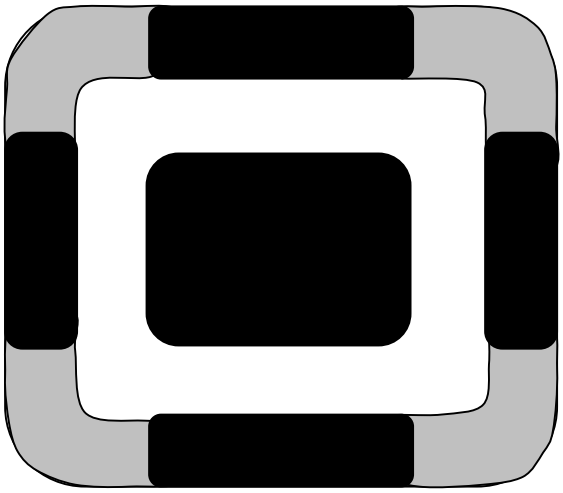

Figure 18. Electrode pattern.

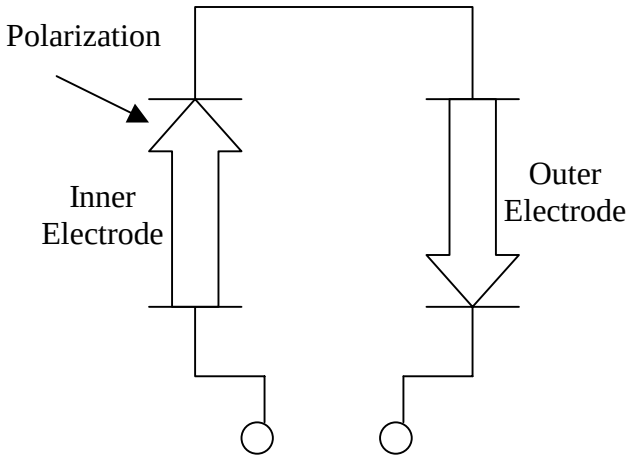

Figure 19. Piezoelectric response [16, 54].

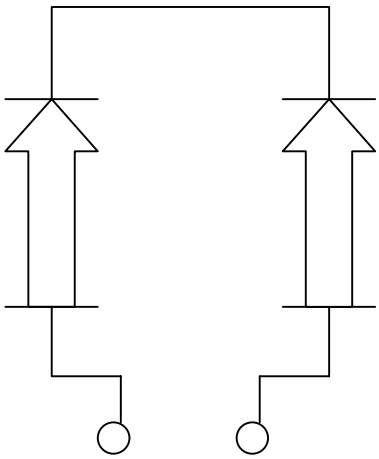

Figure 20. Pyroelectric response [16, 54].

4.2. Micromachining

The tremendous progress made recently with microsensors and microactuators is primarily due to the advances in micromachining technology. Micromachining entails the fabrication techniques used to produce three-dimensional structures and mechanical parts with dimensions in the micrometer range. It can be combined with microelectronics processing to produce completely integrated microelectromechanical systems (MEMS) devices. Some of these micro-engineered structures, which are currently used mainly in the automotive and biomedical markets, include acceleration sensors for automobile airbags, disposable blood pressure transducers, and ink jet nozzles. Micromachining fabrication techniques evolved from the well-developed IC technology [16].

Since its inception in the late 1950s, ICs have increased in complexity while decreasing in dimension. Moreover, ICs have afforded the creation of low cost, high

performance, batch processed devices. Microstructures generally are smaller, more reliable, cheaper, and faster than the macroscopic structures [56]. Therefore, when concern was given for the advancement of conventional transducers, these same IC microfabrication techniques were also adopted into transducer technology. The first and probably still most successful microsensor is the silicon pressure sensor [56].

There are a number of innovative fabrication techniques that have been developed specifically for microelectromechanical structures including silicon micromachining, excimer laser micromachining, and LIGA. All of these techniques can implement IC processes such as chemical etching, ion implantation, diffusion, photolithography, and thin film deposition [57].

Silicon micromachining can be divided into two categories: bulk and surface micromachining. Bulk micromachining involves shaping the silicon substrate using chemical etchants to form a set of basic microstructures. Surface micromachining entails depositing and etching thin films on the substrate to produce more complex microstructures [58]. Bulk micromachining is a subtractive process, while surface micromachining is additive. Bulk micromachining is one of the most developed processes of any of the other micromachining technologies. It was used in fabricating the acoustic sensor presented in this thesis.

There are three basic techniques that are utilized in bulk micromachining. These processes include: deposition or growth of thin films which serve as masks, patterning the substrate by wet chemical etchants, and patterning material by dry etching [59]. The fabrication process may also include such techniques as doping the silicon to alter its properties and bonding micromachined silicon wafers to obtain certain dimensions.

Indeed, wet chemical etching is recognized as the key factor in the bulk micromachining process.

Wet chemical etchants are divided into two groups: isotropic etchants and anisotropic etchants. The first etches the substrate at the same rate in all directions. The latter, however, attacks the substrate at different rates in different directions producing microstructures with critical dimensions that are precisely determined by the crystal structure of the silicon wafer [58]. Because of its very unique etching capabilities, anisotropic etching is an important technology for micromachining miniature three-dimensional structures such as sensors and actuators.

Introduced as a preferential directional etchant in the late 1960s and early 1970s, anisotropic etching allows structures to be fabricated in a highly controllable and reproducible manner [60]. Anisotropic etchants were initially used to etch V-grooves on <100> silicon or U-grooves on <110> silicon for MOS transistor fabrication [61]. Once its unique capabilities were explored and developed, anisotropic etchants were used to create other various geometries and shapes. They can be combined with etch masks and etch stop techniques to "sculpt" three-dimensional structures that might otherwise be impossible. Therefore, anisotropic etching is vital for the micromachining of miniature structures.

4.3. Emulsion Plating

The masks used in transferring the desired pattern for the acoustic sensor onto the silicon substrate were made by emulsion plating. Two masks were required to fabricate the sensor and are shown in Figure 21. Mask #1 defined the square opening through

which the backside of the silicon wafer was anisotropically etched. Mask #2 defined the metal electrode pattern on the front of the wafer. The metallization step used a lift-off procedure, therefore a dark-field mask was required.

In emulsion plating, an image is created, reduced in size, and then transferred to an emulsion coated glass plate. CorelDRAW® software was used to create the images. The images were scaled down for 20x reduction. The patterns for each mask were printed on two transparencies. The transparencies were used to transfer the created image onto the glass plate. Two overlapping and properly aligned transparencies ensured that light only passed through the image in the clear regions of the transparencies.

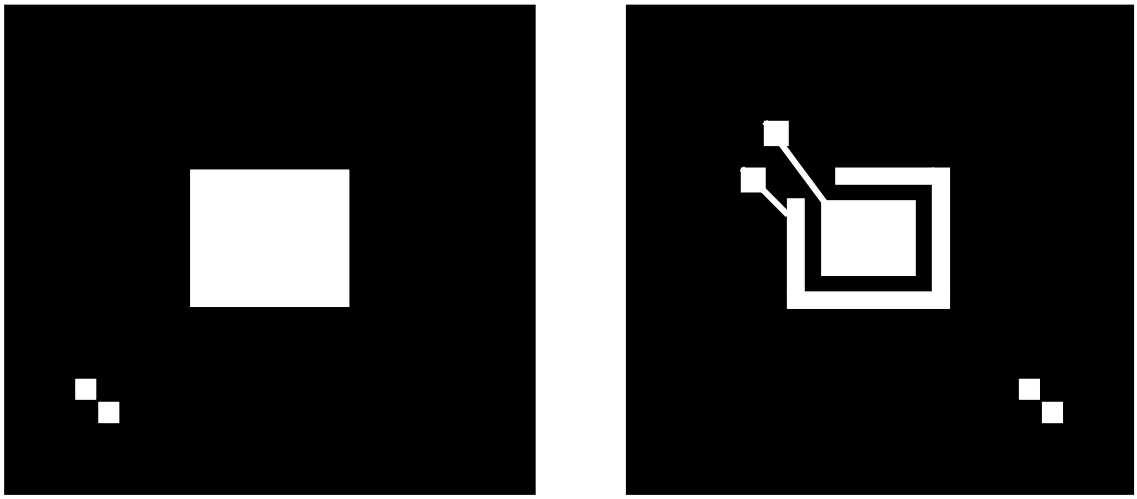

Mask #1 Mask #2

Figure 21. Mask layout.

The process used in transferring the image to the masks is analogous to the process used in taking pictures with a conventional camera and film. Figure 22 shows the set-up used. The procedure was performed in a dark room and the transparencies were placed in

the center of the camera screen. The camera "photographs" the image on the transparency onto the emulsion plate. Once the "picture" is taken, the exposed plates are placed in a protective mask box. The masks were then transported to the lab (which had special dark room lights) where they were developed using the appropriate chemicals.

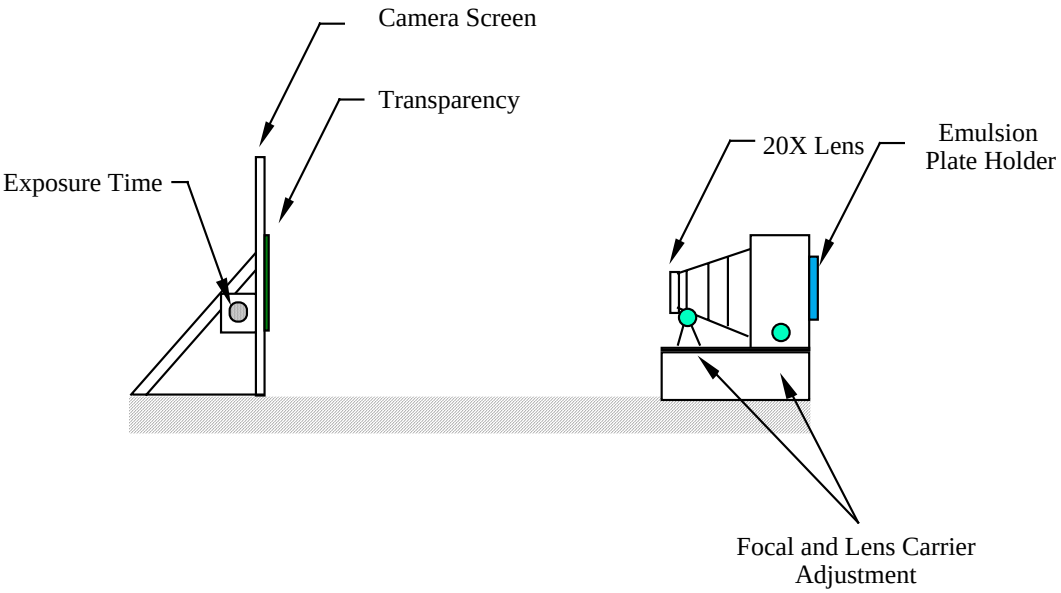

Figure 22. Camera set-up for making masks.

4.4. Process Sequence

Processing of the sensor was performed in the Microelectronics Research Center. The fabrication steps are illustrated in Figure 23. First, a two-inch n-type (100) silicon wafer was cleaned using an RCA cleaning process. It was then doped with a high concentration of boron atoms. The doped area acted as an etch stop in a later step. A constant source diffusion process was used to obtain the p^+-silicon layer with a depth of 3.5 μm (Figure 23a). It was performed at 1150°C for two hours. After the diffusion step, the wafer was dipped in a buffered oxide etch to remove any silicon dioxide grown during the diffusion.

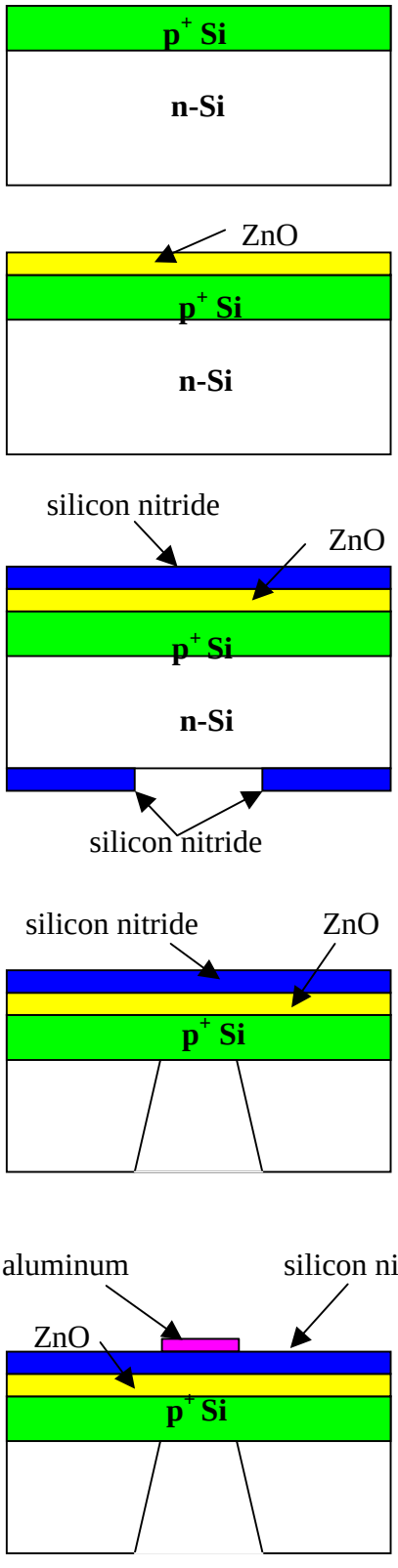

Figure 23. Schematic of fabrication process.

The ZnO piezoelectric layer was then deposited on the front side of the wafer (Figure 23b). The deposition of high quality ZnO is an art. In this case, the ZnO layer was deposited and characterized by the Georgia Tech Microacoustics research group, using an RF-magnetron sputterer dedicated to ZnO depositions. Such a layer yields an effective piezoelectric coupling of 0.23. The ZnO layer was 0.8 μm thick. Masking layers of silicon nitride were deposited over the ZnO, as well as on the back of the wafer, in a plasma enhanced chemical vapor deposition (PECVD) chamber. A 5-hour post-deposition anneal in a rapid thermal processing (RTP) reactor was performed at 325°C to relax some of the stress in the ZnO [62, 63].

In order to micromachine the thin membrane into the silicon, two-sided processing was employed. This introduced numerous processing complications. First, HMDS primer was applied to the nitride on the backside of the wafer. Shipley 1813 photoresist was then spun onto the wafer. The photoresist was soft-baked for 30 minutes at 95°C. It was then patterned using a mask aligner and mask #1. The pattern was developed using Shipley Microposit 319 Developer. This pattern was used to define the diaphragm area. The wafer was then hardbaked at 120°C for 30 minutes. The exposed nitride (on the backside) was dry etched in a reactive ion etcher (Figure 23c). The square openings etched into the nitride left areas of the underlying silicon exposed. The wafer was then immersed in acetone to remove the photoresist. Next, the exposed silicon was back-etched in an aqueous solution of 29% (by weight) potassium hydroxide (KOH). KOH is an anisotropic etchant.

ZnO is highly reactive and can be etched in varying degrees by many common bases, acids, and even photoresist developer [64]. Therefore, many problems were encountered

in forming the membrane without attacking the ZnO. The nitride passivation layer over the ZnO provided only limited protection, as any pinholes in the nitride facilitated exposure of the ZnO to the KOH, and therefore, fast etching of the ZnO. This problem was eventually resolved using a set-up developed by Brugger et al. for single-sided wet etching of microelectromechanical systems (MEMS) devices [65].

This technique uses an elastomer, polydimethylsiloxane (PDMS), as a sealing ring. It has been reported that this material will self-adhere and bond to very clean, hard surfaces without the need for mechanical pressure. Therefore, if such a ring is formed to adhere to the back of the wafer, a small etching "pit" can be realized on the back surface only. Figure 24 shows the incorporation of the ring in the etching set-up, the PDMS ring was applied to the wafer, forming a bond between the wafer and ring surface. Using this approach, a small amount of the etchant can be placed on the wafer surface and will not leak. An infrared (IR) lamp can be used to heat the etchant during the process. The front side of the wafer, where the ZnO was located, was totally isolated from the KOH. The PDMS ring was fabricated using Dow Sylgard 184 elastomer. The Sylard curing agent and silicone elastomer were mixed using a ratio of 1 part curing agent to 10 parts base elastomer. The mixture was then poured into a mold that was custom designed to fit the 2-inch wafers used.

The PDMS ring was cured in an oven for one hour at 100°C and then removed from the mold. It was then applied to the wafer surface. KOH was applied to the backside of the wafer using a pipette and the wafer was back-etched. The boron-doped silicon, as well as the slow etching (111) planes, were used as an etch stop and to delineate the

sensor membrane (Figure 23d). The membrane was very thin at that point.(~4.4 μm), and extreme care had to be used during the subsequent processing steps.

AZ 5214 photoresist was spun onto the top surface of the wafer. It was pre-baked on a hot plate for a minute at 100°C. It was patterned using mask #2. This pattern was aligned with the membrane using an IR bulb with the mask aligner to "see" the dimensions on the back side. The photoresist was then developed in Shipley Microposit 354 developer. A 200 Å layer of chrome and 1500 Å of aluminum were then deposited on the front side of the wafer in an electron beam evaporator (Figure 23e). A lift-off procedure was then used to produce the electrode pattern of Figure 18. In the lift-off procedure, metal was deposited over a photoresist mask on a sample. The sample was then placed in acetone. The photoresist, as well as any metal deposited over it, was removed in acetone. Therefore, metal remained on the substrate only in the open areas of the photoresist mask. The electrode pattern was transferred to the metal and a final anneal in the RTP was performed to ensure good electrical contact.

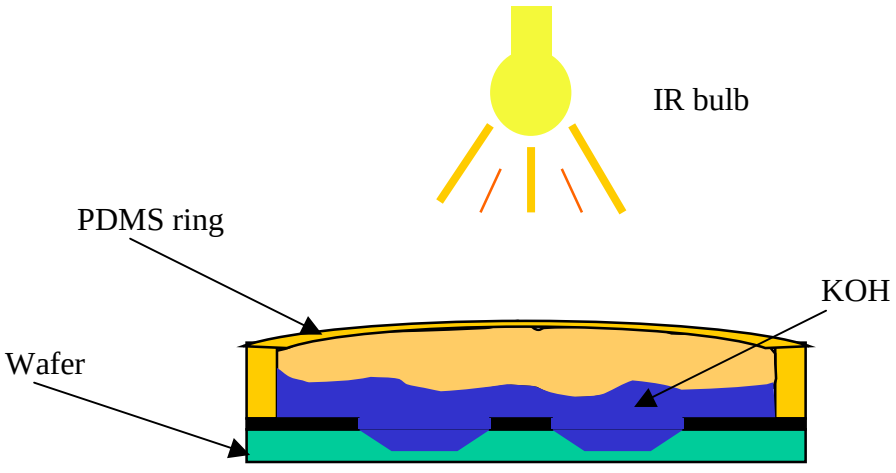

Figure 24. Etching set-up with PDMS ring.

CHAPTER FIVE

SENSOR RESPONSE AND MEASUREMENTS

The acoustic sensor presented in this thesis consists of a silicon diaphragm. To predict the performance of the sensor, mechanical theory of thin plates was considered. This theory provided the foundation necessary to describe the behavior of the diaphragm when subjected to a mechanical load. The mechanics equations derived were used, along with the piezoelectric equations of Section 3.1 and the equations derived for the equivalent electric circuit described in Section 3.4, to predict the sensitivity of the sensor. The approach used in determining this response was based on that of Kim [66].

The acoustic sensor was tested, and its sensitivity was determined experimentally. The test set-up used to measure this response is described in this chapter. Moreover, the experimental results are presented and compared to the theoretical sensitivity calculations.

5.1. Theory of Thin Plates

The sensor uses a diaphragm as its sensing element. A diaphragm is a thin plate. Plates are structures with thicknesses that are much smaller than their other dimensions [67]. For isotropic, homogeneous thin plates with small deflections w (with respect to their thickness h), there are usually three fundamental assumptions that are made [67, 68]:

1. The middle plane of the plate remains neutral during bending and is not strained.

2. Points on a plane that is normal to the middle plane remain on that normal-to-the-middle plane and remain normal to the midplane after bending.
3. Stresses that are normal to the middle plane are small in comparison to the other stress components and can be disregarded.

These assumptions are known as the Kirchoff Hypotheses [67]. The deflection w is a function of the two coordinates of the plate's plane. Using the above assumptions, all of the stress components can be derived from w [68]. The expression for the deflection as a function of the plane's coordinates has to satisfy a linear differential equation. This equation, along with the boundary condition(s) of the plate, defines w entirely [68]. Its solution can be used in calculating the stress at any point on the plate.

The sensor diaphragm has a square shape with all edges clamped, as shown in Figure 25. It has edge length a and thickness h. Its middle surface (midplane) is the xy plane. When a uniform lateral load q is applied to the plate, as shown in Figure 26, deformation occurs and the midplane experiences deflection w in the z-direction. As depicted, the stress varies in sign along the x-axis and is of opposite sign in areas above and beneath the midplane.

The boundary conditions for a square plate with all edges clamped or built-in is [67,68]

$$w = 0 \quad \frac{\partial w}{\partial x} = 0 \ \ (x = \pm a/2) \tag{23}$$

$$w = 0 \quad \frac{\partial w}{\partial y} = 0 \ \ (y = \pm a/2) \tag{24}$$

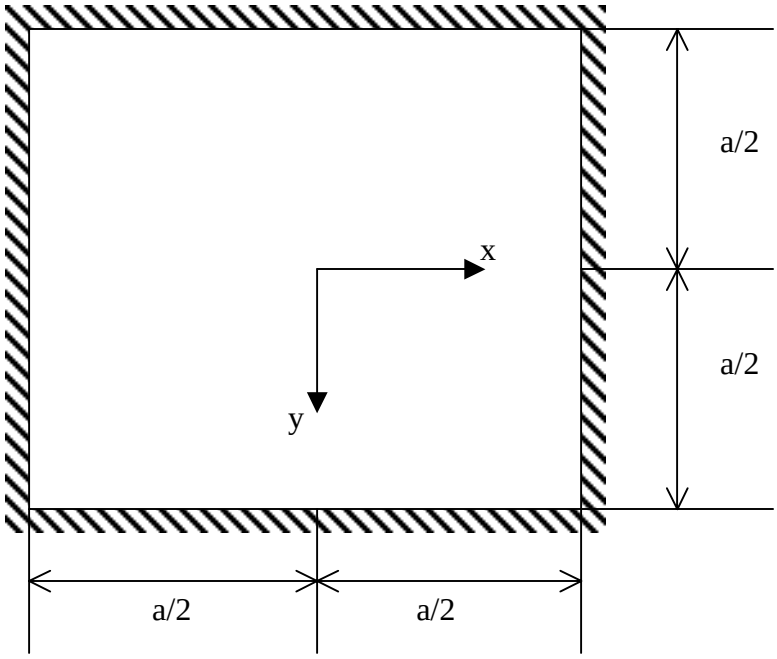

Figure 25. Sensor diaphragm.

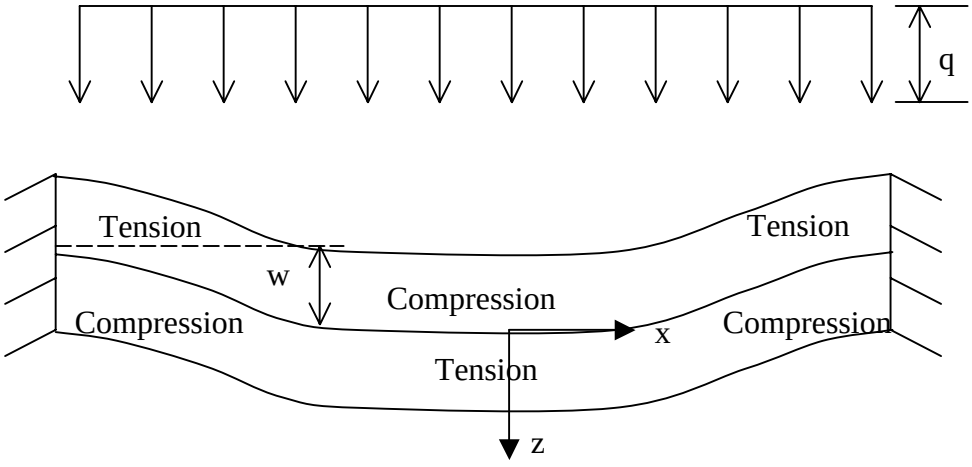

Figure 26. Side view of deflected diaphragm.

5.2. Theoretical Sensitivity Calculations

Equation (16) expresses the relation between the polarization of the piezoelectric plate and its stress. Expressed in its extended form for ZnO (hexagonal crystal symmetry), Equation (16) can be written as:

$$\begin{bmatrix} P_x \\ P_y \\ P_z \end{bmatrix} = \left| \begin{matrix} 0 & 0 & 0 & 0 & d_{15} & 0 \\ 0 & 0 & 0 & d_{15} & 0 & 0 \\ d_{31} & d_{31} & d_{33} & 0 & 0 & 0 \end{matrix} \right| \begin{bmatrix} \sigma_x \\ \sigma_y \\ \sigma_z \\ \tau_{yz} \\ \tau_{zx} \\ \tau_{xy} \end{bmatrix} \tag{25}$$

where d_{15} = -8.3x10^{-12} C/N, d_{31} = -5x10^{-12} C/N, and d_{33} = 12.4x10^{-12} C/N [69]. P_x, P_y, and P_z are the x, y, and z components, respectively, of the polarization. The σ's and τ's are the respective normal and shear stresses in the designated direction(s). Because the electrodes are located perpendicular to the z-axis, the charge induced on the electrodes is primarily due to P_z. The charges due to P_x and P_y are negligible. Therefore, in our calculations, the values of the shear stresses are not needed. Also, based on the theory of thin plates with small deflections, σ_z can be neglected because it is perpendicular to the plate [67, 68]. For a square membrane with all edges clamped, σ_x and σ_y are symmetrical with respect to the x and y axes. Therefore, $\sigma_x(x,y) = \sigma_y(y,x)$ [66, 68]. The resulting charge on the electrodes is given by [54]

$$P_z = \sigma_x d_{31} + \sigma_y d_{31} = d_{31}(\sigma_x + \sigma_y) \tag{26}$$

As shown in Section 3.1., the induced charge Q_s is determined from $\boldsymbol{P}$ and is proportional to the applied mechanical pressure. Multiplying the average P_z by the area will equal the induced charge on that area. To derive the average P_z, the average stress in the membrane must first be determined.

The equation for the deflection w of a square plate with all edges clamped is derived by starting with the equation for deflection for a simply supported plate [66-68]

$$w = \frac{4qa^4}{\pi^5 D} \sum_{m=1,3,5...}^{\infty} \frac{1}{m^5} \left(1 - \frac{\alpha_m \tanh \alpha_m + 2}{2 \cosh \alpha_m} \cosh \frac{m\pi y}{a} + \frac{1}{2 \cosh \alpha_m} \frac{m\pi y}{a} \sinh \frac{m\pi y}{a} \right) \sin \frac{m\pi x}{a} \tag{27}$$

where

$$D = \frac{Eh^3}{12(1-\nu^2)} \tag{28}$$

In Equations (27) and (28), q is the load applied to the plate, a is the length of the side of the membrane, D is the flexural rigidity, m is an odd integer, $\alpha_m = \pi m/2$, E is the modulus of elasticity, and Poisson's ratio is ν. The solution of Equation (27) is superimposed with the solution of the equation for a deflected plate that is subjected to uniformly distributed moments along its edges [66, 67]. This derivation is detailed in [66] and [68] and yields the equation for the deflection of a square diaphragm with all edges clamped

$$\begin{aligned} w(x,y) = \sum_{m=1,3,5....}^{\infty} \Bigg[& \frac{4qa^4}{\pi^5 D} \frac{(-1)^{(m-1)/2}}{m^5} \cos \frac{m\pi x}{a} \Bigg[1 - \frac{\frac{m\pi}{2} \tanh \frac{m\pi}{2} + 2}{2 \cosh \frac{m\pi}{2}} \cosh \frac{m\pi y}{a} \\ & + \frac{1}{2 \cosh \frac{m\pi}{2}} \frac{m\pi y}{a} \sinh \frac{m\pi y}{a} \Bigg] - \frac{a^2}{2\pi^2 D} \frac{E_m (-1)^{(m-1)/2}}{m^2 \cosh \frac{m}{2}} \cos \frac{m\pi x}{a\pi} \Bigg[\frac{m\pi y}{a} \sinh \frac{m\pi y}{a} \\ & - \frac{m\pi}{2} \tanh \frac{m\pi}{2} \cosh \frac{m\pi y}{a} \Bigg] - \frac{a^2}{2\pi^2 D} \frac{E_m (-1)^{(m-1)/2}}{m^2 \cosh \frac{m}{2}} \cos \frac{m\pi y}{a\pi} \Bigg[\frac{m\pi x}{a} \sinh \frac{m\pi x}{a} \\ & - \frac{m\pi}{2} \tanh \frac{m\pi}{2} \cosh \frac{m\pi x}{a} \Bigg] \Bigg] \end{aligned} \tag{29}$$

where E_m is a constant that is computed by the method of successive approximations as shown in [68]. It can be expressed as $E_m = e_m K$, where $K = -4qa^2/\pi^3$ and $e_1 = 0.3721$, $e_3 = -0.0380$, $e_5 = -0.0177$, $e_7 = -0.0085\ldots$ Thus, $w(x,y)$ is given by [66]

$$w(x,y) = \frac{2qa^4}{\pi^5 D}\sum_{m=1,3,5....}^{\infty}\frac{(-1)^{(m-1)/2}}{m^2\cosh\frac{m}{2}}\left[\cos\frac{m\pi x}{a\pi}\left\{\frac{2}{m^3}\cosh\frac{m\pi}{2}-\left[\left(1/m^3+e_m\right)\frac{m\pi}{2}\tanh\frac{m\pi}{2}\right.\right.\right.$$
$$\left.\left.\left.+\frac{2}{m^3}\right]\cosh\frac{m\pi y}{a}+\left(1/m^3+e_m\right)\frac{m\pi y}{a}\sinh\frac{m\pi y}{a}\right\}+e_m\cos\frac{m\pi y}{a}\left[\frac{m\pi x}{a}\sinh\frac{m\pi x}{a}\right.\right. \quad (30)$$
$$\left.\left.-\frac{m\pi}{2}\tanh\frac{m\pi}{2}\cosh\frac{m\pi x}{a}\right]\right]$$

The normal stresses are given as [66, 67]

$$\sigma_x = \frac{-Ez}{1-\nu^2}\left[\frac{\partial^2 w}{\partial x^2}+\nu\frac{\partial^2 w}{\partial y^2}\right] \quad (31)$$

$$\sigma_y = \frac{-Ez}{1-\nu^2}\left[\frac{\partial^2 w}{\partial y^2}+\nu\frac{\partial^2 w}{\partial x^2}\right] \quad (32)$$

$$\sigma_z = 0 \quad (33)$$

Equations (31) and (32) demonstrate that the stresses disappear at the midplane and change linearly over the thickness of the diaphragm [67]. The bending moments created by these stresses are given as

$$\begin{Bmatrix} M_x \\ M_y \end{Bmatrix} = \int_{-h/2}^{h/2}\begin{Bmatrix} \sigma_x \\ \sigma_y \end{Bmatrix} z\,dz \quad (34)$$

$$M_x = -D\left(\frac{\partial^2 w}{\partial x^2}+\nu\frac{\partial^2 w}{\partial y^2}\right) \quad (35)$$

$$M_y = -D\left(\frac{\partial^2 w}{\partial y^2}+\nu\frac{\partial^2 w}{\partial x^2}\right) \quad (36)$$

where M_x and M_y are the x- and y-components of the bending moments, respectively. Thus, the stress can also be expressed as [67]

$$\sigma_x = \frac{12M_x z}{h^3} \tag{37}$$

$$\sigma_y = \frac{12M_y z}{h^3} \tag{38}$$

The largest stresses are located on the surface of the plates (at z = ±h/2). Also, the largest deflection w_{max} is located at the center of the plate, and the largest bending moments M_{max} are found at the center of the fixed edges [67]. They are given by

$$w_{\max} = 0.00126\frac{qa^4}{D} \qquad (x = 0, y = 0) \tag{39}$$

$$M_{\max} = 0.0513qa^2 \qquad \begin{pmatrix} x = \pm a/2, y = 0 \\ x = 0, y = \pm a/2 \end{pmatrix} \tag{40}$$

Because of the symmetry of σ_x and σ_y, the average of each of these stress components is equivalent for the square membrane. Therefore, this derivation will focus on σ_y only. Substituting (30) into (32) yields [66]

$$\sigma_y = \frac{24qza^2}{\pi^3 h^3}\sum_{m=1,3,5...}^{\infty}\frac{(-1)^{(m-1)/2}}{\cosh\frac{m\pi}{2}}\left(\cos\frac{m\pi x}{a}\left\{2\frac{v}{m^3}\cosh\frac{m\pi}{2} - \left(\left(\frac{1}{m^3}+e_m\right)\frac{m\pi}{2}\tanh\frac{m\pi}{2}(v-1)\right.\right.\right.$$

$$\left.\left.+2\frac{v}{m^3}+2e_m\right)\cosh\frac{m\pi y}{a} + \left(\frac{1}{m^3}+e_m\right)(v-1)\frac{m\pi y}{a}\sinh\frac{m\pi y}{a}\right\}$$

$$\left.-e_m\cos\frac{m\pi y}{a}\left\{\left(2v+(1-v)\frac{m\pi}{2}\tanh\frac{m\pi}{2}\right)\cosh\frac{m\pi x}{a}+(v-1)\frac{m\pi x}{a}\sinh\frac{m\pi x}{a}\right\}\right) \tag{41}$$

It has been shown that this series converges quickly as *m* increases [66]. Thus, Kim determined that using only the first term of the series in (41) yields an approximation of (41) with less than 10% error. Using ν = 0.3 for Poisson's ratio, this approximation is given by

$$\sigma_y = \frac{24qza^2}{\pi^3 h^3}\left(\cos\frac{\pi x}{a}\left(0.6 + 0.01573\cosh\frac{\pi y}{a} - 0.3828\frac{\pi y}{a}\sinh\frac{\pi y}{a}\right)\right.$$

$$\left. - \cos\frac{\pi y}{a}\left(0.2385\cosh\frac{\pi x}{a} - 0.1038\frac{\pi x}{a}\sinh\frac{\pi x}{a}\right)\right) \qquad (42)$$

The average stress over the area covered by the electrode pattern of Figure 18 can now be calculated. Because of the symmetry of σ_x and σ_y, only one quadrant of the membrane is required for the calculation. Using the dimensions of the electrodes for the acoustic sensor, the average stress $\overline{\sigma_y}'$ is given by:

$$\overline{\sigma_y}' = \frac{1}{(0.1042191a^2 + 0.06693a^2 + 0.0490115a^2)}\left[\int_0^{0.32283a}\int_0^{0.32283a}\sigma_y dydx + \int_0^{0.5a}\int_{0.36614a}^{0.5a}\sigma_y dydx\right.$$

$$\left. + \int_{0.36614a}^{0.5a}\int_0^{0.36614a}\sigma_y dydx\right] \qquad (43)$$

Substituting (42) in (43) gives

$$\overline{\sigma_y}' = \frac{24a^2qz}{\pi^3 h^3}(0.4236) \qquad (44)$$

Equation (44) is dependent on z and thus, $\overline{\sigma_y}'$ must be averaged over the ZnO thickness to obtain the average stress that can be used in calculating the average P_z in the ZnO layer.

Figure 16 shows the cross sectional view of the sensor and shows the various layers of the device. For the membrane, the ZnO thickness h_{ZnO} = 0.8 μm, the length of the side of the square membrane a = 1270 μm, the thickness of the silicon nitride and the electrodes h_s = 0.385 μm, and the total thickness of the membrane (including the silicon) h = 4.685 μm. The average stress $\overline{\sigma_y}$ in the ZnO is [66]

$$\overline{\sigma_y} = \frac{24a^2 q}{\pi^3 h^3}(0.4236)\frac{1}{h_{ZnO}} \int_{-(\frac{h}{2}-h_s)}^{-(\frac{h}{2}-h_s-h_{ZnO})} z dz \qquad (45)$$

Solving (45) gives the average stress in terms of h, h_{ZnO}, h_s, a, and q. Substituting the values for h, h_{ZnO}, h_s, and a results in an average stress of

$$\overline{\sigma_y} = -8005q \qquad (46)$$

Now the average polarization $\overline{P_z}$ per unit area can be found by substituting Equation (46) into Equation (26) and using $\overline{\sigma_y} = \overline{\sigma_x}$

$$\overline{P_z} = d_{31}(\overline{\sigma}_x + \overline{\sigma}_y) = 2d_{31}\overline{\sigma_y}$$

=2 (-5 x 10^{-12} C/N) (-8005q) for q in Pa (=N/m^2=10μbar)

=8.005 x 10^{-13} q (C/cm^2) for q in μbar

For a given area on the membrane, the induced charge Q_S is $\overline{P_z}A$, where A is the area. Substituting this for Q_S in Equation (21) yields

$$V_o = \frac{-Q_s e^{jwt} C_N}{C_{fb}(C_s + C_N)} = \frac{-\overline{P_z} A C_N}{C_{fb}(C_s + C_N)} = \frac{-8.005\times10^{-13} qAC_N}{C_{fb}(C_S + C_N)} \qquad (47)$$

where q varies sinusoidally ($q \sim q_o e^{j\omega t}$). The values for the capacitances in Equation (47) are C_N = 207.67 pF, C_{fb} = 11 pF , and C_S = 65.48 pF. Also the area A of the electrodes over the ZnO is 6.724x10^{5}μm^2. Substituting these values into Equation (47) gives

$$V_o = \frac{-8.005\times10^{-13} qAC_N}{C_{fb}(C_S + C_N)} = \frac{-8.005\times10^{-13}(C/cm^2)q(6.724\times10^{-3} cm^2)(207.67\,pF)}{11pF(65.48\,pF + 207.67\,pF)}$$

$$= -372q \ \mu V \quad \text{for q in } \mu\text{bar} \qquad (48)$$

From (48), the amplified theoretical sensitivity of the acoustic sensor is determined to be

$$\frac{V_o}{q} = -372\ \mu\text{V/}\mu\text{bar} \tag{49}$$

Microphones are usually operated at frequencies where their response is known to be flat and does not oscillate. Thus, their frequency bandwidth is limited by the diaphragm's fundamental resonant frequency. Therefore, the fundamental resonant frequency was calculated for an isotropic, homogenous square plate with all edges built-in. The plate was assumed to be a heavily doped silicon membrane with a thickness of h = 4.685 μm. The equation for the fundamental mechanical resonant frequency f_0 is [70]

$$f_0 = \frac{1.654h}{a^2}\left[\frac{E}{(1-\nu^2)d}\right]^{1/2} \tag{50}$$

where a is1270 μm, E is 125 GPa (for p^{++} Si), ν = 0.27, and the density d is 2.33 g/cm^3. Therefore, the fundamental resonant frequency of the silicon diaphragm was determined to be 36.5 kHz.

5.3. Experimental Results

After the sensor was designed and fabricated, it was tested to measure its output response to an applied pressure. The test set-up used to measure the sensor response is presented below.

5.3.1. Test Set-up

Figure 27 shows the test set-up for the silicon microphone. It consisted of the microphone under test (MUT), the wafer stage, a probe station, a loudspeaker, a sine wave generator, and a Hewlett Packard (HP) 4395A network/spectrum analyzer. The set-up was arranged so that the MUTs could be tested on the wafer without having to dice the

wafer. The wafer stage had a hole in the center that functioned as an inlet for sound pressure to the backside of the MUT diaphragm. A loud speaker (2" directly radiated tweeter) driven by a sine wave generator provided the sinusoidal pressure (sound) that propagated through the ¾" plastic tubing to the stage inlet hole. The MUT was probed by probe needles that were connected to the amplifier. Because of the high output impedance and the low output signal of the MUT, the amplifier was needed as an interface between the MUT and the measuring equipment. The amplifier was connected to an HP 4395A network/spectrum analyzer, where the MUT output signal was measured and recorded. The amplifier used was a low noise charge sensitive amplifier (DN620) by ThermOptics. A Brüel and Kjaer 4135 condenser microphone was used as a reference microphone. The sensitivity of the MUT was obtained by dividing the MUT output response by that of the reference microphone. All of the measurements were performed in the screening room in MIRC 162 to help eliminate electromagnetic interference.

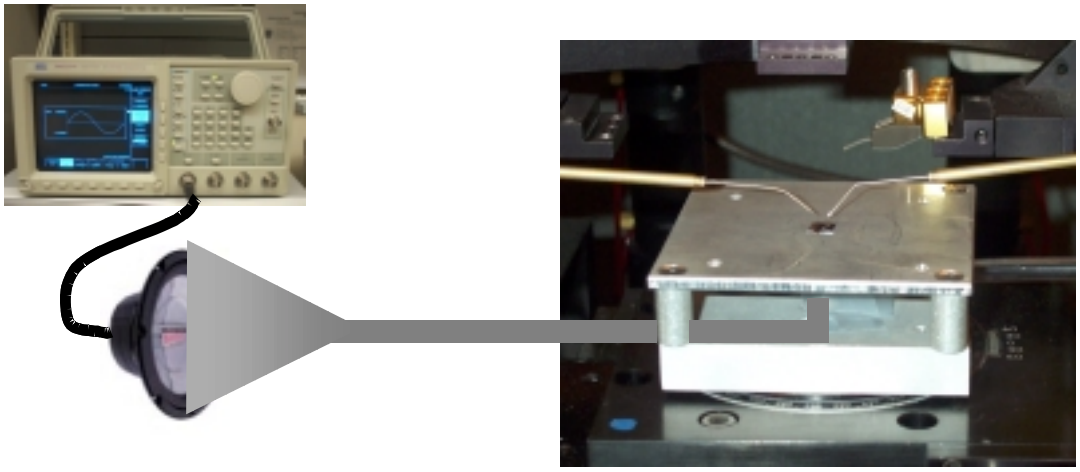

Figure 27. Testing set-up.

5.3.2. Results

Plotted in Figure 28 are the amplified sensitivity values measured from the acoustic sensor from 100 Hz to 10 kHz. The sensitivity yields the output voltage of the sensor for a given incident pressure. It describes how a sensor responds to a given input signal. Below 1 kHz we see large variations in the output. This may have been caused by equipment or other set-up noise, as this was also the case for the reference microphone. Between 1 and 10 kHz, the sensitivity variation was approximately 8.3 dB, and the typical sensitivity was 195 μV/μbar.

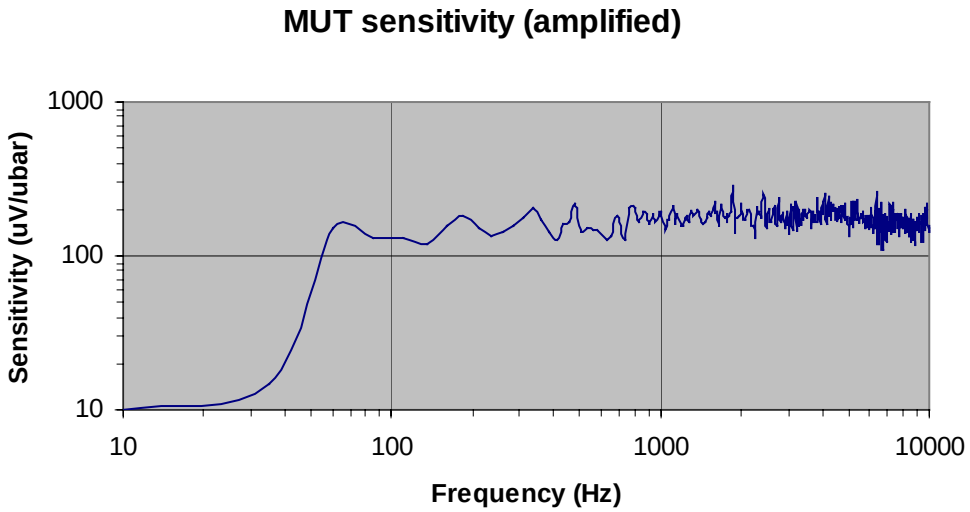

Figure 28. Plot of sensor sensitivity (amplified).

5.4. Comparison

The experimental sensitivity (195 μV/μbar) of the fabricated device is on the same order of magnitude of the theoretically calculated sensitivity of 372 μV/μbar. Discrepancies between the measured and theoretical values can be attributed to the influence of the testing environment on the sensor output. Noise due to the amplifier,

cables, as well as the measurement equipment may affect the response measured. All of the plots obtained had non-uniform graphs. This could be due to acoustic noise and interference in the room where the measurements were performed, as it was not anechoic. The reference microphone also exhibited a non-uniform response. Also there may be discrepancies in the idealized values used in the analytical equations used to calculate the sensitivity. For example, though the dimensions of the device are pre-determined and somewhat controlled, some dimensions, such as layer thickness, are ultimately determined during processing. Other processing issues result in factors not accounted for by the equations, such as stress in the ZnO layer. It is known that such stress not only affects the acoustic response to an external loading, but can cause buckling in the membrane as well [62].

5.5. Summary

In this chapter the theory of thin plates was presented and used to derive the equations that describe the response of the acoustic sensor to a mechanical load. The microphone membrane can be modeled mechanically as a thin square plate with all edges clamped. This membrane is deflected when a load is applied. Based on the equation describing this deflection and the boundary conditions that exist because of the structure of the plate, an equation for the stress in the plate was determined. This equation for stress was then used to obtain the polarization induced in the piezoelectric layer due to the mechanical load (pressure). The charge generated on the sensor surface could then be derived from the polarization. The charge generated was used to determine the output voltage of the microphone due to pressure. Thus, the sensitivity (V_o/pressure) was determined theoretically to be -372 μV/μbar.

The microphone was also implemented in an experimental test set-up to determine its measured sensitivity to an applied pressure. It was observed to have a sensitivity of 195 μV/μbar, which was on the same order of magnitude as that of the theoretically determined sensitivity. Discrepancies between the theoretical and experimental values may have been a result of the testing environment, electrical/equipment noise, and differences in the real life device dimensions and the ideal dimension values used in the theoretical calculations.

Chapter 6 describes the application of the microphone as a process sensor for monitoring electrochemical deposition (electroplating). The mechanism of electroplating will be presented, as well as uses of a specific plated metal alloy-nickel-iron. The plating set-up incorporating the sensor will be described, and the results obtained during the

deposition runs will be presented. The predictive model developed relating the sensor output to the plated thickness will be presented as well. Such a model enables real time monitoring of electrodeposition.

CHAPTER 6

MONITORING ELECTROCHEMICAL DEPOSITION USING THE ACOUSTIC SENSOR

As demands in semiconductor manufacturing increase, the need to monitor and control fabrication processes continues to grow. New sensors and systems are required to meet these demands. The key to achieving process control involves identifying crucial processes that warrant monitoring and providing ways to provide it. This thesis addresses the need for new techniques for monitoring the electrochemical deposition (electroplating) process. This critical manufacturing process is used for the deposition of metal films for packaging interconnects, as well as in the creation of magnetic devices.

For a given deposition process, *in-situ* determination of the deposition rate or thickness is desired. Currently quartz crystal microbalance (QCM) technology is the primary means of providing this [71,72]. This technology monitors the shift in the resonant frequency of the quartz to determine the deposition rate. The acoustic sensor described in previous chapters was used to provide *in-situ* monitoring of the progression of metallization during electroplating. This chapter describes the electrochemical deposition process. Prior to the discussion of electroplating, some preliminary experimentation was performed to validate the concept of acoustic velocity variations as a function of molarity. The results of these experiments are discussed in Appendix A. These results verified that acoustic velocity decreases with decreasing molarity, thereby implying that this affect could be used to monitor an electroplating process.

In this chapter, first the mechanism and chemistry of electroplating will be presented, as well as details about the nickel-iron electroplating bath used in the experiments. The implementation of the sensor in the electroplating set-up will also be described. The theory used to validate the sensing approach used is detailed, and the empirical model established for electroplating is reviewed.

6.1. Electroplating Mechanism

Electrochemical deposition is used to deposit various metals on substrates via the reduction of ions in an electroplating solution (electrolyte). An electrolyte is an aqueous solution where ions are present and through which electricity is conducted. Ionic compounds (e.g. NaCl) are normally dissolved by a solvent, which is usually water. It should be noted that like dissolves like; meaning ionic solids are more soluble in polar solvents than in non-polar solvents [73]. Water is a polar liquid. Moreover, the hydrogen atoms of the H_2O molecule have a small partial positive charge and the oxygen atom has a small partial negative charge. This results in a dipole moment [74]. The water dipole is shown in Figure 29.

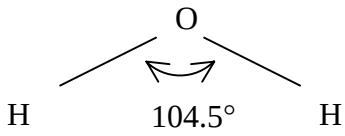

Figure 29. Water dipole.

The dissolution of ionic solids separates the compound into separate positive and negative ions in the solution. In strong electrolyte solutions, the solute is completely ionized. For an ionic compound MA (M is the cation and A is the anion), the dissolution process is shown by the reaction [74]

$$M^{z+}A^{z-} + (m + a)H_2O \rightarrow M^{z+}(mH_2O) + A^{z-}(aH_2O) \quad (51)$$

where z is the number of electrons, and m and a are the number of moles. Therefore, in this process, water molecules break the ion-ion lattice and the ions are free to move apart.

The interaction of the ions with the water molecules hydrates the ions. Electrolyte solutions can also be found from certain molecular compounds as well. No ions are present in this compound until it is dissolved. This discussion, however, will only focus on electrolyte solutions formed from ionic compounds.

For reasons that will become clear in a subsequent section, it is necessary to describe the model of the ions in the solution. The cations and anions interact with the water primarily because of the ion-dipole forces. For cations, the negatively charged end of the water dipole is attached to the cation electrostatically (Figure 30a) [74]. Anions are attached to the positively charged end (Figure 30b). Moreover, water molecules directly interacting with the ions are aligned and make up the primary hydration shell as shown in Figure 31 (location A). This shell of molecules and the ions move together as one entity.

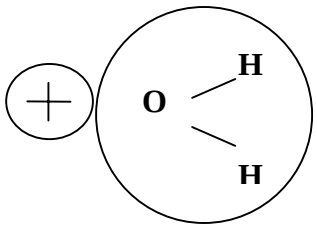

a.

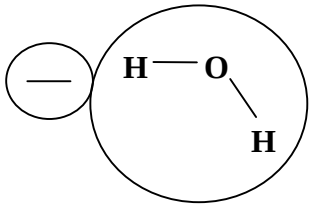

b.

Figure 30. Alignment of ions with water

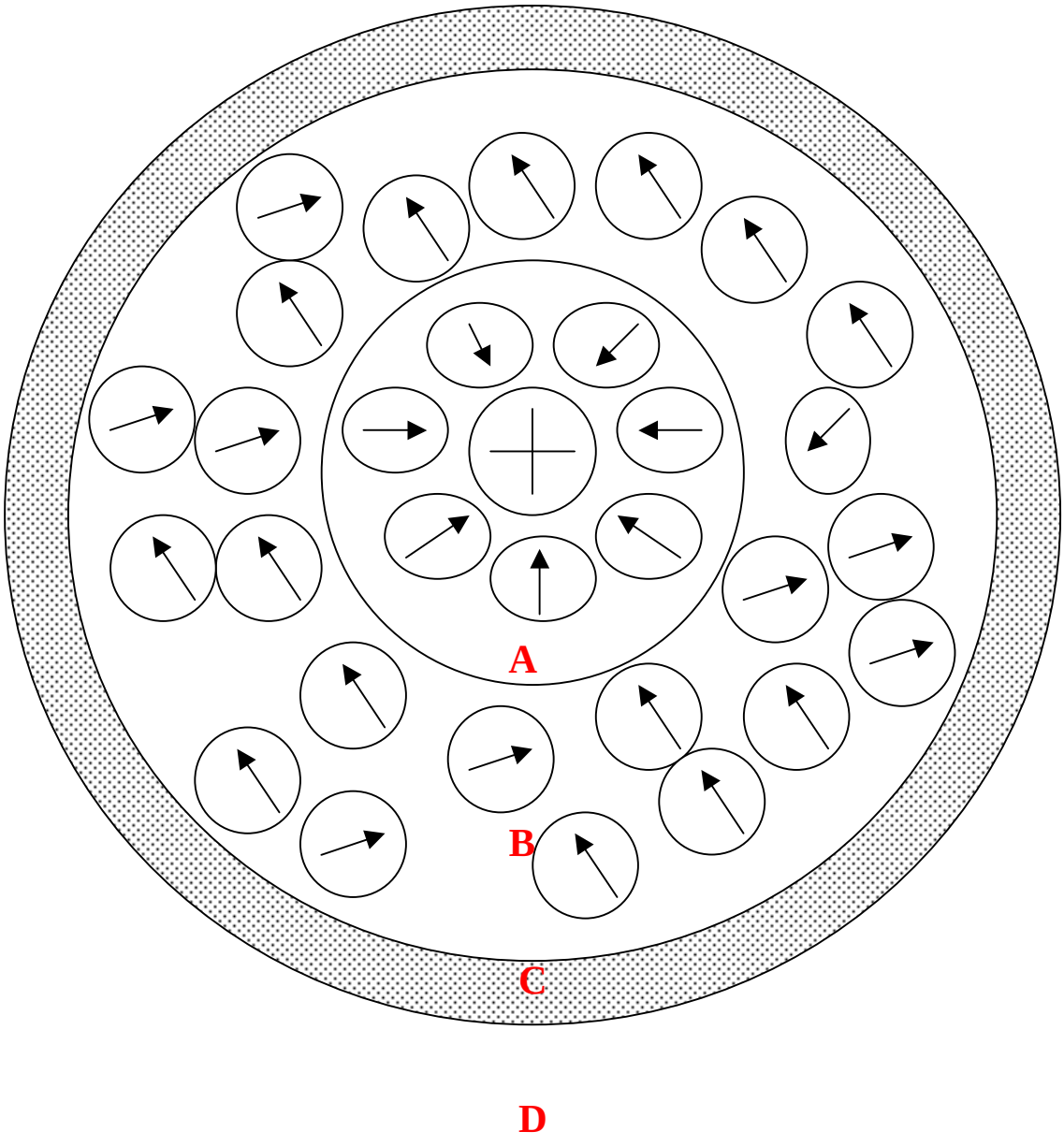

A: Primary Hydration Shell
B: Secondary Hydration Shell
C: Disordered Region
D: Bulk Solvent

Figure 31. Environment of ion in aqueous solution.

The region next to the primary hydration shell is the secondary hydration shell of water molecules. These molecules are not in contact with the ion, but are influenced by the interaction of the electrostatic fields of the ions and their dipoles [75]. These molecules are partially aligned. There is an intermediate disordered region, C, that lies between the partially oriented region B and the bulk solvent, D. The water molecules in the bulk solvent are not affected by the ions.

Metal ions usually have a positive charge (cations). The deposition of a metal onto a substrate requires that the metal gain electrons (becomes reduced). This is represented by [15, 74]

$$M^{z+} \text{ (solution)} + ze \rightarrow M \text{ (lattice)} \qquad (52)$$

If the arrow in (52) was reversed, and the reaction went from right to left, electrons would be released and oxidation would occur.

Electroplating entails two different methods: electrolytic and electroless plating. In electrolysis, the beaker contains an electroplating solution (electrolyte) consisting of ions of the metal to be plated as well as sufficiently negative and positive electrodes as shown in Figure 32. The substrate to be plated is located at the negative electrode (cathode). Power is supplied to the electrodes, causing current to flow through the electrolyte. The current is needed to drive a non-spontaneous reaction—the flow of electrons from the anode to the cathode. Thus, electrons are supplied to the metal ions at the cathode. For example, if copper sulphate ($CuSO_4$) is used as the plating solution in Figure 32, the copper cations (Cu^{2++}) will move towards the cathode, become reduced (gain electrons), and deposit Cu there [13,14]. The sulphate anions (SO_4^{2-}) are attracted to the positively

charged anode and oxidation (electrons released) occurs. The reaction is represented as [13, 14]:

$$CuSO_4 \rightarrow Cu^{2+} + SO_4^{2-}$$

$$\text{at cathode: } Cu^{2+} + 2e^- \rightarrow Cu(s)$$

$$\text{at anode: } SO_4^{2-} \rightarrow SO_4 + 2e^-$$

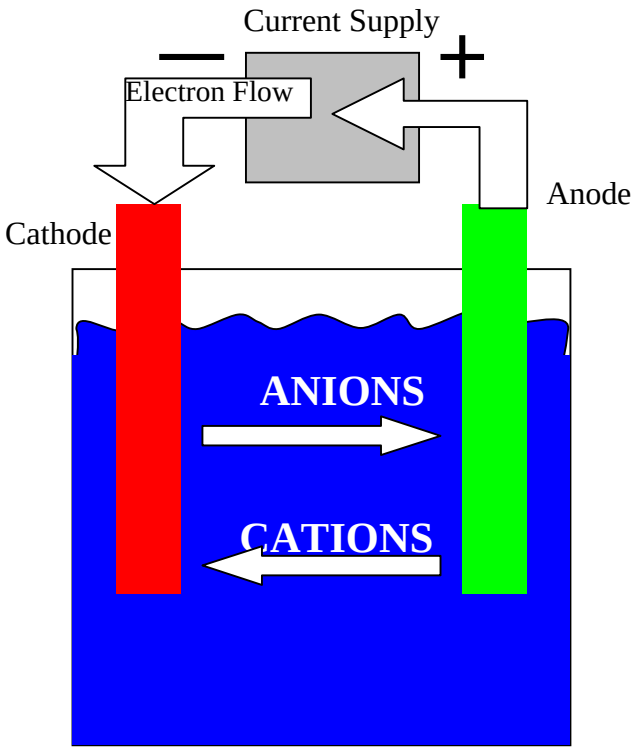

Figure 32. Electrolytic cell.

Usually, a conductive seed layer is deposited on the substrate prior to an electroplating process. Contact is made to the substrate, and it is used as the cathode. The deposition rate of the metal is related to the current density; therefore, a metal with uniform thickness can be obtained by maintaining a uniform current density over the

substrate surface. The current needed for the reaction is determined by multiplying the surface area of the exposed seed layer by the current density associated with the process for the particular metal used.

When considering the deposition of the metal, it is necessary to consider structure properties of the metal lattice. The metal can be thought of as a fixed positively charged lattice with a gas of freely moving electrons [15]. The metallic bond formed during deposition is mainly due to the interactions of the metal ions and free electrons. The deposition process can be described from an atomic standpoint using Figure 33, in which location 1 is the initial state of the hydrated metal ion, M^{z+} (solution). The final state of the ion for deposition is found at location 4. Note that the ion will attach to the metal crystal as an adsorbed ion at a kink site [15]. This is represented as

$$[M(H_2O)_x]^{z+} \text{ (solution)} \rightarrow M^{z+} \text{ (kink)} \qquad (53)$$

Step-edge site ion-transfer or terrace site ion- transfer are the two mechanisms whereby this process will occur. For the step-edge site ion-transfer mechanism, the ion is transferred from the solution to the kink site of a step edge (Figure 33, location 4) or to some other location on the step edge (Figure 33, location 3). For the latter case, the metal ion will move (diffuse) down the step edge until it finds a kink site (location 4).

For the terrace site transfer mechanism, the ion is transferred to a flat region of a terrace site (location 2). This adion is weakly attached to the lattice and seeks to find a position with a lower energy [15]. It diffuses on the surface and eventually arrives at a kink site, its final destination.

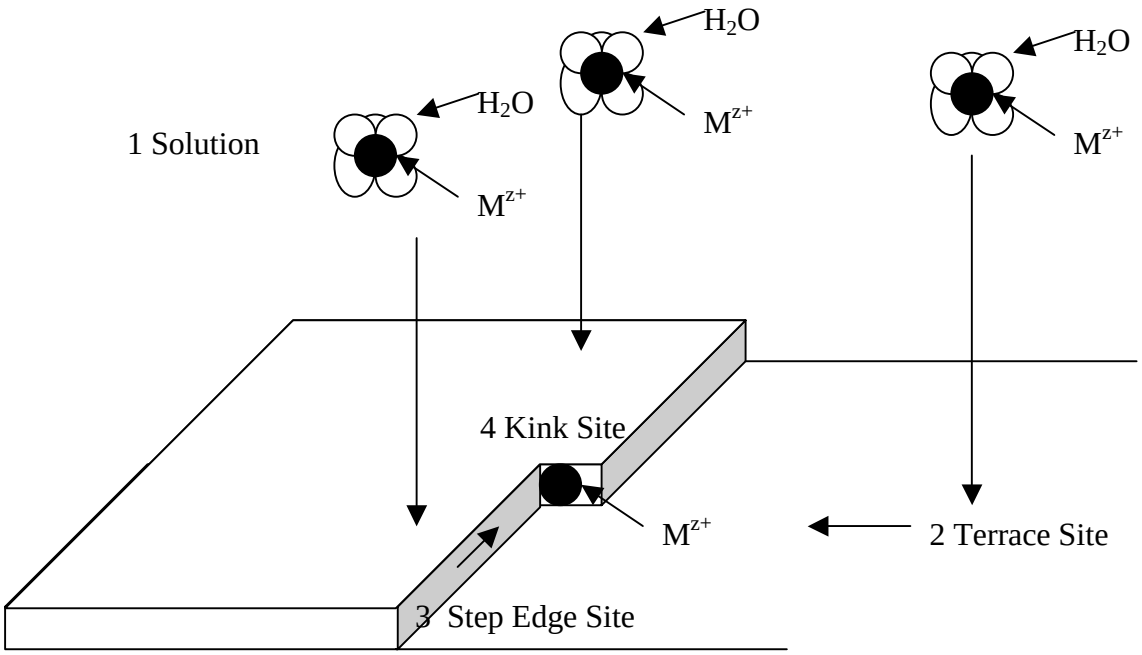

Figure 33. Ion transfer for metal deposition [15].

6.2. Nickel-iron Plating

This thesis focuses on monitoring nickel-iron (Ni-Fe) electroplating baths. Nickel-iron is an alloy (a mixture of two or more metals). Alloy deposition follows the same guidelines and mechanisms as single-metal electroplating. Alloys are desirable since they can provide specific characteristics unobtainable for single metals. Ni-Fe alloys have favorable magnetic properties, such as high permeability, good soft magnetic properties, and low magnetostriction and anisotropy [18, 19, 76]. They also possess good mechanical properties. Ni-Fe alloys have been used for thin-film magnetic heads, enabling magnetic media with greater reading and writing densities. Ni-Fe is also of interest for micromachined magnetic devices, such as actuators and inductors.

Table 3 gives the composition of the Ni-Fe bath used in the experiments performed in this research. The nickel sulfate ($NiSO_4 \bullet 6H_2O$) and nickel chloride ($NiCl_2 \bullet 6\ H_2O$)

Table 3. Composition of Ni-Fe electroplating solution.

Component	Ni (80%) - Fe (20%)
$NiSO_4 \bullet 6H_2O$	200 (g/l)
$NiCl_2 \bullet 6\ H_2O$	5 (g/l)
$FeSO_4 \bullet 7H_2O$	8 (g/l)
H_3BO_3	25 (g/l)
Saccharin	3 (g/l)
pH	2.5 – 3.0
Temperature	25 – 30 (^oC)
Current density	15-30 (mA/cm^2)

each provide Ni^{2+} ions. The ferrous sulfate ($FeSO_4 \bullet 7H_2O$) provides Fe^{2+} ions. The nickel-iron bath is prepared by first weighing the components of the bath as outlined in Table 3. The components are then mixed in a glass beaker, and the beaker is filled with DI water to 1000 ml. A magnetic stirrer is used to stir the bath overnight. In addition to the metal salts, the bath also contains boric acid (H_3BO_3) and saccharin. Boric acid is a buffering agent that is used to stabilize the pH in the cathode film [15]. The saccharin is added to the solution to reduce the residual stress in the metals deposited [19].

6.3. The Propagation of Sound in Fluids

The methodology used to monitor nickel-iron plating involves sensing changes in the plating bath using acoustic waves. For a small volume element of fluid in equilibrium, the fluid surrounding the element exerts an equivalent normal pressure on all of the surfaces of the element [77]. In equilibrium, the molecules in the fluid, however, are not at rest. They move randomly and collide with other molecules. As a sound wave propagates through a fluid, each element of the fluid experiences longitudinal vibrations and is displaced from its equilibrium position in the presence of the wave. This movement dominates the molecules' random movements and is transmitted to the adjacent volume element causing the sound wave to propagate through the fluid. Therefore, the fluid does not move as a whole with the wave, but small elements of the fluid are displaced (in the presence of sound) [78]. The particle displacement is along the direction of the wave, and therefore, it is a longitudinal wave. This is the only wave type that can be sustained in ideal fluids.

If the collision between molecules transmitting the wave increases the local density and pressure of the fluid, then an area of compression has been established. Areas of rarefaction propagate where the region possesses a density and pressure lower than that of equilibrium. The speed of the wave traveling through a fluid is determined by the properties of the medium. More, specifically, the speed is a function of an inertial property (density ρ) and an elastic property (bulk modulus *B*) [78]. Elasticity establishes the restoring force of a fluid element displaced from equilibrium and inertia indicates the response of the displaced element to the restoring forces [78].

The elasticity of a fluid is given by a parameter known as the bulk modulus of elasticity. The bulk modulus is the reciprocal of compressibility. It is a measure of how much a fluid compresses due to a pressure. The bulk modulus yields the ratio of change in pressure to the fractional change in volume [77, 78]. It is given by

$$B = -\frac{\Delta P}{\Delta V / V} \tag{54}$$

where P is the pressure of the fluid and V is the volume. The negative sign enables B to have a positive value since an increase in pressure produces a negative change in the volume.

B can also be given in terms of density. In instances where the mass is constant (ρV product is constant) [79],

$$\rho dV + V d\rho = 0 \tag{55}$$

Therefore,

$$\frac{d\rho}{\rho} = \frac{-dV}{V} \tag{56}$$

and

$$B = dp\frac{\rho}{d\rho} \tag{57}$$

The speed v of the sound wave propagating through a fluid is given by

$$v = \sqrt{\frac{B}{\rho}} = \sqrt{\frac{dp}{d\rho}} \tag{58}$$

Consequently, a speed wave travels without transporting matter but causes pressure or density fluctuations in the medium. The term dp is normally called the excess pressure [77]. From Equation (58) it can be written as

$$dp = v^2 d\rho \tag{59}$$

6.4. Plating Set-Up

During electroplating, it is desirable to determine the metal thickness *in-situ*. Usually, the thickness is calculated from the product of an estimated deposition rate and the electroplating time duration. The exact film thickness can then be measured by post-process equipment such as a profilometer. While this is a viable method of determining the thickness deposited, it will present error if the estimated deposition rate is inaccurate or changes during the process. The acoustic sensor developed in this thesis can alleviate such concerns. This sensor was implemented in a plating set-up to provide *in-situ* monitoring of Ni-Fe depositions (see Figure 34).

The composition and preparation of the plating bath were described in Section 6.2. A polypropylene container with flat sides was used for these experiments. The seed metal layer was deposited on a silicon sample. The seed layer consisted of 300Å Ti and 3000Å Cu, and was deposited using an e-beam evaporator. A small portion of the silicon was masked to enable a profilometer to step across the metal-silicon interface after plating to

determine the metal thickness. The silicon/seed layer was used as the cathode and a pure nickel film was used as the anode. A DC supply that could manipulate both current and voltage was used as the power supply. All of the experiments were performed at room temperature.

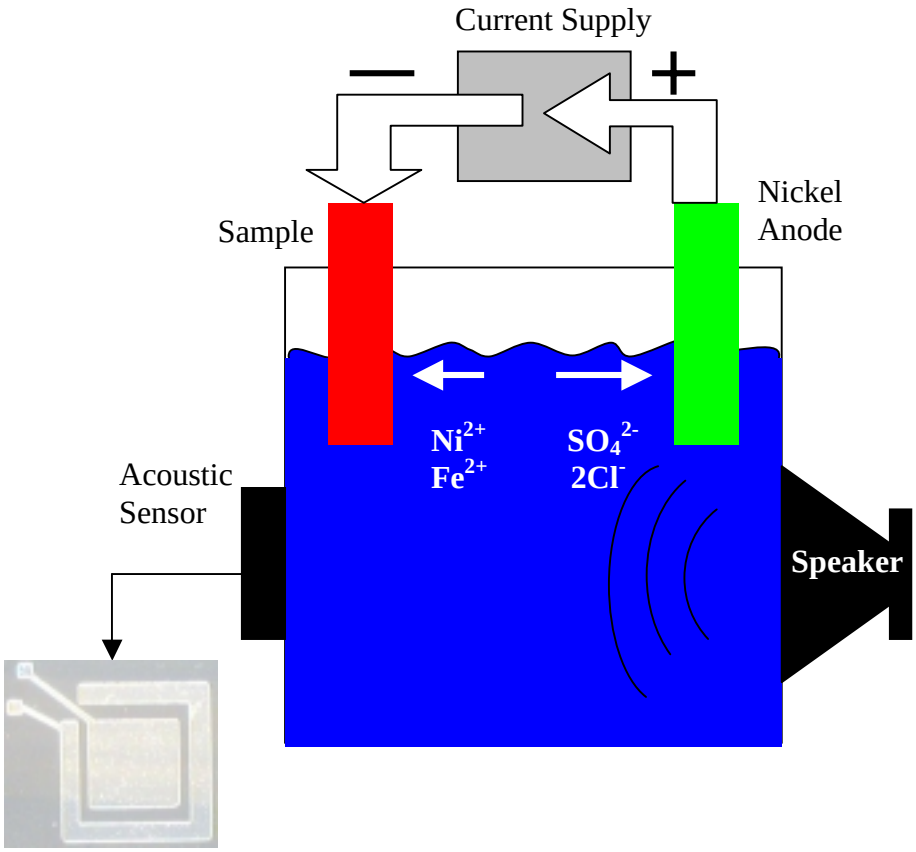

Figure 34. Electroplating monitoring set-up.

The sensor used was separated from the wafer with a diamond saw. It was then bonded onto the center of an IC package. The electrical contacts were wire-bonded to the "legs" of the package. The package was enclosed by a glass slide, and the backside had

an opening that allowed an acoustical port for the sensor. The sensor and loudspeaker were then attached to opposite sides of the electroplating bath container. The "legs" of the sensor package were attached to the amplifier circuit. The output of the circuit was recorded by an HP 4395A spectrum analyzer. The loudspeaker was driven by a sine wave at 9 kHz at 1 V_{rms}. This frequency (9kHz) was chosen because the sensor was known to have a flat response at this frequency.

During plating of Ni-Fe, the nickel and iron ions are attracted to the cathode, while the sulphate and chloride ions are attracted to the anode. The nickel and iron ions are reduced and deposited on the cathode, forming the Ni-Fe alloy layer. At the anode, the sulphate and chloride ions are oxidized, and nickel ions from the anode are added to the plating bath. Therefore, during plating the nickel ions are plating out, but are also being replenished by the nickel anode. The iron ions, however, are not being replenished and are being depleted during deposition. While Ni-Fe baths should be discarded before the iron is totally depleted from the bath, this depletion of ions was the basis of the approach used in monitoring these baths.

For many years, researchers have studied the affect of salts in seawater on the propagation of sound [80,81]. Such studies were necessary for applications such as underwater sensing using sonar. In more recent years, research has been performed to investigate the affects of ions on the structure and thermodynamic properties of various solutions [82, 84]. Such studies have documented the behavior of the speed of sound in electrolytic solutions. Ions in polar solvents (e.g. water) change the structure of the solvent because of the alignment of the solvent dipoles with the ions [85]. The movement of water molecules from the bulk solution to the ion hydration shell increases

the order of the structure. Electrostriction results, where the volume of the solvent is compressed by the electric fields of the ions [75, 85]. Thus, the bulk modulus and the speed of sound through the solvent are increased [85].

While a thorough (microscopic) theoretical explanation is yet to be presented in literature, many experimental observations have been made displaying the increase in the speed of sound through electrolytes due to the increase in the ionic strength *I*, which is a measure of the electrical field due to the ions [73, 81]

$$I = \frac{1}{2}\sum c_i z_i^{\ 2} \tag{60}$$

Note that *I* is a function of the concentration of each ion c_i and the ion charge number z_i. This trend is also shown in some references as an increase in the speed of sound due to an increase in the salt molarity [80-85]. An increase in the density of the solution with increased ion concentrations has been observed as well. This affect on the speed of sound is less that that of the bulk modulus, however [81].

Thus, in experiments performed in this thesis, it was expected that as Ni-Fe was being deposited, iron was being depleted from the bath and the bulk modulus (and density) was decreasing. Therefore, the speed of sound through the bath was expected to decrease as well. Consequently, from Equation (59), one would expect that the (excess) pressure propagating through the bath would decrease.

In the electroplating set-up shown in Figure 34, a sound wave was generated by the loudspeaker and propagated through the bath. The acoustic sensor was implemented so that it sensed pressure changes in the bath by measuring the voltage generated on its surface. Before the start of the electroplating, a measurement was recorded from the sensor to obtain a reference measurement (of noise in room). The initial film of a Ni-Fe

electroplating bath is usually of poor quality, therefore a “dummy” sample was electroplated for 5 minutes to stabilize and condition the bath. Subsequent runs were then performed for 5, 15, 30, 45, 80, 150, and 20 minutes. At the end of each run the sample was removed and the sensor response was recorded. For each plating time period mentioned above, a new sample was used and the thickness was measured for each run using a profilometer to accurately measure the film thickness deposited. The sensor voltage recorded as a function of total thickness plated is shown in Figure 35.

This graph shows that the greater the thickness of the Ni-Fe electrodeposit, the smaller the magnitude of the sensor response recorded. Thus, it is reasonable to state that the pressure in the bath is decreasing with increasing thickness plated as a consequence of ions being plated out of the solution. Figure 35 displays a greater positive slope in region 1 than in region 2 of the graph. Region 1 includes the time period starting with the onset of deposition and during conditioning of the bath. One possible explanation for this difference between regions is that initially ions may deplete out of the system faster or non-uniformly until some stable condition is met resulting in the smaller slope in region 2. Rohman et al. [83] observed in experiments for monitoring the change in the speed of sound as a function of molarity in aqueous lithium nitrate solutions that there were changes in the slope of their speed vs. molarity graphs due to structural transitions in the aqueous solution. While such changes have not theoretically been explained, they have been cited and related to the structure of the primary hydration shell around the ions [83].

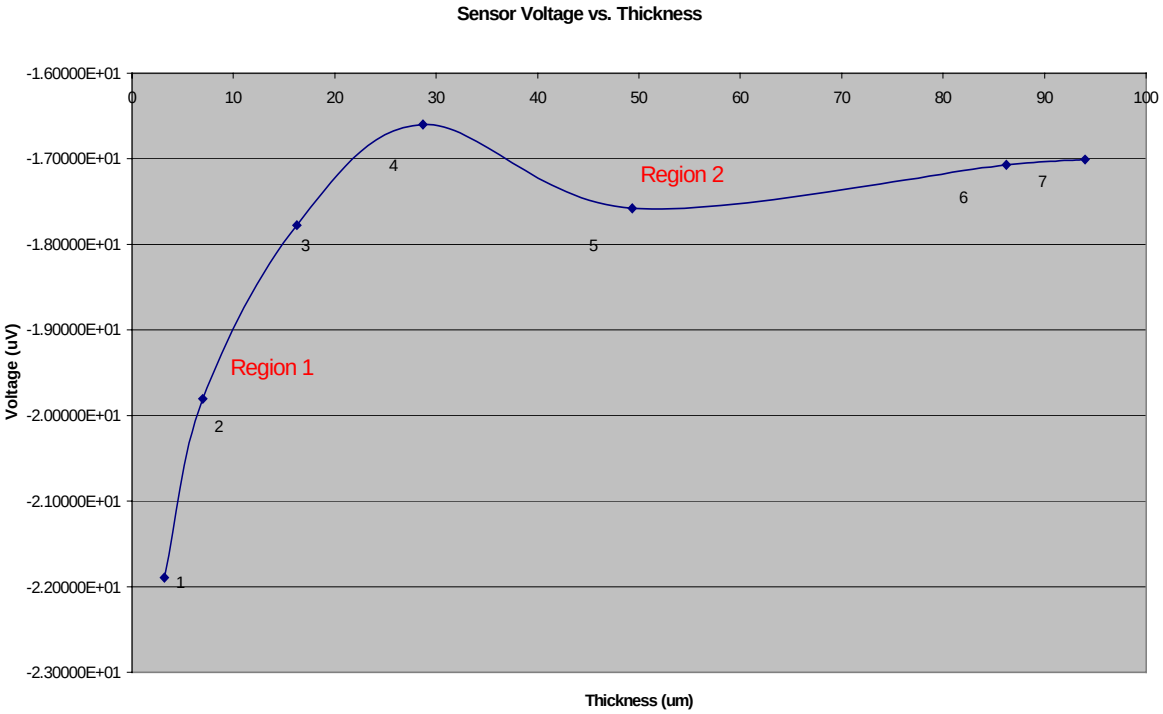

Figure 35. Sensor output voltage vs. Ni-Fe thickness.

6.5. Predictive Model for Metallization

Experiments can be used to generate inferences about a population based on a few observations. Sometimes, these experiments are performed in the absence of an explicit known relationship between the input factor(s) and the output response(s). In such cases, mathematical models can be used and statistical tests can be performed to try and describe and correlate the observations gleaned from the experiment.

The purpose of collecting the data for the experiments outlined in Section 6.4. was to map the output of the sensor to the Ni-Fe thickness measured. This enables the development of a predictive model for thickness as a function of sensor voltage and plating time. Such a model can be used to determine the thickness of a Ni-Fe deposit *in-*

situ based on the observed response of the sensor and duration of the deposition run. Note that the time used in the model should be the total electroplating time of the bath, not that of each individual run. Based on the theory presented, such a model is only valid when the time includes all times for which the ions have been plating out of the solution. For example, a 20-minute deposition process in a bath that has been previously used will yield a different sensor response than a 20-minute deposition run using a fresh plating bath.

The experimental data was analyzed using RS/Explore®. A linear (least squares) regression model was derived. Regression analysis is a statistical tool that determines the value of a response based on the relationship between that response and one or more variables. The analysis of variance (ANOVA) for the electroplating experiment is shown in Appendix B. The *F* statistic is used to determine whether the regression model explains a significant portion of the variance in the response. For this experiment, the statistic is $F = 4135.92/1.09 = 3811$. An *F* value this large would occur randomly only 0.000028% of the time if there were no true relationship between the thickness and the predictors (sensor voltage and plating time). Because this is a rare event, it is likely this model explains a statistically significant portion of the variation in the thickness (only factors with a significance level less than 0.05 are considered significant). The R^2 statistic provides an overall measure of the fit attained by the model. R^2 will have a value between zero and one, with one being the optimal value. The R^2 value for this model is 0.9995, and therefore, the model yields a good fit to the data supplied.

From least squares coefficients calculated for the model, the equation of the Ni-Fe thickness deposited is given by

$$T = 10.32 + 0.46V + 0.26M \quad (61)$$

where T is the thickness (μm), V is the voltage (μV), and M is the time (minutes). The RMS error for the model was 1.042 μm. Figures 36 and 37 are graphs of thickness vs. voltage and thickness vs. time, respectively. Both the experimental data and the data predicted from the regression model are plotted and labeled accordingly.

Neural networks were used as an alternative method to generate a model of the experimental data. Neural networks illuminate subtle relationships between sets of input and output parameters by performing complex mappings on arbitrary or non-linear data [86]. A neural network crudely resembles the architecture of the human brain. It consists of many elementary parallel processing units called "neurons." In a "black-box" configuration, multiple layers of neurons exist. The interconnection of the neurons enables the network to learn complex relationships between input and output patterns. These relationships are stored in the weights of the connections between the neurons. Each neuron contains the weighted sum of its inputs filtered by a non-linear sigmoidal function [86].

The neural network simulation software package, Object-Oriented Neural Network Simulator (ObOrNNS) developed by the Intelligent Semiconductor Manufacturing group at the Georgia Institute of Technology, was used to model the plating responses. ObOrNNS simulates feed-forward neural networks trained by the error back propagation (BP) algorithm. The neural network structure is shown in Figure 38.

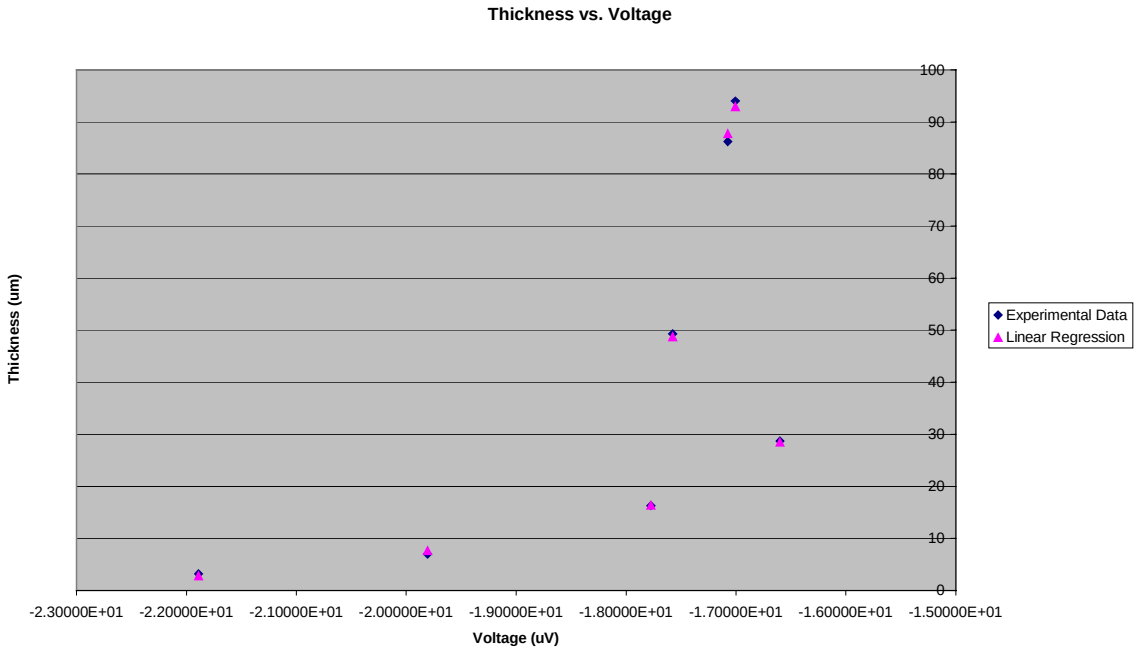

Figure 36. Experimental data and output from regression model for plating thickness vs. voltage.

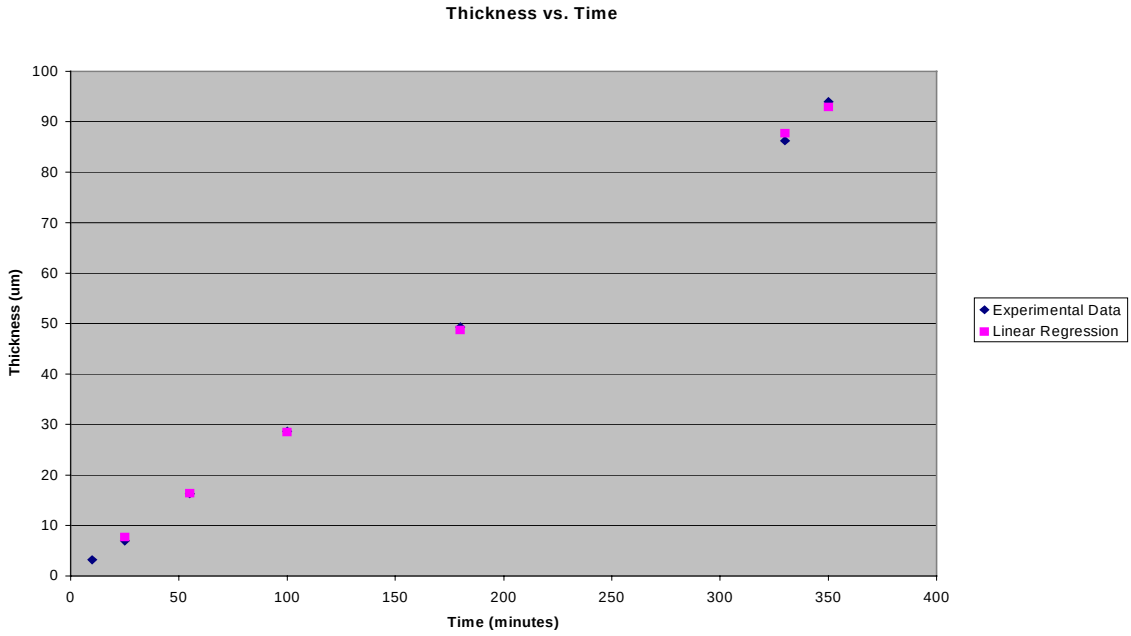

Figure 37. Experimental data and output from regression model for plating thickness vs. time.

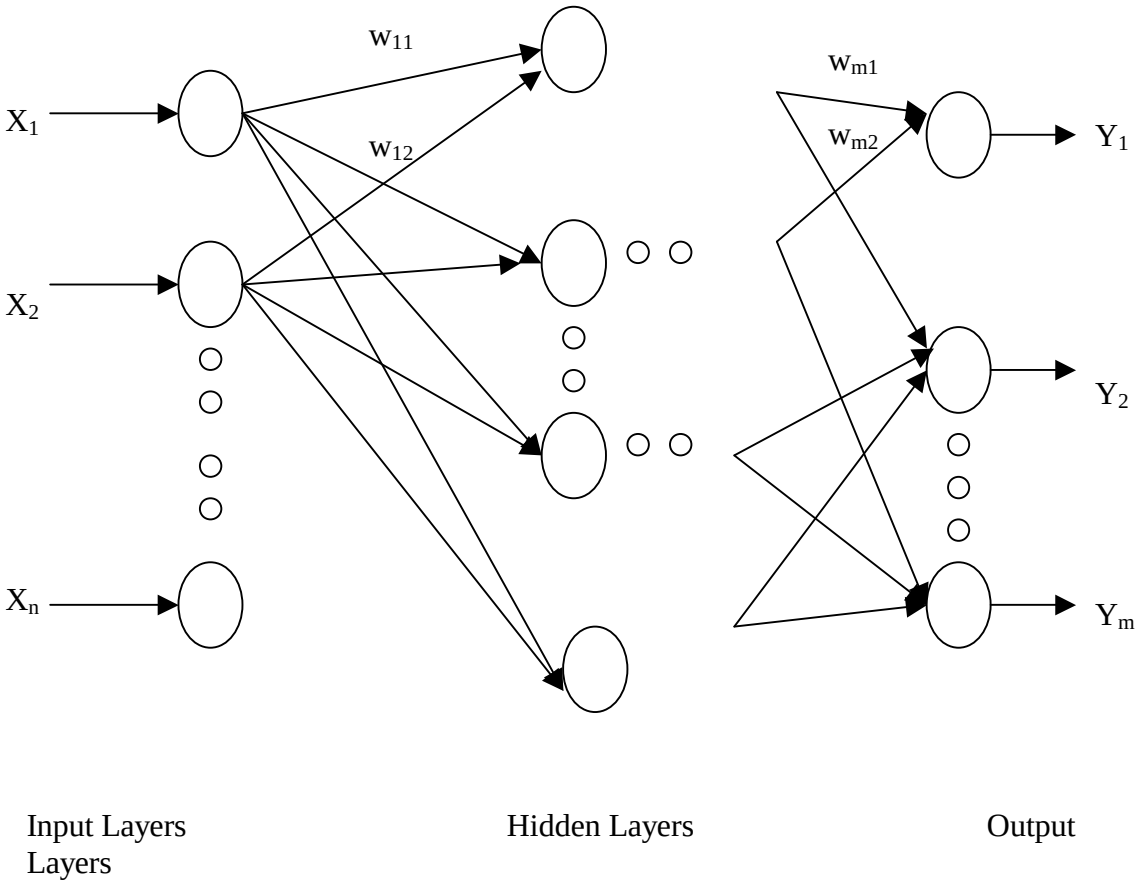

Figure 38. Feed-forward network showing input, hidden, and output layers.

The layers of neurons receive, process, and transmit information about the input and output parameters and the corresponding responses. For a three-layer structure with one input layer, one output layer, and one hidden layer, the input layer receives data corresponding to the input parameters to be modeled. The hidden layer, which does not interact with the outside world, assists in performing classification and feature extraction tasks on information provided by the input and output layers [86]. The output layer transmits the data once it has been fed through the neural network.

The BP algorithm is described as a supervised learning technique. The neural network is trained to learn the functional relationship between the input and output data. This is achieved by determining a set of network weights that facilitate mapping the desired process. Initially, random weights are used. An input vector is presented to the network, the inputs propagate through the layers and an output is calculated using the initial weight set. This output is compared to the target output data. The squared difference between the two vectors determines the system error. This error is propagated through the network backward. Learning occurs by reducing the error through modification of the weights by the gradient descent approach [86]. In this approach, the weights are adjusted in the direction of decreasing error. Once the network weights are updated, the procedure is repeated and the network is trained until the desired convergence is reached.

The neural network used for the electroplating dataset was a 3-layer network (1 input layer, 1 hidden layer, 1 output layer) with a 2, 2, 1 network structure (2 input layer neurons, 2 hidden layer neurons, 1 output layer neuron). Since it was small, the entire dataset (7 points) was used to train the network. The learning cycle was repeated until an

RMS error of 0.01 was achieved. The ObOrNNS display showing the data for two inputs (Input1 = sensor voltage, Input2 = plating time), the experiment output (Target1 = Ni-Fe thickness measured), predicted output (Output1 = predicted Ni-Fe thickness), and the error (Error) is shown in Figure 39.

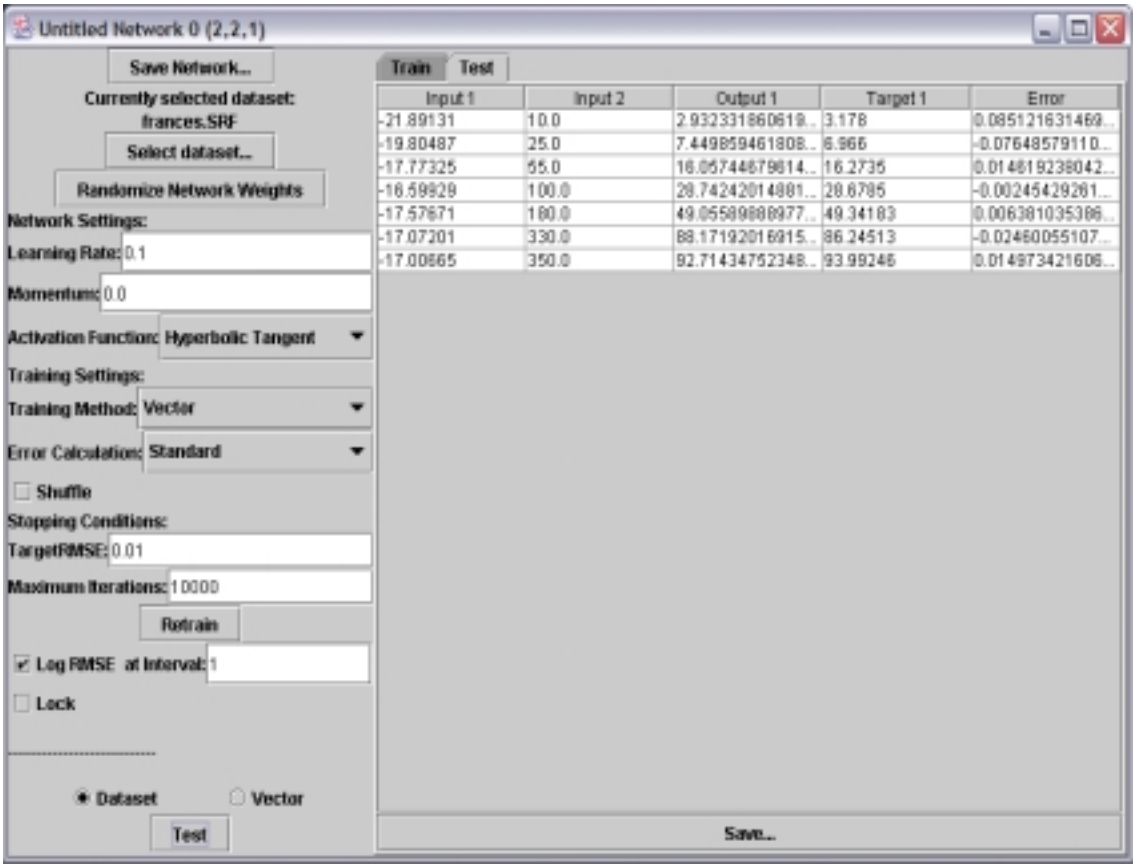

Figure 39. ObOrNNS display with input, output, target, and error data.

The neural network model that predicts the Ni-Fe film thickness is graphed in Figure 40 as a response surface. This is a 3-D model of the changes in thickness predicted due to changes in sensor voltage and plating time. The central oval area on the surface

signifies the data range of input and output parameters for the experiments performed. In this region, an increase in Ni-Fe thickness can be observed for increasing time and decreasing voltage magnitude. This model was more accurate in modeling the electroplating thickness than the regression model presented previously, as the RMS error of the neural network model is 0.01 (μm) and the RMS error for the regression is 1.042 (μm).

In real manufacturing applications, these models can be used to determine the thickness of a nickel–iron electrodeposit by recording the output voltage of the acoustic sensor and the total time that has elapsed for the electroplating process. These two inputs would then be used either in Equation (61) or entered into the neural network model created by ObOrNNS as inputs to determine the predicted Ni-Fe thickness in real time.

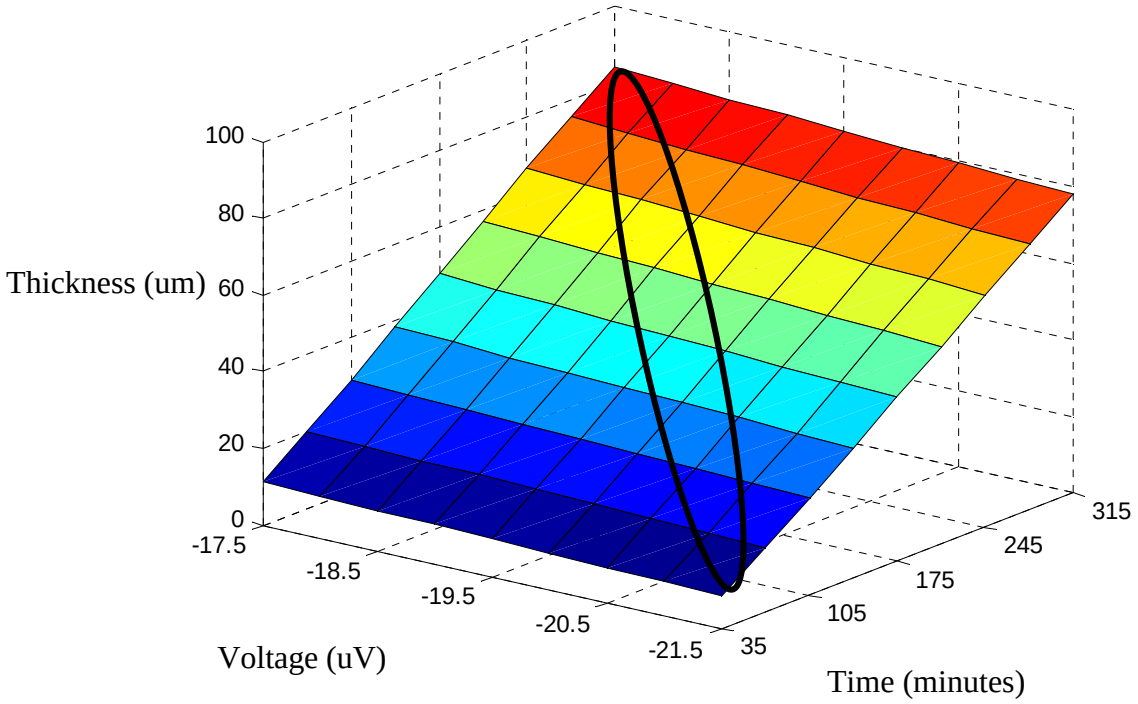

Figure 40. Response surface graph generated from ObOrNNS.

CHAPTER 7

CONCLUSION

Today's technology is driven by the concepts of "better and faster, yet smaller and cheaper." The computer, biomedical, defense, and automotive industries are at the forefront of this push. Integration of improved microelectronic devices is one method used to meet this demand. Semiconductor manufacturing techniques must continue to evolve to accommodate advances in this ever changing field. Therefore, monitoring and control of microfabrication processes are critically important. Process monitoring is necessary to alleviate processing errors and miscalculations, and provides for increased device yield while maintaining relatively low costs.

It has been demonstrated in this thesis that acoustic techniques are promising for monitoring and control of semiconductor fabrication equipment and processes. Acoustic devices can generally serve as non-invasive, relatively simple, *in-situ* process sensors. They can be fabricated at low cost, in batches, and with good reproducibility using IC fabrication techniques. Compared to the existing optical monitoring methods that rely on "looking" at the process to monitor its status, acoustic sensors tend to be smaller, cheaper, and provide equally precise measurements of process parameters. They can sense a wide range of parameters with fewer limitations. For precision, however, it may be beneficial to consider using acoustical and optical techniques as complementary methods. This could further enhance the amount and sensitivity of data collection to facilitate process diagnostics and control.

This thesis investigated the use of an acoustic sensor for *in-situ* monitoring of electrochemical deposition processes. These processes are used in the semiconductor industry to deposit various metals on substrates in aqueous solutions. Metals are used for contacts and interconnects on circuit boards, as etch masks, and in the creation of micromachined magnetic devices. By employing IC and micromachining techniques, the author was able to design, fabricate, and implement a piezoelectric acoustic sensor to provide a novel approach for monitoring electroplating. During a nickel-iron electroplating process, sensor data and plating time were mapped to the measured alloy thickness to yield an empirical relationship between the variables. Thus, a predictive model for the metallization of nickel-iron was developed, potentially leading to real-time monitoring of Ni-Fe film thickness during electroplating.

7.1. Summary of Contributions

The goal of this research was to design and fabricate an acoustic sensor that will provide process monitoring of electroplating. Thus, acoustic sensors were initially studied to identify a viable process sensor. The acoustic sensor selected was a piezoelectric microphone. This microphone uses a thin bendable membrane as its sensing element. This device operates based on the piezoelectric effect, where a mechanical stress deforms the membrane and generates an electric charge on the piezoelectric layer. Piezoelectric sensors can be realized on-chip, with a simple design, and without the air-gap losses associated with other acoustic sensors. Piezoelectric materials convert mechanical energy into electrical energy and vice versa; therefore, an excitation voltage or supply current is not required for these type devices.

The substrates used for the sensors were made of silicon, a non-piezoelectric material. They therefore required the addition of a piezoelectric film. There are various piezoelectric films used in microsensors structures. However, zinc oxide was the piezoelectric material chosen because it possesses suitable properties and because of ease of processing.

The design of the sensor consisted of a membrane, a piezoelectric layer, and segmented surface electrodes. To optimize performance, the sensor was modeled using finite element analysis software. The results of the analysis indicated that movement of the sensor's membrane due to sound pressure experiences the greatest bending stress in the middle and outer region of the defined diaphragm area. Thus, electrodes were placed in these regions on the sensor surface.

The sensor was fabricated using IC and micromachining techniques, enabling the batch fabrication of small, precise devices that could be reproduced. Two-inch silicon wafers were used as the substrate, and most of the processing was performed in the cleanroom. Some processing difficulties arised in forming the sensor membrane. Because two-sided processing was employed, a method had to be devised to protect the ZnO on the front-side while etching the membrane into the backside with KOH. A PDMS sealing ring was applied to the backside. The ring self-adhered to the wafer and formed a ridge around the periphery of the wafer, allowing a small amount of the etchant to be placed on the backside only.

Because the acoustic sensor consists of a diaphragm, the mechanical theory of thin plates was used to provide the background for describing the behavior of the diaphragm

when subjected to a mechanical load. This theory, along with the piezoelectric equations, was used to derive the analytical expression for sensor sensitivity.

Because of the high impedance and low output charge of the piezoelectric sensor, a charge amplifier from ThermOptics (DN 620) was used to amplify the sensor's output. This inverting amplifier was used to convert the high impedance sensor output to a low impedance voltage signal and served as an interface between the device and the spectrum analyzer. The piezoelectric sensor incorporating the amplifier was modeled using an equivalent electrical circuit, and the expression for the output of the circuit was determined. The sensitivity, which is expressed as the output produced for a given input, was calculated theoretically and verified experimentally. Discrepancies between the measured and theoretical values were attributed to electrical noise from the equipment and cables, acoustical interference in the non-anechoic room, and differences between the idealized values used in the derivations and the actual real life values of these parameters.

The proposed variation of acoustic velocity with molarity was verified experimentally using a commercial piezoelectric sensor. The acoustic sensor was then incorporated into a nickel-iron electroplating bath to monitor the deposition process *in-situ*. To facilitate this, the theory and mechanisms of electrochemical deposition were described. This theory indicated that for certain electroplating baths, ions plated out are not replenished during deposition. Such plating bath changes alter the behavior of a sound wave propagating through the fluid. A loudspeaker was used to launch a sound wave through the bath during deposition runs. The sensor was used to monitor the pressure changes and indirectly, the changes in the electroplating bath. The sensor output and the time of

the plating deposition were used to predict the Ni-Fe thickness, which was measured after each deposition run.

Statistical analysis and neural networks were used to map the output of the sensor and the plating time to the Ni-Fe thickness. RS/Explore was used to perform a linear regression analysis on this data. A regression model was generated that provided a good fit to the experimental data. This model derived an equation of metal thickness as a function of sensor output and plating time. The ObOrNNS neural network simulation package was also used to generate a model of the experimental data. The trained neural network established a model for the predicted thickness based on test input data. This data set (inputs and predicted output) was graphed as a response surface model to observe Ni-Fe electroplating process trends. The predictive models developed can be used to provide real-time monitoring of Ni-Fe electroplating.

7.2. Future Work

An initial extension of this work would be to improve the models and make them more robust. This would include performing more deposition runs. This would provide more data points for analysis, making the models more accurate. Also, it is known that the speed of sound in fluids is dependent on the temperature. Any substantial variations in temperature that were unaccounted for would affect the sensor response for the current sensing approach. Therefore, solution temperature is another potential input parameter that could be incorporated into the current models.

It is also known that control conditions for electroplating not only include solution composition, but also temperature, pH, agitation, and current density [16]. If any of these

other factors vary during the deposition process, the thickness may be affected as well. The more parameters that are measured and used as inputs (predictors) for the model, the more accurate the predicted response will be. To measure these parameters, however, would entail adding more equipment and limiting the simplicity of this approach.

This monitoring method is currently being used for nickel-iron plating, but there may be other electroplating bath solutions for which this approach is applicable. Therefore, it would be beneficial to identify single metal or other alloy depositions where the sensing method used in this thesis is useful.

It may be desired that the metal ion concentration be determined during electroplating. Such monitoring could be used to detect solution composition deviations from a set concentration range. Current methods of measuring metal ion concentration include colorimetry, polarography, and ion selective electrodes [15, 87]. The acoustic sensor could be incorporated to predict the concentration of metal ions during electroplating. For example, in the experiments performed in this thesis where iron was being plated out of the bath, if a separate set of experiments were performed that measured the sensor output at various colorimeter readings yielding iron concentration, the iron ion concentration as a function of sensor output response could be mapped. This could be used to inform the operator when iron ions have been plated out. Moreover, during electroplating depositions, alloy thickness and iron concentration can be monitored simultaneously.

Another direction for future work would be to improve the sensor used. One of the first modifications to the sensor presented in this thesis would be to incorporate on-board

electronics into the sensor chip. Such integration will increase the sensor sensitivity and reduce parasitic capacitance [54].

Finally, it may be desirable to investigate other sensing mechanisms using acoustic sensors. Flexural plate wave devices may be of interest, as they are capable of operating in liquids. The ability to monitor an electroplating bath using a sensor located inside of the bath may provide a very sensitive sensor response. It may also lead to a sensing method that can monitor metals for which the method presented here cannot: baths where the ions are being replenished.

APPENDIX A

TIME DELAY EXPERIMENTS

Preliminary experiments were performed to demonstrate the behavior of sound waves in electrolytic solutions. This was accomplished by monitoring the time delay t_d (or phase shift, $\phi = 2\pi f t_d$) of a sound wave propagating through an electrolyte. The time delay of a signal represents the time it takes for the signal to propagate through a medium. If the distance d that the wave has traveled is also known, the velocity ν of that wave can be calculated by $\nu = d/t_d$. The change in velocity between two measurements, one with an initial velocity ν_o and time delay t_o and the other with a velocity ν_1 and time delay t_1, is given by

$$\Delta \upsilon = \upsilon_1 - \upsilon_0 = d\left[\frac{1}{t_1} - \frac{1}{t_0}\right] = \frac{d}{t_0}\left[\frac{-\Delta t}{t_1}\right] \tag{61}$$

or

$$\Delta \upsilon = \upsilon_0\left[\frac{-\Delta t}{t_0 + \Delta t}\right] = \upsilon_0\left[\frac{-\Delta t}{\frac{d}{\upsilon_0} + \Delta t}\right] \tag{62}$$

Measurements were initially performed with a commercial Murata piezoelectric sensor to verify that the experimental set-up (see Figure 41) would be effective in measuring the time delay of a sound wave. The sensor was first placed in front of the loudspeaker at a distance of 2 cm. The sensor output was amplified using circuitry employing a charge amplifier. The loudspeaker was pulsed at 100 Hz with an amplitude of 1.080V and a duty cycle of 1%. The signal from the function generator was connected

to channel 1 of a Tektronix oscilloscope and was used as a trigger. The output from the sensor was measured on channel 2 of the oscilloscope.

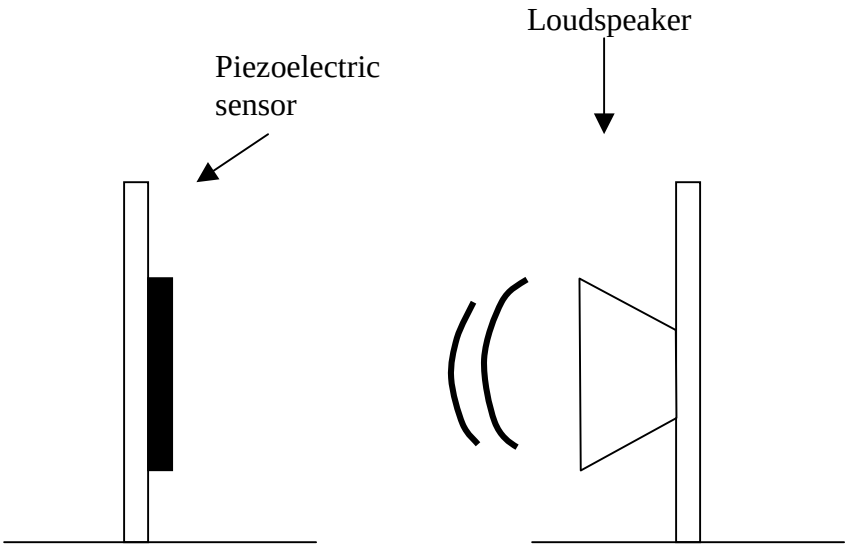

Figure 41. Sensor/loudspeaker measurements.

To calculate the time delay of the sensor output, one peak in the output signal was used as a reference point and the movement of a second peak in the output was tracked. The difference between the two yields the cumulative time delay. The distance between the loudspeaker and sensor was increased at 1 cm increments until a distance of 10 cm was reached. At each location the time delay was recorded. The (cumulative) time delay increased for each increment and the average time delay between each 1 cm increment (Δt_d) was approximately 29.4 μs, which yielded a velocity (through air) of 340 m/s. This value is very close to the value of the speed of sound in air (343 m/s at 20°C). The time delay at each distance is given below.

The ultimate goal of these preliminary experiments was to validate the concept of using an acoustic sensor for monitoring electrochemical deposition. Section 6.4. of this thesis presents the relevant theory to describe the behavior of sound in electrolytic solutions. It was noted there that the speed of sound through electrolytes increases due to an increase in salt molarity [73, 81].

Table 4. Time delay measurements.

Distance of sensor from speaker (cm)	Cumulative Time Delay (μsec)	Time differences (Δt_d) (μsec)
2	0	(used as reference)
3	30	30
4	58	28
5	87	29
6	117	30
7	146	29
8	176	30
9	206	30
10	235	29

An electroplating bath container was placed between the sensor and the loudspeaker of the set-up shown in Figure 41. The container was approximately 9 cm wide on each side. The container was then filled with de-ionized (DI) water. The loudspeaker was driven using a sinusoidal input at 2.3 kHz (1.5 V amplitude, 1 V offset). It was attached

to one side of the beaker, and the sensor was placed on the opposite end. The delay of the sensor output relative to the input sine wave was observed. This was accomplished by monitoring the time shift between the peak amplitude of the source and that of the sensor. The time delay was found to be 44 μs for DI water.

Twenty-five grams of sodium chloride (NaCl) were then dissolved in 500 ml DI water and its time delay was calculated. The change in time delay Δt was determined at this salt concentration. Then fifty grams of salt were dissolved in 500 ml HI water. The time delay through the solution was measured and Δt was determined. The results of this experiment are shown in Table 5 and plotted in Figure 42.

Table 5. Salt molarity and time delay.

Salt concentration (g)	Salt molarity (mol/L)	t_d (μs)	Δt (μs)
0	0	44	0
25	.85558	28	-16
50	1.711	20	-24

The experimental results agree with the observations in the literature that changes in the ionic strength of a solution change the speed of sound in the solution. It was shown in this experiment that as the salt molarity increases, the change in the time delay for each measurement decreases and thus, the velocity of the sound wave propagating through the fluid increases.

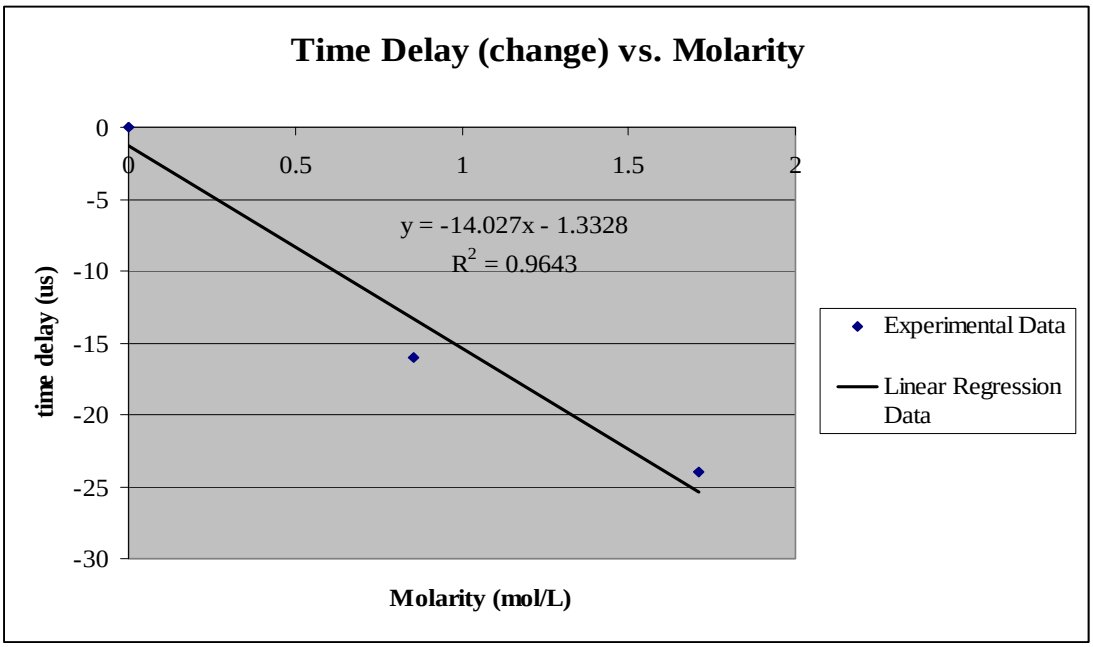

Figure 42. Time delay vs. molarity.

Since it was demonstrated that the time delay of a sound wave changes as molarity changes, experiments were also performed in an actual electroplating bath. The set-up of this experiment is shown in Figure 43. The set-up used a Ni-Fe bath and its composition is given in Table 3. A copper coated circuit board with an area of 25 cm^2 was used as the plating sample for the Ni-Fe electrodeposit. A platinum anode was used to ensure that maximum ion depletion was occurring, allowing for better monitoring of the time delay during the process. The goal of this experiment was to see if the changes in an Ni-Fe electroplating bath produce enough changes during plating to actually yield a measurable change in the velocity of the sound wave.

Five hundred milliliters of the plating solution were poured into the electroplating container, and the loudspeaker and Murata sensor were attached to opposite sides of the container. The sample was weighed on a scale and its mass was 8.43g. It was then placed

at the cathode and was immersed along with the anode into the plating bath. A thermometer was used to measure the temperature and the temperature was maintained at a constant value (28 °C). The loudspeaker was driven by a sinusoidal input (1 V amplitude, 1 V offset), and the time delay was measured. The delay was obtained by measuring the distance between the peak amplitude of the source signal and that of the output of the sensor. The distance between these same two peaks were measured throughout the plating experiments to ensure that the measurements were not shifted a period. A current of 250 mA was then applied to the electrodes to start electrodeposition. The time delay of the signal was measured every ten minutes and recorded. After 60 minutes, the sample was removed and weighed to determine the mass of Ni-Fe plated. Four more electroplating runs were performed for 30 minutes each. During these trials, the time delay was calculated at the start and end of each plating run, as well as in 10-minute intervals during plating. After each thirty minute period, the mass of the Ni-Fe plated was determined. The change in the time delay (Δt) was measured for each plating interval, using the time delay obtained from the bath at the onset of plating and the time delay measured at the completion of the process for that interval. The total Ni-Fe plated was 0.436 μm thick. The results of these experiments are shown in Figure 44. This deposit was 80% Ni and 20% Fe, and the results are presented in terms of Ni deposited.

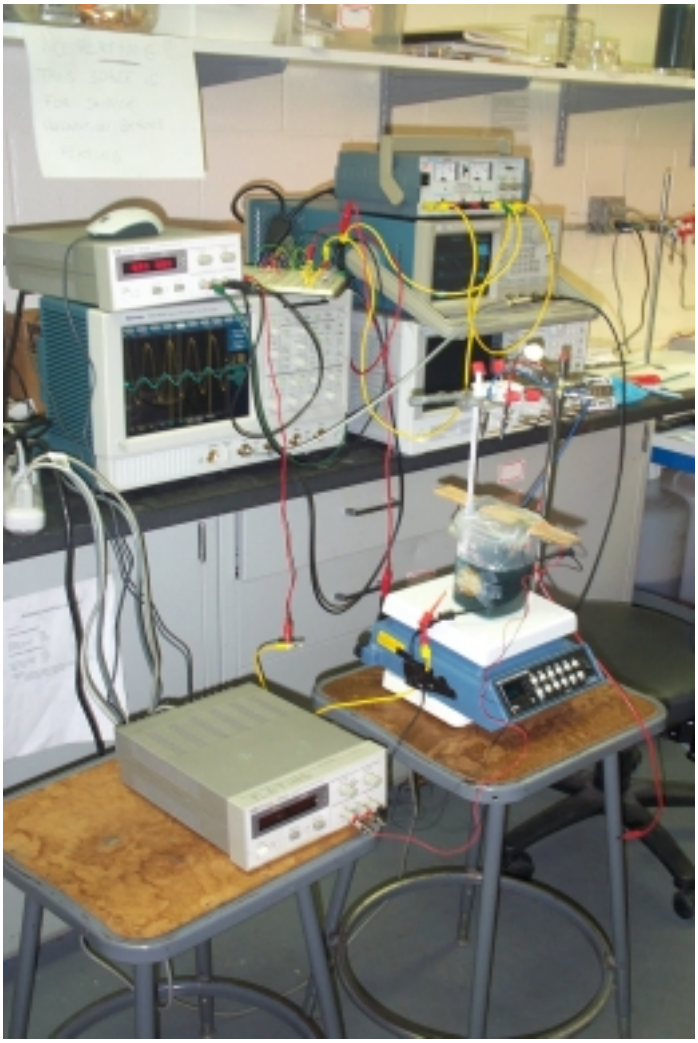

Figure 43. Electroplating set-up for measuring time delay.

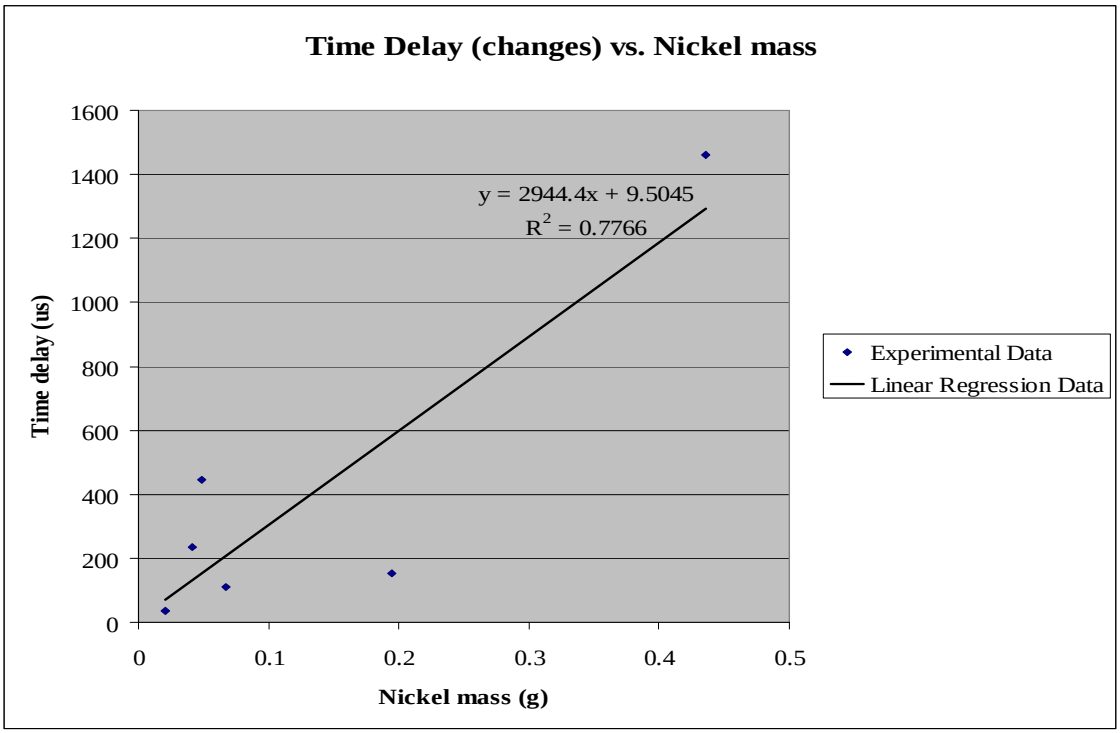

Figure 44. Time delay vs. nickel mass.

The graph shows an approximate linear relationship between time delay and nickel deposited during electroplating. The time delay measured is a relative measurement and while it is proportional to velocity, there is some uncertainty about the reference in which these values were obtained. However, these measurements demonstrate that the changes in velocity are real and observable. Based on theory, it is reasonable to assume that the velocity changes with molarity.

Equation 62 can be re-arranged to express the fractional change in velocity due to changes in time delay

$$\frac{\Delta \upsilon}{\upsilon_0} = -\frac{\Delta t}{\frac{d}{\upsilon_0} + \Delta t} \tag{63}$$

where d is the distance of propagation (for the container d = 0.09cm). For the first Ni-Fe electroplating time interval, Δt = 152 μs. Because a value of the speed of sound in Ni-Fe plating baths was not available in the literature, the sound velocity (1700 m/s) of magnesium sulphate salt at a similar molarity was used for v_0 to determine the feasibility of the results obtained. Substituting these numbers in Equation 63 yields a 70% decrease in velocity due to changes in time delay during Ni-Fe electroplating. While this number is more than expected, it is not totally unreasonable. Moreover, some other factors could have affected the velocity including reflections off of the container sidewalls, slight shifting of the signal between measurements taken (from turning signal on/off), or circuitry phase delay.

Nonetheless, the goal of these preliminary experiments was to observe that the changes in molarity during electroplating yield real, measurable changes in the acoustic signal. This objective was achieved. Based on the findings in this section, an acoustic sensor was proposed to be used as a process monitor for electroplating processes. While its monitoring technique is different, these results validate the concept of its implementation.

APPENDIX B

STATISTICAL MODEL RESULTS

Table 6. ANOVA table for response thickness *T*.

Source	**DF**	**Sum Sq.**	**Mean Sq.**	***F*-Ratio**	**Significance**
Total	6	8276.17			
Regression	2	8271.83	4135.92	3811.00	0.00000028
Residual	4	4.34	1.09		

Table 7. Least squares coefficients for regression model.

Predictor	**Coefficient**	**Standard Error**	***T*-value**	**Significance**
1	10.32	5.75		
V	0.46	0.29	1.58	0.19
M	0.26	0.00	65.28	0.00

R-sq = 0.9995

REFERENCES

1. "International Technology Roadmap for Semiconductors 2002 Update," http://public.itrs.net/Files/2002Update/2002Update.pdf.

2. Rao Tummala, ed. Fundamentals of Microsystems Packaging. New York: McGraw-Hill, 2001.

3. S. Limanond, J. Si and K. Tsakalis. "Monitoring and Control of Semiconductor Manufacturing Processes." IEEE Control Systems Magazine. 18 (6) (December 1998): 46-58.

4. M. Moslehi, R. Chapman, A. Parnjpe, H. Najm, J. Kuehne, R. Yeakley and C. Davis. "Single-wafer Integrated Semiconductor Device Processing." IEEE Transactions on Electron Devices. 39 (1) (January 1992): 4-32.

5. Jimmy Hosch. "Process Control Sensor Development for the Automation of Single Wafer Processors." Proceedings of SPIE—Advanced Techniques for Integrated Circuit Processing. 1392 (1990): 555-562.

6. Mehrdad Moslehi. "Noninvasive sensors for In-Situ Process Monitoring and Control in Advanced Microelectronics Manufacturing." Proceedings of SPIE—Rapid Thermal and Related Processing Techniques. 1392 (1991): 280-294.

7. T. Knight, D. Greve, X. Cheng and B. Krogh. "Real-Time Multivariable Control of PECVD Silicon Nitride Film Properties." IEEE Transactions on Semiconductor Manufacturing. 10 (1) (February 1997): 137-146.

8. D. Ballatine, R. White, S. Martin, A. Ricco, E. Zellers, G. Frye, H. Wohltjen. Acoustic Wave Sensors. New York: Academic Press, 1997.

9. A. Iturralde. "Sensing Technologies for Semiconductor Process Applications." Proceedings of SPIE—Process, Equipment, and Materials Control in IC Manufacturing. 2637 (1995): 91-101.

10. M. Hoummady, A. Campitelli and W. Wlodarski. "Acoustic Wave Sensors." Smart Materials and Structures. 6 (6) (December 1997): 647-657.

11. J. Grate, S. Martin, R. White. "Acoustic Wave Microsensors." Analytical Chemistry. 65 (21) (1 November 1993): 940-948.

12. M. Vellekoop. "Acoustic Wave Sensors and Their Technology." Ultrasonics. 36 (1-5) (February 1998): 7-14.

13. Gregory Kovacs. Micromachined Transducers Sourcebook. Boston: WCB/McGraw-Hill, 1998.

14. Eric Ollard. Introductory Electroplating. Teddington: Robert Draper Limited, 1968.

15. Mordechay Schlesinger and Milan Paunovic, eds. Modern Electroplating, Fourth Edition. John Wiley and Sons, Inc.: New York, 2000.

16. Marc Madou. Fundamentals of Microfabrication. New York: CRC Press, 1997.

17. http://electrochem.cwru.edu/ed/encycl/art-e01-electroplat.htm.

18. J. Y. Park and M. G. Allen. "Development of Magnetic Materials and Processing Techniques Applicable to Integrated Micromagnetic Devices." Journal of Micromechanics and Microengineering. 8 (4) (December 1998): 307-316.

19. W. Taylor, M. Schneider, H. Baltes, and M. Allen. "A NiFeMo Electroplating Bath for Micromachined Structures." Electrochemical and Solid-State Letters. 2 (12) (1999): 624-626.

20. Richard Jaeger. Introduction to Microelectronic Fabrication. New York: Addison-Wesley Publishing Co., 1993.

21. D. White, D. Boning, S. Butler, and Gabe Barna. "Spatial Characterization of Wafer State Using Principal Component Analysis of Optical Emission Spectra in Plasma Etch." IEEE Transactions on Semiconductor Manufacturing . 10 (1) (February 1997): 52-61.

22. P. Banks, W. Pilz, I. Hussla, G. Lorenz, and G. Castrischer. "In-Situ Diagnostics for Plasma Processing." Monitoring and Control of Plasma-Enhanced Processing of Semiconductors. James Griffiths, Ed. Proc. SPIE 1037, 35-42.

23. M. Konuma. Film Deposition by Plasma Techniques. New York: Springer-Verlag, 1992.

24. D. Manoes and D. Flamm. Plasma Etching: An Introduction. New York: Academic Press, 1989.

25. Michael Baker, Frances Williams, and Gary May. "A Novel In-Situ Monitoring Technique for Reactive Ion Etching Using a Surfaced Micromachined Sensor." IEEE Transactions on Semiconductor Manufacturing. 11 (2) (May 1998): 254-265.

26. M. Meyyappan, D. Economou, and S. Butler. Process Control, Diagnostics, and Modeling in Semiconductor Manufacturing. New Jersey: The Electrochemical Society, Inc., 1995.

27. W. Lochte-Holtegreven. Plasma Diagnostics. New York: American Institute of Physics, 1995.

28. Stephen Campbell. The Science and Engineering of Microelectronic Fabrication, Second Edition. New York: Oxford University Press, 2001

29. Ron Iscoff. "In-Situ Deposition Rate Monitoring for Thin Films." Semiconductor International. 17 (9) (August 1994): 5p.

30. http://www.uta.edu/optics/research/ellipsometry/ellipsometry.htm.

31. E. Irene. "Applications of Spectroscopic Ellipsometry to Microelectronics." Thin Films. 233 (1-2) pt. 1 (12 October 1993): 96-111.

32. J. Hilfiker and R. Synowicki. "Spectroscopic Ellipsometry for Process Applications." Solid State Technology. 39 (10) (October 1996): 157-164.

33. www.efunda.com/designstandards/sensors/pyrometers/pyrometers_theory.cfm.

34. J. Fraden. Handbook of Modern Sensors: Physics, Designs, and Applications—2nd Edition. New York: Springer-Verlag, 1996.

35. M. Motamedi. "Acoustic Sensor Technology." IEEE MTT-S International Microwave Symposium Digest. 1 (1994): 521-524.

36. W. Kühnel, J. Franz, D. Hohm, G. Heβ. "Silicon Subminiature Microphones for Airborne Sound." Acustica. 73 (1991): 90-99.

37. J. Franz and D. Hohm. "Silicon Acoustic Sensors." Eurocon '86: Part 2. (1986): 156-161.

38. G. Sessler. "Silicon Microphones." Journal of the Audio Engineering Society. 44 (1/2) (January/February 1996): 16-21.

39. G. Sessler. "Acoustic Sensors." Sensors and Actuators A. 25-27 (1991): 323-330.

40. P. R. Scheeper, A.G.H. van der Donk, W. Olthuis, P. Bergveld. "A Review of Silicon Microphones." Sensors and Actuators A. 44 (1994): 1-11.

41. S. M. Sze. Semiconductor Sensors. New York: Wiley-Interscience, 1994.

42. Y. Lee, L. Degertekin, J. Pei, B. Khuri-Yakub, and K. Saraswat. "In-Situ Acoustic Thermometry and Tomography for RTP." Technical Digest-International Electron Devices Meeting. (1993): 187-190.

43. J. Pei, L. Degertekin, B. Honein, B. Khuri-Yakub, and K. Saraswat. "In-Situ Thin Film Thickness Measurement Using Ultrasonics Waves." 1994 IEEE Ultrasonics Symposium. Pt. 2 (1994): 1237-1240.

44. Susan Morton, F. L. Degertekin, and B. Khuri-Yakub. "Ultrasonic Sensor for Photoresist Processing Monitoring." IEEE Transactions on Semiconductor Manufacturing. 12 (3) (August 1999): 332-339.

45. H. Rosemary Taylor. Data Acquisition for Sensor Systems. New York: Chapman and Hall, 1997.

46. Joel Rosenbaum. Bulk Acoustic Wave Theory and Devices. Boston: Artech House, 1988.

47. http://www.efunda.com/materials/piezo.

48. P. Chen, R. Muller, R. M. White, and R. Jolly. "Thin Film ZnO-MOS Transducer with Virtual DC Response." IEEE Proceedings of Ultrasonics Symposium. (1980): 945-948.

49. G. B. Clayton. Operational Amplifiers, second ed. Boston: Newnes-Butterworths, 1979.

50. Klaas Klaasen. Electronic Measurement and Instrumentation. New York: Cambridge University Press, 1996.

51. R. Schellin, G. Hess, W. Küehnel, G. Sessler, and E. Fukada. "Silicon Subminiature Microphones with Organic Piezoelectric Layers." IEEE Transactions on Electrical Insulation. 27 (4) (August 1992): 862-871.

52. M. Royer, J. Holmen, M. Wurm, and O. Aadland. "ZnO on Si Integrated Acoustic Sensor." Sensors and Actuators. 4 (3) (November 1983): 357-362.

53. http://www.ansys.com

54. Michele Royer. U.S. Patent #4,445,384, May 1984.

55. E.-S. Kim, J. Kim, R. Muller. "Improved IC-compatible Piezoelectric Microphone and CMOS Process." Transducers '91: 1991 International Conference on Solid-State Sensors and Actuators. (1991): 270-273.

56. A. Dewa,W. Ko, C. Liu and M. Mehregany. "Introduction to Microelectro-mechanical Systems and the Multi-user MEMS Processes." CWRU-MCNC, MEMS-MUMPS Short Course, June 14-16, 1995.

57. J. Bryzek, W. McCulley and K. Petersen. "Micromachines on the March." IEEE Spectrum (May 1994): 20-31.

58. K. Gabriel, R. Howe, R. Muller and W. Trimmer. "Silicon Micromechanics: Sensors and Actuators on a Chip." IEEE Spectrum (July 1990): 29-35.

59. M. Elwenspoek and H.V. Jansen. Silicon Micromachining. Cambridge University Press: New York, 1998.

60. Ljubisa Ristic. Sensor Technology and Devices. Massachusetts: Artech House, 1994.

61. H. Seidel, L. Csepregi, A. Heuberger and H. Baumgartel. "Anisotropic Etching of Crystalline Silicon in Alkaline Solutions: I. Orientation Dependence and Behavior of Passivation Layers." Journal of the Electrochemical Society 137(11) (November 1990): 3612-3626.

62. A. Cimpoiasu, N.M. van der Pers, Th. H. de Keyser, A. Venema, and M.J. Vellekoop. "Stress control of piezoelectric ZnO films on silicon substrates." Journal of Smart Materials and Structures. 5 (6) (December 1996): 744-750.

63. Michael Vellekoop, A. Venema, C. Visser, and P. Sarro. "Processing and Passivation of Zinc Oxide Films in Silicon Applications." Ceramic Bulletin. 69 (9) (1990): 1503-1505.

64. M. J. Vellekoop, C. Visser, P. Sarro, and A. Venema. "Compatibility of Zinc Oxide with Silicon IC Processing." Sensors and Actuators. A21-A23 (1990): 1027-1030.

65. J. Brugger, G. Beljakovic, M. Despont, H. Biebuyck, N. de Rooij, P. Vettiger. "High-yield Wafer Chuck for Single-sided wet etching of MEMS Structures." Transducers '97: 1997 International Conference on Solid State Sensors and Actuators. (16-19 June 1997): 711-713.

66. Eun Sok Kim. "Integrated Microphone with CMOS Circuits on a Single Chip." Ph.D. Dissertation Report, University of California at Berkeley, November 1990.

67. A. C. Ugural. Stresses in Plates and Shells. New York: McGraw-Hill Book Company, Inc., 1999.

68. S. Timoshenko and S. Woinowsky-Krieger. Theory of Plates and Shells. New York: McGraw-Hill Book Company, Inc., 1959.

69. D. Crisler, J. Cupal, A. Moore. "Dielectric, Piezoelectric, and Electromechanical Coupling Constants of Zinc Oxide Crystals." Proceedings of the IEEE. 56 (February 1968): 225-226.

70. S. Timoshenko, D. H. Young, and W. Weaver, Jr. Vibration Problems in Engineering. New York: John Wiley and Sons, 1974.

71. http://www.maxtekinc.com/products/plating/.

72. S. Yoshihara, T. Shirakashi, N. Kudoh, and W. Oikawa. "In-situ Monitoring of the Electroplating Process and Its Photocathodic Protection from Corrosion of Fe-Cr Alloy by the Use of Quartz Crystal Microbalance." http://www.arofe.army.mil/Conferences/Recent_Abstract/200th_Meeting/symposia/e1/0762.pdf.

73. J. N. Murrell and A. D. Jenkins. Properties of Liquids and Solutions, Second Edition. New York: John Wiley and Sons, 1994.

74. M. Paunovic and M. Schlesinger. Fundamentals of Electrochemical Deposition. New York: John Wiley and Sons, 1998.

75. John Burgess. Ions in Solution: Basic Principles of Chemical Interactions. New York: John Wiley and Sons, 1988.

76. Jae Yeong Park and Mark Allen. "Integrated Electroplated Micromachined Magnetic Devices Using Low Temperature Fabrication Process." IEEE Transactions on Electronics Packaging Manufacturing. 23 (1) (January 2000): 48-55.

77. Harris Benson. University Physics, Revised Edition. New York: John Wiley and Sons, 1996.

78. D. Halliday and R. Resnick. Physics. New York: John Wiley and Sons, 1978.

79. http://galileo.phys.virginia.edu/classes/311/notes/compflu2/node2.html.

80. Susumu Kuwahara. "Velocity of Sound in Sea-water and Calculation of the Velocity for Use in Sonic Sounding." Hydrographic Review. 16 (November 1939): 123-140.

81. A. Weissler and V. Del Grosso. "The Velocity of Sound in Sea Water." The Journal of the Acoustical Society of America. 23 (2) (March 1951): 219-223.

82. S. Ernst, M. Gepert, and R. Manikowski. "Measurements of the Speed of Sound and Density of Aqueous Solutions of the First-Row Transition Metal Halides. 3. Apparent Molar Compressibilities and Volumes of Aqueous CoI_2 and NiI_2 Within

the Temperature Range 291.15 K to 297.15 K." Journal of Chemical Engineering Data. 45 (6) (November 2000): 1064-1068.

83. N. Rohman, S. Mahiuddin, and N. Dass. "Speed of Sound in Aqueous and Methanolic Lithium Nitrate Solutions." Journal of Chemical and Engineering Data. 44 (3) (1999): 473-479.

84. C.-T. Chen, L.-S. Chen, and F. Millero. "Speed of Sound in NaCl, $MgCl_2$, Na_2SO_4, and $MgSO_4$ Aqueous Solutions as Functions of Concentration, Temperature, and Pressure." Journal of Acoustical Society of America. 63 (6) (June 1978): 1795-1800.

85. Malcolm Crocker, Ed. Handbook of Acoustics. New York: John Wiley and Sons, 1998.

86. Michael Baker. "*In-situ* Monitoring of Reactive Ion Etching." Ph.D. Thesis, Georgia Institute of Technology, November 1996.

87. Dennis Turner. "Role of Sensors in Automatic Electroplating." Plating and Surface Finishing. 73 (6) (June 1986): 30-34.

VITA

Frances Williams was born on December 9, 1972 in Portsmouth, Virginia. She received the B.S. and M.S. degrees in electrical engineering from the North Carolina Agricultural and Technical State University (Greensboro, NC) in 1994 and 1996, respectively. She has worked at Lucent Technologies, Quantira Technologies, the Central Intelligence Agency, NASA, and Fermilab. She began graduate study at the Georgia Institute of Technology in October 1996 and joined the Intelligent Semiconductor Manufacturing research group. Her project in the group was to design, fabricate, and implement a micromachined acoustic sensor to provide *in-situ* monitoring of electroplating, under the supervision of Dr. Gary S. May. At Georgia Tech, Ms. Williams was a National Science Foundation graduate fellow, Office of Naval Research graduate fellow, FACES fellow, GAANN fellow, Sloan Foundation fellow, and a President's scholar. Her research interests include micromachined sensors, integrated circuit (IC) processing, microelectromechanical systems (MEMS) devices and processes, and acoustic devices.